Title
Superconductor/spin-valve proximity effects

Author
Jara Abarzua, Alejandro Andres

Publication Date
2017

Peer reviewed|Thesis/dissertation

UNIVERSITY OF CALIFORNIA,
IRVINE

Superconductor/spin-valve proximity effects

DISSERTATION

submitted in partial satisfaction of the requirements
for the degree of

DOCTOR OF PHILOSOPHY

in Physics

by

Alejandro Andrés Jara Abarzúa

Dissertation Committee:
Professor Ilya Krivorotov, Chair
Professor Zuzanna Siwy
Professor Wilson Ho

2017

DEDICATION

To My Parents:
Myriam and Raúl

TABLE OF CONTENTS

Page

LIST OF FIGURES **v**

ACKNOWLEDGMENTS **xi**

CURRICULUM VITAE **xii**

ABSTRACT OF THE DISSERTATION **xvi**

1 Introduction **1**

2 Background Theory: Magnetism **5**
2.1 Magnetic states 5
2.2 Exchange bias interaction 8
2.3 Magnetoresistance effects 9
2.3.1 Giant Magnetoresistance 10
2.3.2 Tunnel Magnetoresistance 12

3 Background Theory: Superconductivity **14**
3.1 Phenomenological Theory of superconductivity 15
3.1.1 Meissner-Ochsenfeld Effect and London Equation 15
3.1.2 Ginzburg-Landau (GL) theory 16
3.1.3 Type I and II S.C. 17
3.2 Microscopic Theory of Superconductivity 18
3.2.1 BCS and Bogoliubov model Hamiltonians 18
3.2.2 Cooper pair 19
3.3 Superconducting Proximity Effect 21

4 Fabrication **26**
4.1 Introduction 26
4.2 General aspect of fabrication 29
4.2.1 Clean sample 29
4.2.2 Dicing 30
4.2.3 Sputtering deposition 32
4.2.4 Deposition Rate Measurement Using XRR 35
4.2.5 Ion-Mill etching 37

4.2.6 E-Beam Lithography . . . 41
4.3 Nanowires with top contact and square nanopillars . . . 49
4.3.1 Multilayer deposition . . . 49
4.3.2 Definition of wires . . . 50
4.3.3 Dielectric Oxide Growth . . . 56
4.3.4 Open bottom wires . . . 58
4.3.5 Deposition of the top lead wires . . . 60
4.3.6 Definition of pillars . . . 64
4.3.7 Notes Regarding the Fabrication . . . 65
4.4 Testing Results . . . 67

5 Angular dependence of superconductivity in superconductor / spin valve heterostructures 70
5.1 Introduction . . . 70
5.2 Sample Preparation and Characterization . . . 72
5.3 Angular Dependence of T_c . . . 74
5.4 Theoretical Methods . . . 80
5.5 Analysis . . . 83

6 Highly textured $IrMn_3$(111) thin films grown by magnetron sputtering 94
6.1 Introduction . . . 94
6.2 Film Preparation . . . 96
6.3 Film Characterization . . . 96
6.4 Conclusion . . . 104

7 Giant resonant nonlinear damping in nanoscale ferromagnets 109
7.1 Introduction . . . 109
7.2 Results . . . 111
7.2.1 Spin wave spectroscopy . . . 111
7.2.2 Effect of spin torque . . . 113
7.2.3 Theoretical model . . . 115
7.2.4 Effect of the drive amplitude and intrinsic nonlinearitites on the resonance lineshape . . . 119
7.2.5 Effective single-mode nonlinear oscillator approximation . . . 121
7.3 Discussion . . . 123
7.4 Methods . . . 127
7.4.1 Solution of the equations of motion . . . 127
7.4.2 Linewidth evaluation . . . 131
7.4.3 Micromagnetic simulations . . . 131

8 Conclusion 138

LIST OF FIGURES

Page

2.1 **Schematic of magnetic states.** The arrows represent the magnetic moments of the atoms in the crystal. (a) In the paramagnetic state all magnetic moments point in random direction, (b) in the ferromagnetic state all point same direction, and (c) in the antiferromagnetic state neighbor magnetic moment point in opposite direction 6

2.2 **Schematic of a noncollinear antiferromagnet.** Atoms are represented by balls and magnetic moments by arrows. This antiferromagnet has three sublattice represented by green arrows pointing: up-right, up-left, and down. Assuming the magnitude of each magnetic moments is the same, it easy to see that the net magnetization is zero 7

2.3 **Schematic of the exchange bias effect.** The arrows represent the magnetic moments of the atoms in the crystal. The magnetization of the ferromagnet (F) is set by the direction of the adjacent magnetic moment of the antiferromagnet (AF) at the interface. 8

2.4 **First measurement of the exchange bias effect.** The solid lines show the hysteresis loops of Co/CoOx at 77 K when the material is affected by the Exchange bias. In the negative field direction the field has to be higher to saturate the film. Adapted from [5] 9

2.5 **Schematic of the parallel and antiparallel configurations of a SV.** The ferromagnetic layers are represented by the blue layers and the nonmagnetic layer for a orange layer. Red arrows illustrate the magnetization of each ferromagnetic layer. 10

2.6 **First measurement of the GMR effect.** Magnetoresistance from Fe double layers with anti-ferromagnetic coupling. This means that at zero field the system prefers the antiparallel configuration. By increasing the field, one of the magnetic layer reverses the direction of the magnetization and makes the system to get the parallel configuration. Adapted from [1] 11

2.7 **Current in plane and current-perpendicular-to-plane configurations of a GMR SV.** In the left geometry the leads are at the same side of the multilayer making these devices much easier to fabricate than the right geometry which has the leads at opposite side of the multilayer 12

3.1 **Schematic of a metal in the Normal and superconducting states.** This schematic represents a piece of metallic lattice, the atoms are represented by blue circles and conduction electrons by red dots. Left panel represent the normal state and the right panel the superconducting state. 19
3.2 **Suppression of the superconducting transition temperature.** This schematic represents how the penetration of the Cooper pair can change the superconducting transition temperature 21
3.3 **Superconducting proximity effect between a conventional superconductor and a metal:** (a) nonmagnetic metal, (b) ferromagnetic metal with collinear magnetization, and (c) ferromagnetic metal with noncollinear magnetization. 22

4.1 **Etching time measurement.** Left panel shows the sequence of steps if a Filmetrics is used to measure the etching time and the right panel if the XRR is used. 40
4.2 **MAN negative resist pattern.** The value on top of the picture is the size of the pattern. The value in parenthesis is the dose used. The result is the size show with the yellow arrows. All three are nanowires. 42
4.3 **MAN negative resist pattern (cont).** The value on top of the picture is the size of the pattern. The value in parenthesis is the dose used. The result is the size show with the yellow arrows. All three are nanowires. 43
4.4 **MAN negative resist pattern (cont).** The value on top of the picture is the size of the pattern. The value in parenthesis is the dose used. The result is the size show with the yellow arrows. (a) is a wire, (b) a nanodot, and (c) a nano ellipse 44
4.5 **Current misalignment correction procedure.** Images of the monitor of the EBL computer in each step: (a) shows the alignment pattern centered to the reference particle at the smallest current (e.g. 13 pA), (b) shows the same thing at the next current (e.g. 800 pA or 6400 pA) to know the misalignment with respect to the smallest current, (c) shows after centering the alignment pattern to the reference particle, and (d) shows where the offset values are shown in the monitor 48
4.6 **Definition of bottom wires.** Left panel shows the multilayer structure with the e-beam MAN resist pattern on top of the multilayer. The MAN resist is used as hard mask for the etching process. Right panel shows the sample after etching, the nanowires are already defined 50
4.7 **Global map of patterns.** The red square with a X in the center are the big alignment marks. The black cross are the devices (bottom leads, top leads and local alignment marks). There are two horizontal lines of big alignment marks, this is to have the option to divide the sample in two pieces (top and bottom) and continue the fabrication for each piece independently. Two big alignment marks are necessary for piece, however, if you want to subdivide the piece in columns, it good to have an alignment mark for each of those column. That is why in this example each column has their own big alignment marks. Local alignment marks are not shown in this schematic. 52

4.8 **Big alignment mark.** This pattern is completely symmetric. Some dimensions are shown and the rest are evidently known by symmetry. 53
4.9 **Pattern for e-beam lithography of the bottom lead.** This consists in three parts: blue is the big part of the lead, green is the medium leads with the medium local alignment marks (L-shape), and yellow is the nanowire with the small local alignment marks (squares). In general, the smallest alignment marks have to be written along with the most important part (e.g. nanowire) 55
4.10 **Dielectric Oxide Growth.** The schematic shows how the wire is cover completely by the SiO_2 film creating a bump on top of the wire. The thickness of SiO_2 on top of the wire is the same as the thickness on the rest of the substrate. This is represented in the right panel 57
4.11 **Demonstration of the presence of SiO2 at the side of the wire.** SEM image of a sample destroyed by electric discharge, the two horizontal white line at the center is possible to see the remaining dielectric oxide growth at the side-walls of the wire 58
4.12 **SEM images** of the same wire after etching SiO_2. (a) after etching 10 min, (b) after etching extra 30 sec, total etch time = 10.5 min, (c) after etching a second extra 30 sec, total etch time = 11 min, and (d) after O_2 plasma etching for 3 min. 59
4.13 **Open bottom wires.** After an anisotropic etching process SiO_2 is removed from everywhere except the side of the wire (left). Right panel represent the sample after remove the MAN resist with O_2 plasma. 60
4.14 **Comparison between sputter and evaporated top lead.** Left panel shows the sputter top vertical lead, this lead is not very-well define. There is a huge side-wall and the center of the top lead looks thinner than the evaporated. This may be due to a shadow effect during deposition. The e-beam resist probably block the access to the material inside of the cavity. Instead, the right panel has an e-beam evaporated well-defined top wire which looks much thicker than the sputtered one. That is why the evaporated top lead is desirable as hard mask for the last step (definition of pillars). 61
4.15 **Deposition of the top wire.** The top lead in the illustration is represented by blue color because this can be either normal lead or superconducting material lead. 62
4.16 **Pattern for e-beam lithography of the top lead.** Two images of the dgs file program to make the top lead (vertical structure). The dimensions are the same as for the bottom lead layer. The only different is the top lead wire is wider in some part to reduce the resistance and the distance between the medium leads are longer than fro the bottom leads. However, the dimensions will depend on the application. 63
4.17 **SEM image of the structure after depositing the top lead** Vertical wire is the top lead wire and the horizontal wire is the bottom lead wire. The top lead of this sample was sputtered, that is why there is some strutures at the edges of the wire. 64
4.18 **Definition of the pillars.** The schematic shows how the nanopillar would look after the last etching process. 64

4.19 **Dirty surface using MAN resist.** In this SEM images is shown the MAN resist in not remove in the same way every time 66
4.20 **Current perpendicular-to-plane measurement.** Resistance versus field along the bottom wire direction. Top plot shows the data when the system is at normal state and the bottom plot when is at superconducting state 68

5.1 **Schematic and resistance versus magnetic field.** (a) Schematic of the CoO(2 nm)/ Co(d_p)/ Cu(d_n)/ Co(d_f)/ Nb(17 nm) multilayer, where α is the in-plane angle between the magnetic moments of the Co layers. (b) Resistance versus the in-plane magnetic field applied parallel to the pinned layer magnetization at $T = 4.2$ K (above the superconducting transition temperature). . 73
5.2 **Resistance versus temperature** for parallel (P, $\alpha = 0$), antiparallel (AP, $\alpha = \pi$), and perpendicular (90°, $\alpha = \frac{\pi}{2}$) orientations of magnetic moments of the Co layers for multilayer samples with (a) $d_f = 0.5$ nm and (b) $d_f = 1.0$ nm. The resistance is divided by its normal state value measured at $T = 4.2$ K. 75
5.3 **Resistance versus angle.** Resistance of a CoO(2 nm)/ Co(2.5 nm)/ Cu(6 nm)/ Co(0.6 nm)/ Nb(17 nm) structure versus magnetic field angle, α , measured at $T = 2.92$ K in the middle of the superconducting transition, at a field of 800 Oe. 76
5.4 T_c **versus angle.** $T_c(\alpha)$ for a CoO(2 nm)/ Co(1.5 nm)/ Cu(6 nm)/ Co(0.6 nm)/ Nb(17 nm) multilayer calculated from the $R(\alpha)$ data by different methods described in the text. 77
5.5 T_c **versus angle and thicknesses.** $T_c(\alpha)$ for representative samples from the three series of samples studied in this paper. (a) From the d_f series, (b) from the d_n series, (c) from the d_p series. 78
5.6 ΔT_c **versus thicknesses.** Dependence of $T_c(\pi) - T_c(0)$ (red circles) and $T_c(\frac{\pi}{2}) - T_c(0)$ (green squares) on the free Co layer thickness d_f (a), nonmagnetic spacer thickness d_n (b), and pinned layer thickness d_p (c). 78
5.7 **Experimental data and theoretical fitting** of T_c in the P state as a function of (a) the Co free layer thickness d_f (with $d_n = 6$ nm and $d_p = 2.5$ nm), (b) the Cu normal metal layer thickness d_n (with $d_p = 2.5$ nm and $d_f = 0.6$ nm), and (c) the Co pinned layer thickness d_p (with $d_n = 6$ nm and $d_f = 0.6$ nm). 82
5.8 **Experiment and theory comparisons** of ΔT_c [defined as $\Delta T_c(\alpha) \equiv T_c(\alpha) - T_c(0)$] as a function of relative magnetization angle are shown for the three batches of samples. Top row: Three different free layer thicknesses, $d_f =$ 0.6 nm, 0.8 nm, 0.9 nm, and with $d_p = 2.5$ nm, $d_n = 6$ nm. Middle row: Three different nonmagnetic layer thicknesses: $d_n = 4$ nm, 5 nm, 6.8 nm, and with $d_f = 0.6$ nm, $d_p = 2.5$ nm. Bottom row: Three different pinned layer thicknesses: $d_p = 1.5$ nm, 3.5 nm, 5.5 nm, and with $d_f = 0.6$ nm, $d_n = 6$ nm. 85

5.9 **Average triplet amplitudes in the pinned ferromagnet layer as a function of relative magnetization angle**. The quantity plotted is the average of $F_t(y,t)$ [Eq. (5.8)] in this region, at $\omega_D t = 4$. The quantity ΔT_c is also shown (right scale). Red squares are the theoretical triplet amplitudes (left scale) and the blue circles are the experimental ΔT_c (right inverted scale) as a function of angle. The ΔT_c data correspond to one set chosen from each batch of samples in Fig. 5.8. (a) From the d_f series, (b) from the d_n series, (c) from the d_p series. 87

6.1 **Crystallographic structure of $IrMn_3$.** (a) Unit cell of $IrMn_3$ in the $L1_2$ phase. Green arrows indicate the magnetic moments of Mn. (b) A (111) plane of $IrMn_3$ in the $L1_2$ phase. 98
6.2 **Grazing incident XRD profiles.** The vertical axis is linear. The inset shows the schematic of the experiment. 98
6.3 **XRD $\theta/2\theta$ scans.** The vertical axis is logarithmic. The inset shows the schematic of the experiment. 99
6.4 **XRD analysis of a peak.** XRD analysis of the out-of-plane (111) $IrMn_3$ reflection of the textured sample 4: (a) $\theta/2\theta$ and (b) Rocking curve. 100
6.5 **XRD pole figures.** XRD pole figures of the (100) reflections ($2\theta = 23.53°$) of the untextured sample 3 (a) and textured sample 4 (c); the (111) reflections ($2\theta = 41.36°$) of untextured sample 3 (b) and textured sample 4 (d). The sets of peaks A and B have a polar angle of 54.7° which is the same as for the $\langle 100 \rangle$ directions of $IrMn_3$. C and D peaks have a polar angle of 70.5°, corresponding to $\langle 111 \rangle$ peaks of $IrMn_3$. A and C are sets of peaks of the weak phase, B and D represent the strong phase. E marks the [111] peak of $IrMn_3$ which is shared by both phases. Enclosed in a white circles are the residual signal from the tail of the MgO (200) reflection peaks. 101
6.6 **XRD 2θ scan along [100] direction.** XRD 2θ scan along [100] direction of the strong phase for the textured sample 4. The vertical axis is logarithmic intensity. The feature marked K_β at 42.85° is an artifact due to residual K_β(Cu) radiation. F and S indicate the fundamental and the superlattice peaks. 104

7.1 **Spin wave spectra in a nanoscale MTJ. a** Normalized ST-FMR spectra $\langle \tilde{V}_{\mathrm{mix}}(f) \rangle$ of spin wave eigenmodes in a perpendicular MTJ device (Sample 1) measured as a function of out-of-plane magnetic field. Resonance peaks arising from three low frequency modes of the MTJ free layer $|0\rangle$, $|1\rangle$, and $|2\rangle$ are observed. **b** Spectral linewidth of the quasi-uniform $|0\rangle$ spin wave mode as a function of out-of-plane magnetic field. Strong linewidth enhancement is observed in the resonant three-magnon regime at H_1 and H_2. 111

7.2 **Effect of spin torque on spin wave resonance lineshape. a, b** Spin wave resonance lineshapes in the nonresonant regime at $H > H_1$ for different values of direct bias current $I_{\rm dc}$. **c, d** Spin wave resonance lineshapes in the resonant three-magnon regime at $H = H_1$. **a, c** Measured ST-FMR spectra (Sample 2). **b, d** Solutions of Eqs. (3) and (4). Identical bias current values $I_{\rm dc}$ (displayed in **a**) are used in **a-d**. 113

7.3 **Effect of spin torque on linewidth.** Linewidth of the quasi-uniform spin wave mode as a function of the applied direct bias current (Sample 3): blue symbols – in the nonresonant regime $H \neq H_1$ and red symbols – in the resonant three-magnon regime $H = H_1$. Lines are numerical fits using Eqs. (3) and (4). 117

7.4 **Effect of intrinsic nonlinearities on the quasi-uniform spin wave resonance lineshape.** Spectral lineshape of the quasi-uniform spin wave mode resonance $|\bar{a}|^2(\omega)$ at the three-magnon resonance condition $2\omega_0 = \omega_n$ calculated by numerically solving Eq. (7.30). The red curve is a reference lineshape calculated with all intrinsic nonlinearity parameters $(\eta_0, \eta_n, \Psi_0, \Psi_n)$ set to zero. The blue lineshape in each panel is calculated with one of the intrinsic nonlinearity parameters set to a non-zero value: **a** $\eta_0 = 1.325 \cdot 10^{-24}\,\mathrm{J}$, **b** $\eta_n = 3.313 \cdot 10^{-24}\,\mathrm{J}$, **c** $\Psi_0 = 1.325 \cdot 10^{-24}\,\mathrm{J}$, **d** $\Psi_n = 1.325 \cdot 10^{-23}\,\mathrm{J}$. Other parameters employed in the calculation are: $\omega_0 = 2\pi \cdot 2.63\,\mathrm{GHz}$, $\omega_n = 2\pi \cdot 5.26\,\mathrm{GHz}$; $\alpha_0 = 0.02662$, $\alpha_n = 0.03042$ at $I_{\rm dc} = 0$; $\psi_n \cdot \zeta = h^2 \cdot 0.006\,\mathrm{GHz}^2$, where h is the Planck constant. 120

7.5 **Effect of the drive amplitude on linewidth in the resonant three-magnon regime.** Calculated linewidth of the quasi-uniform spin wave mode as a function of the drive amplitude ζ for different values of the mode coupling parameter ψ_n. (i) Green: $\psi_n = 0$, (ii) red: variable ψ_n with a constraint $\psi_n \cdot \zeta = h^2 \cdot 0.006\,\mathrm{GHz}^2$, and (iii) blue: $\psi_n = h \cdot 0.1\,\mathrm{GHz}$. All intrinsic nonlinearity parameters: Ψ_0, Ψ_n, η_0 and η_n are set to zero. h is the Planck constant. Other parameters employed in the calculation are: $\omega_0 = 2\pi \cdot 2.63\,\mathrm{GHz}$, $\omega_n = 2\pi \cdot 5.26\,\mathrm{GHz}$; $\alpha_0 = 0.02662$ and $\alpha_n = 0.03042$ at $I_{\rm dc} = 0$. 121

7.6 **Spatial profiles of spin wave eigenmodes.** Normalized amplitude and phase of the three lowest frequency spin wave eigenmodes of the MTJ free layer, given by micromagnetic simulations. 132

ACKNOWLEDGMENTS

I would like first to express my gratitude to my research advisor, Professor Ilya Krivorotov. His support and guidance have been crucial to my research. His leadership has allowed to create a unique team of people where each member contributes to keep growing the group and to pass on knowledge to the following generations. I would also like to thank the members of my doctoral committee, Dr. Zuzanna Siwy and Dr. Wilson Ho, for taking time out of their busy schedules to help me accomplish this important task.

I would like to thank everyone who has contributed directly or indirectly to my research. Dr. Brian Youngblood and Dr. Yu-Jin Chen, who were the first people to teach me how to do experiments in the lab. Jian Zhu and Graham Rowlands, who helped me by answering all my questions by e-mail. My coworker Chris Safranski, with whom I published my first paper with professor Ilya Krivorotov's group. Dr. Zheng Duan and Dr. Liu Yang, who guided me through my first steps in the fabrication process. Dr. Andrew Smith and Jen-Ru Chen, for being awesome partners in the fabrication tasks. Dr. Han Kyu Lee and Dr. Eric Montoya, for allowing me to learn from their big research experience. Harmeet Gill and Amanatullah Khan, for giving me the opportunity to teach them and give my first steps as a mentor. Dr. Jieyi Zhang, Chengcen Sha, Josh Dill, Alexandre Goncalves, and Tobias Schneider, although I haven't collaborated with them directly, they have been great labmates. I would also like to give special thanks to Dr. Igor Barsukov for guiding me in different projects and for teaching me concepts of condensed matter. I wanted to thank Dr. Qiyin Lin for teaching me how to do XRD characterization. I would also like to thank my collaborators including professor Oriol Valls, Chien-Te Wu, Abdul N. Malmi-Kakkada, and Klaus Halterman for their great theoretical work in superconducting proximity effect. Patrick Braganca, John Read, and Hua Chen for the design and fabrication of the $IrMn_3$ films. Alexandre Gonçalves, J. A. Katine, Rodrigo Arias, and Boris Ivanov for the collaboration in the work of "Giant resonant nonlinear damping in nanoscale ferromagnets".

Finally, I would like to thank my friends and family. I am deeply indebted to my parents Myriam and Raúl and to my siblings Bárbara and Raúl Jr. for being the pillars of my life. Also, I am wholeheartedly grateful to my partner in all this process, my wife Tracy Dunstan, for her love and emotional support, and to my daughter Emilia Jara who is my source of energy.

I would like to acknowledge Physical Review B. for allowing the use of "Angular dependence of superconductivity in superconductor/spin-valve heterostructures" in chapter 5 of this dissertation. I would like to acknowledge IEEE Magnetics Letters for allowing the use of "Highly textured IrMn3(111) thin films grown by magnetron sputtering" in chapter 6 of this dissertation.

Funding support from the prestigious Fulbright-CONICYT Scholarship during the first four years of my graduate program is acknowledged.

CURRICULUM VITAE

Alejandro Andrés Jara Abarzúa

EDUCATION

Ph.D. in Physics	Physics and Astronomy Department, University of California, Irvine, 2017
M.S. in Chemical and Material Physics	Physics and Astronomy Department, University of California, Irvine, 2017
M.S. in Physics	Facultad de Ciencias Fisicas y Matematicas, Universidad de chile, 2010
B.S in Physics	Facultad de Ciencias Fisicas y Matematicas, Universidad de chile, 2007

RESEARCH EXPERIENCE

2012-2017	Superconducting/ferromagnetic Proximity effects & Nanofabrication and characterization Graduate Research Assistant, Physics and Astronomy Department, University of California, Irvine.
2008-2010	Normal modes in ferromagnetic and dielectric nanowires Graduate Research Assistant, Facultad de Ciencias Fisicas y Matematicas, Universidad de Chile.
July 2007-December 2007	Measuring dislocation density in aluminum with ultrasound spectroscopy Undergraduate Research Assistant, Facultad de Ciencias Fisicas y Matematicas, Universidad de Chile.
January 2007-March 2007	The breakup of a water drop and a glycerin drop Undergraduate Research Assistant, James Franck Institute, University of Chicago.

TEACHING EXPERIENCE

2015 Teaching Assistance
Physics and Astronomy Department,
University of California, Irvine.

2005-2009 Teaching Assistance
Facultad de Ciencias Fisicas y Matematicas,
Universidad de Chile.

RECOGNITION & AWARDS

PhD's degree Scholarship Miguel Velez Scholarship
University of California , 2016

PhD's degree Scholarship US-Chile Equal Opportunities Scholarship
Fulbright-CONICYT , 2011-2015

Master's degree Scholarship Departamento de Fisica Scholarship
universidad de chile, 2008-2009

Bachelor's degree Scholarship Juan Gomez Millas Scholarship
Chilean Ministry of Education, 2003-2007

Academic Excellence Recognition The Highest Score in Mathematics in National University Admission Process, 2002
H. Consejo de Rectores Universidades Chilenas

RESEARCH INTERESTS

- *Experimental Physics, Condensed Matter Physics, Nanomagnetism, Spintronics, Nanofabrication and Characterization, Proximity effects in ferromagnetic/superconducting nanostructures*

PUBLICATION

- *Giant resonant nonlinear damping in nanoscale ferromagnets*
  I. Barsukov, H. K. Lee, A.A. Jara, Y.-J. Chen, A. M. Gonçalves, C. Sha, J. A. Katine, R. E. Arias, B. A. Ivanov, and I. N. Krivorotov, (manuscript in preparation).

- *Spin caloritronic nano-oscillator*
  C. Safranski, I. Barsukov, H.K. Lee, T. Schneider, A.A. Jara, A. Smith, H. Chang, K. Lenz, J. Lindner, Y. Tserkovnyak, M. Wu, I.N. Krivorotov, Nature Communications **8**, 117 (July 2017).

- *Highly textured IrMn3(111) thin films grown by magnetron sputtering*
  A.A. Jara, I. Barsukov, B. Youngblood, Y.-J. Chen, J. Read, Hua Chen, P. Braganca, I.N. Krivorotov, IEEE Magn. Lett. **7**, 3104805 (July 2016).

- *Angular dependence of superconductivity in superconductor/spin-valve heterostructures*
  Alejandro A. Jara, Christopher Safranski, Ilya N. Krivorotov, Chien-Te Wu, Abdul N. Malmi-Kakkada, Oriol T. Valls, and Klaus Halterman, PHYSICAL REVIEW B **89** 184502 (May 2014).

- *Plasmons and the electromagnetic response of nanowires*
  A.A. Jara, R.E. Arias and D.L. Mills, PHYSICAL REVIEW B **81** 08542 (FEB 2010).

- *Measuring Dislocation Density in Aluminum with Resonant Ultrasound Spectroscopy*
  Felipe Barra, Andres Caru, Maria Teresa Cerda, Rodrigo Espinoza, Alejandro A. Jara, Fernando Lund, and Nicolas Mujica, INTERNATIONAL JOURNAL OF BIFURCATION AND CHAOS **19** No. 10 (JAN 2009).

CONTRIBUTED TALKS & POSTERS

- A.A. Jara and I. Krivorotov, "Bias Current Dependence of Angular Magneto-Resistance in Superconductor/Spin-Valve Nanowires," *62th Conference on Magnetism and Magnetic Materials 2017, Pittsburgh, Pennsylvania.*

- D. Ellsworth, H. Chang, D. Qu, A.A. Jara, R. Wu, I. Krivorotov, C. Chien and M. Wu, "Wavelength Characteristics of the Photo-Spin-Voltaic Effect," *61th Conference on Magnetism and Magnetic Materials 2016, New Orleans, Louisiana.*

- M. Wu, D. Ellsworth, L. Lu, J. Lan, H. Chang, P. Li, Z. Wang, D. Qu, A.A. Jara, J. Hu, B. Johnson, Y. Bian, J. Xiao, I. Krivorotov, C.L. Chien and R. Wu, "Photo-Spin-Voltaic Effect," *61th Conference on Magnetism and Magnetic Materials 2016, New Orleans, Louisiana.*

- A.A. Jara, I. Barsukov, B. Youngblood, Y. Chen, J.C. Read, P.M. Braganca and I. Krivorotov, "Epitaxial growth of IrMn3 thin films by sputter deposition," *MMM — INTERMAG, 2016 Joint Conference, San Diego, California.*

- C.J. Safranski, I. Barsukov, H. Lee, T. Schneider, A.A. Jara, A. Smith, H. Chang, M. Wu and I. Krivorotov, "Spin Current Control of Damping in YIG/Pt Nanowires," *MMM — INTERMAG, 2016 Joint Conference, San Diego, California.*

- H. Lee, I. Barsukov, C.J. Safranski, A.A. Jara, L. Yang, A. Swartz, B. Kim, H. Hwang and I. Krivorotov, "Magnetization dynamics in LSMO/Pt nanowires in the presence of spin Hall torques," *MMM — INTERMAG, 2016 Joint Conference, San Diego, California.*

- A.A. Jara, Igor Barsukov, Yu-Jin Chen, Brian Youngblood, John Read, Patrick Braganca, Ilya Krivorotov, "Epitaxial IrMn3 on MgO(111) by sputter deposition," *American Physical Society March Meeting 2015, San Antonio, Texas.*

- A.A. Jara, Christopher Safranski, Ilya N. Krivorotov, Chien-Te Wu, Oriol T. Valls, "Angular dependence of superconductivity in spin valve / superconductor heterostructures," *American Physical Society March Meeting 2014, Denver, Colorado.*

- A.A. Jara, Christopher Safranski, Ilya N. Krivorotov, Chien-Te Wu, Oriol T. Valls, "Angular dependence of superconductivity in spin valve / superconductor heterostructures," *58th Conference on Magnetism and Magnetic Materials 2013, Denver, Colorado.*

- A.A. Jara, R.E. Arias, and D.L. Mills, "Magnetostatic modes in ferromagnetic nanowires," *Escola Brasil-Chile de Nanomagnetismo 2010, Porto Alegre, R.S. - Brasil.*

- A.A. Jara, R.E. Arias, and D.L. Mills, "Magnetostatic modes in ferromagnetic nanowires," *II Escuela de Magnetismo 2010, Santiago, Chile.*

- R.E. Arias, A.A. Jara, and D.L. Mills, "Plasmons and The Electromagnetic Response of Nanowires," *American Physical Society March Meeting 2010, Portland, Oregon.*

- A.A. Jara, R.E. Arias, and D.L. Mills, "Plasmons and the electromagnetic response of dielectric nanowires," *VI Taller de Jovenes Cientificos iniciativa Cientifica Milenio 2009, Santiago, Chile.*

- A.A. Jara, R.E. Arias, and D.L. Mills, "Plasmons and the electromagnetic response of dielectric nanowires," *Workshop in Magnetism 2009, Rancagua, Chile.*

PROFESSIONAL MEMBERSHIPS

- *American Physical Society (APS).*

ABSTRACT OF THE DISSERTATION

Superconductor/spin-valve proximity effects

By

Alejandro Andrés Jara Abarzúa

DOCTOR OF PHILOSOPHY in Physics

University of California, Irvine, 2017

Professor Ilya Krivorotov, Chair

This thesis describes three experiments in the topics of magnetism and superconductivity. The first experiment demonstrates the ability to have magnetic control of the triplet component amplitude in a Nb/Co/Cu/Co/CoO superconducting spin valve. The experiment is done by measuring the superconducting transition temperature, T_c, in the multilayers as a function of the angle α between the magnetic moments of the Co layers. The measurements reveal that $T_c(\alpha)$ is a nonmonotonic function, with a minimum near $\alpha = \pi/2$. The experimental data were compared with numerical self-consistent solutions of the Bogoliubov–de Gennes equations calculated by our collaborators. This thesis shows that experimental data and theoretical evidence agree in relating $T_c(\alpha)$ to enhanced penetration of the triplet component of the condensate into the Co/Cu/Co spin valve in the maximally noncollinear magnetic configuration. The second experiment is a crystallographic characterization of a magnetron sputtered $IrMn_3$ thin film which is a metallic non-collinear antiferromagnet. It has been predicted to have a large anomalous Hall effect, which enables magnetic state readout in antiferromagnetic spintronic devices. The third experiment is a demonstration of unusual magneto-dynamic phenomena in nanoscale ferromagnets due to resonant three-magnon scattering. In this work, some numerical calculations are presented of a theory made by a collaborator.

Chapter 1

Introduction

Spintronics is an intensive area of research in condensed matter physics. Since the discovery of giant magnetoresistance, three decades ago, by Albert Fert and Peter Grunberg [1, 2], there have been a lot of new important discoveries including tunneling magnetoresistance and the spin transfer torque effect. Smaller, faster, and more energy-efficient technologies have been invented as a result of this vibrant and intellectually rich field of research. The inclusion of superconducting materials in spintronics can boost the possibilities of finding new and exciting phenomena. For this reason, superconductor/ferromagnetic (S/F) heterostructures have been a focus of intensive research over the past decade. Apart from their importance for understanding the fundamental physics of the superconducting proximity effect, S/F nanostructures may find applications in low-power cryogenic computing [3]. Competition between superconducting and ferromagnetic ordering in S/F heterostructures can lead to unusual types of magneto-transport effects emerging from the proximity effect at the S/F interfaces. An example of such an effect is non-monotonic angular dependence of magnetoresistance (MR) observed in S/F/F spin valves near the superconducting transition temperature T_c. The origin of this non-monotonic MR is the long-range odd triplet compo-

nent of the condensate, whose amplitude is controlled by the magnetic configuration of the F layers of the spin valve [4].

Chapter 2 and 3 give background theory that is necessary for understanding the physics in the experimental results. Chapter 2 explains the magnetic concepts and the main effects relevant for this dissertation such as giant magnetoresistance, exchange bias, noncollinear antiferromagnets and magnetic tunnel junctions. Chapter 3 shows a description of the two theoretical approaches to superconductivity: phenomenological and microscopic. Then, it explains the superconducting proximity effect in the three possible scenarios where a superconductor is in proximity with: a nonmagnetic metal, a ferromagnet with collinear magnetization, and a ferromagnet with non-collinear magnetization.

Chapter 4 provides recipes and instructions for each task utilized in this dissertation. My idea is not just to restate instructions already presented by previous members of the group, instead I would like to share my experience in the fabrication of nanodevices. I start describing some general aspects of fabrication by explaining some basic procedures such as deposition, etching, lithography, and characterization. Lastly, I describe the design and the fabrication method of this new non-standard type of nanopillar with which I have been working.

Chapter 5 describes the experiment which demonstrates the angular dependence of T_c. It describes the sample fabrication, the characterization at normal states, and then the methods to measure the angular dependence of T_c. Next it gives a summary of the theoretical description and the comparison with the experimental data. The end of the chapter provides some discussion of the work.

Although, the main work of this dissertation is the study of the interplay between magnetism and superconductivity, it also contains two works in other areas of magnetism.

Chapter 6 reports growth of highly textured films of a non-collinear antiferromagnet $IrMn_3$ on MgO(111) substrates by magnetron sputtering. The films consist of epitaxial (111) twin

domains rotated by 60 degrees within the film plane. The films exhibit partial $L1_2$ ordering that supports the non-collinear T1 spin ground states structure predicted to give rise to anomalous Hall effect, which enables magnetic state readout in antiferromagnetic spintronic devices. An MgO buffer layer evaporated onto the substrate increases the $L1_2$ order parameter from 0.4 to 0.75 but destroys the (111) crystallographic texture.

Chapter 7 experimentally demonstrates that nonlinear damping due to resonant three-magnon scattering gives rise to two unusual magneto-dynamic phenomena in nanoscale ferromagnets. First, a spin wave mode amplitude can exhibit a minimum at the resonance frequency instead of the usual maximum observed in the linear regime. Second, spin torque normally acting as antidamping can strongly enhance the damping of a spin wave undergoing three-magnon scattering. It presents a theory and numerical calculation that explains these counterintuitive phenomena. This work advances understanding of magnetic dynamics in nanoscale ferromagnets and spin torque devices.

Finally, Chapter 8 concludes the thoughts of this thesis.

Bibliography

[1] G. Binasch et al. "Enhanced magnetoresistance in layered magnetic structures with antiferromagnetic interlayer exchange". In: *Phys. Rev. B* 39.7 (1989), pp. 4828–4830. ISSN: 01631829.

[2] M. N. Baibich et al. "Giant Magnetoresistance of (001)Fe/(001)Cr Magnetic Superlattices". In: *Phys. Rev. Lett.* 61 (21 1988), pp. 2472–2475. URL: https://link.aps.org/doi/10.1103/PhysRevLett.61.2472.

[3] D. S. Holmes, A. L. Ripple, and M. A. Manheimer. "Energy-Efficient Superconducting Computing – Power Budgets and Requirements". In: *IEEE Transactions on Applied Superconductivity* 23.3 (2013), pp. 1701610–1701610. ISSN: 1051-8223.

[4] Alejandro A. Jara et al. "Angular dependence of superconductivity in superconductor/spin-valve heterostructures". In: *Phys. Rev. B* 89 (18 2014), p. 184502. URL: https://link.aps.org/doi/10.1103/PhysRevB.89.184502.

Chapter 2

Background Theory: Magnetism

This chapter cover some concepts of magnetism which are essential for understanding the work shown in this thesis.

2.1 Magnetic states

Magnetic states have a microscopic origin in the interaction between the magnetic moments. A simple model to understand this is to think a material as a collection of independent microscopic pieces of magnet where each of them has their own direction of the north and south pole. Those magnets are the magnetic moments. The arrangement, direction and magnitude of the magnetic moments and the interaction between each other produce different magnetic state. For example, paramagnetic state in which the direction of all magnetic moments are randomly distributed (Fig.2.1(a)), ferromagnetic state in which all magnetic moments are in parallel alignment (Fig.2.1(b)), and antiferromagnetic state in which adjacent magnetic moments are in antiparallel alignment (Fig.2.1(c)).

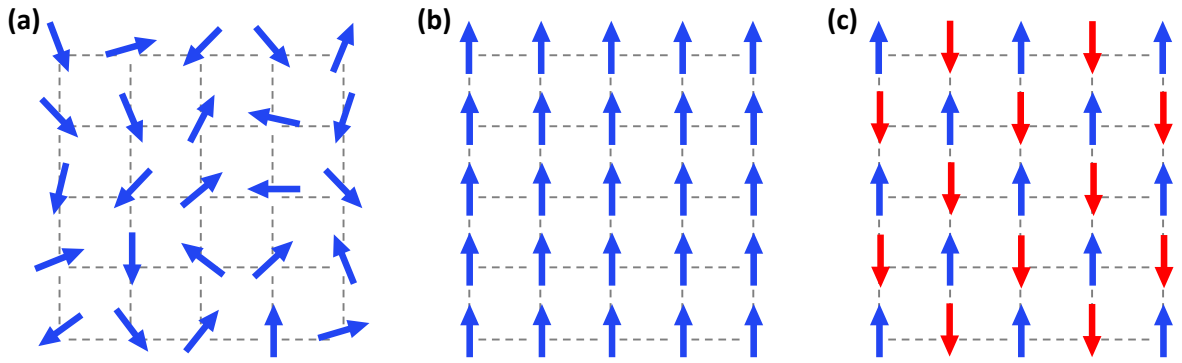

Figure 2.1: **Schematic of magnetic states.** The arrows represent the magnetic moments of the atoms in the crystal. (a) In the paramagnetic state all magnetic moments point in random direction, (b) in the ferromagnetic state all point same direction, and (c) in the antiferromagnetic state neighbor magnetic moment point in opposite direction

The two main interactions between magnetic moments are: magnetic dipolar and the exchange. The order of magnitude of the ***magnetic dipolar effect*** between magnetic moments is very low to explain the long range magnetic order of most of the material (it can be important at milliKelvin temperatures). This means the ***exchange interaction*** is the most important effect to account for the magnetic ordering. The term in the Hamiltonian for this effect is

$$H = -\frac{1}{2}\sum_{ij} J_{ij}\vec{S}_i \cdot \vec{S}_j \tag{2.1}$$

where J_{ij} is the exchange constant between the i^{th} and j^{th} magnetic moments (or spins). Ferromagnetic materials has positive exchange constant ($J > 0$) for nearest neighbors. On the other hand, antiferromagnetic materials has negative ($J < 0$) exchange constant.

Ferromagnets and antiferromagnets can be also differentiated by their ***magnetization*** ($\vec{M}$) which is defined as the magnetic moment per unit volume. This is usually considered a macroscopic quantity, then it is smooth and continues except at the edges of the material. Ferromagnets has spontaneous magnetization even in the absence of external magnetic field.

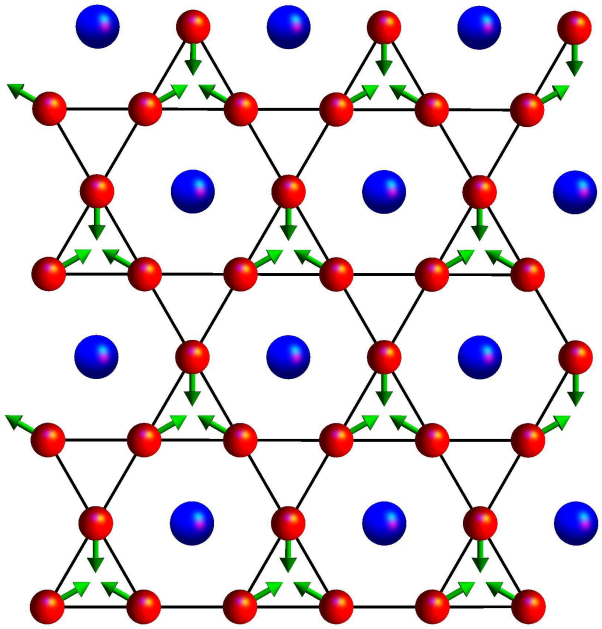

Figure 2.2: **Schematic of a noncollinear antiferromagnet.** Atoms are represented by balls and magnetic moments by arrows. This antiferromagnet has three sublattice represented by green arrows pointing: up-right, up-left, and down. Assuming the magnitude of each magnetic moments is the same, it easy to see that the net magnetization is zero

Antiferromagnets, on the other hand, has zero total magnetization. However, antiferromagnets can be thought as two interpenetrating sublattices, blue and red in Fig.2.1(c) where the magnitude of magnetization of each sublattice are the same, $|M_{up}| = |M_{down}|$.

These two magnetic states have a transition temperature above which is the paramagnetic state. The order parameter of ferromagnets is the magnetization and its transition temperature is known as the *Curie temperature*. For metals like Co, Fe and Ni, the Curie temperature are above room temperature 1388, 1043 and 627 K respectively. Spontaneous magnetization and high transition temperature are two of the reasons why magnetism was first discovered in the ancient world. The order parameter of antiferromagnets is the sum of the magnetization magnitude of the sublattices, $|M_{up}| + |M_{down}|$, and its transition temperature is known as the *Néel temperature*. There are antiferromagnets at room temperature, but its zero net magnetization made impossible to discover until the modern times.

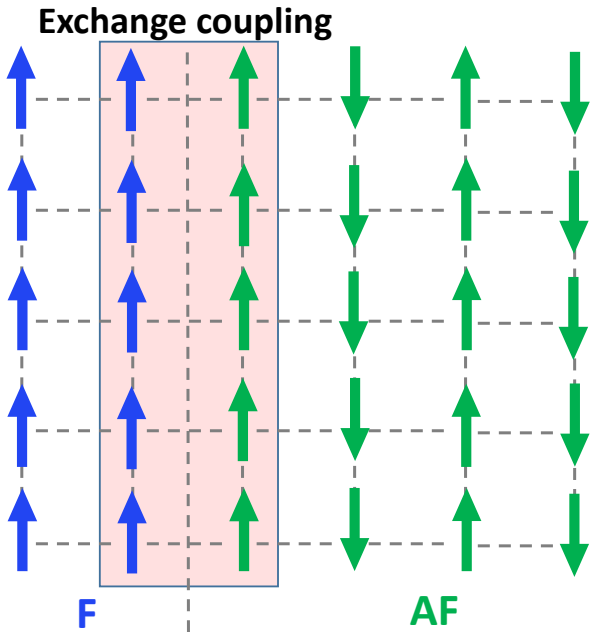

Figure 2.3: **Schematic of the exchange bias effect.** The arrows represent the magnetic moments of the atoms in the crystal. The magnetization of the ferromagnet (F) is set by the direction of the adjacent magnetic moment of the antiferromagnet (AF) at the interface.

The large number of ways of arranging the two sublattices in a crystal make antiferromagnetic materials a potential source of new physical phenomena. Even more if one considers the antiferromagnets with more than two sublattice. For example, $IrMn_3$ which is a ***noncollinear antiferromagnet*** with three sublattices as shown in Fig.2.2. Noncollinear antiferromagnetism is a subject of ongoing research.

It is important to note that the magnetic states presented here were assuming perfect material where there is a complete correlation between all part of the the crystal. The real sample, however, has some magnetic domains where each of them behaves as a perfect material.

2.2 Exchange bias interaction

Exchange anisotropy was discovered by Meiklejohn and Bean in 1956 [5], they found a shift in the magnetization curve in a Co/CoOx bilayer. The shift is due to the extra magnetic field

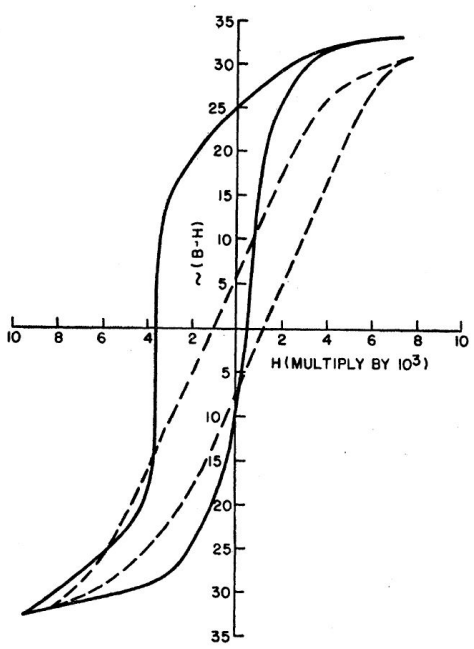

Figure 2.4: **First measurement of the exchange bias effect.** The solid lines show the hysteresis loops of Co/CoOx at 77 K when the material is affected by the Exchange bias. In the negative field direction the field has to be higher to saturate the film. Adapted from [5]

necessary to reverse the direction of the magnetization of the ferromagnetic material, Fig.2.4. In other words, the magnetization of the ferromagnets is pinned by exchange interaction with the magnetic moment of the antiferromagnetic at the interface. Figure 2.3 shows the relation of the magnetic moments of both materials at the interface. The exchange bias effect has had an technological impact in magnetic memory. It has been used to pin the magnetization of soft ferromagnetic layers.

2.3 Magnetoresistance effects

The magnetoresistance (MR) is the modification of the resistance due to magnetic state of the sample and the external magnetic field. For example, the resistance of a ferromagnetic film is different if an external magnetic field is applied perpendicular or parallel to the current.

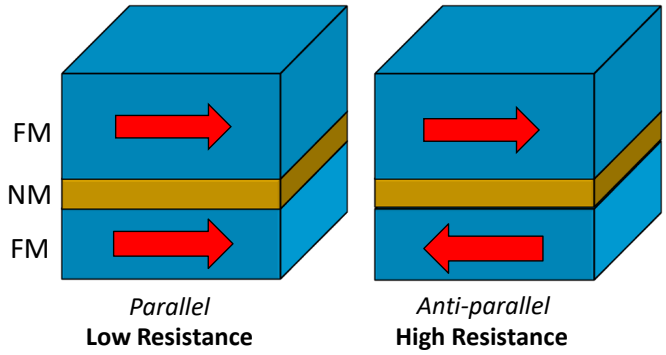

Figure 2.5: **Schematic of the parallel and antiparallel configurations of a SV.** The ferromagnetic layers are represented by the blue layers and the nonmagnetic layer for a orange layer. Red arrows illustrate the magnetization of each ferromagnetic layer.

This effect was first discovered by William Thomson in 1856 and it is known as ***anisotropic magnetoresistance*** (AMR).

2.3.1 Giant Magnetoresistance

A Spin-Valve (SV) is a magnetic structure which consists of two ferromagnetic thin layers separated by a nonmagnetic layer which avoid the direct exchange coupling between the ferromagnetic layers. The resistance of a SV depends on the relative orientation of the magnetization of the two ferromagnets, Fig.2.5.

For example, two possible magnetic configuration of the SV is the parallel (P) and the antiparallel (AP) configuration. These configurations have different resistance. The parallel one has low resistance and the antiparallel one has high resistance. This effect is known as Giant Magnetoresistance and it was discovered independently by Albert Fert and Peter Grunberg in 1988 [1, 2]. Then, they received the Nobel Prize in Physics in 2007 for their work. It was an important discovery for the development of compact hard disks used, for example, in computers and some music players.

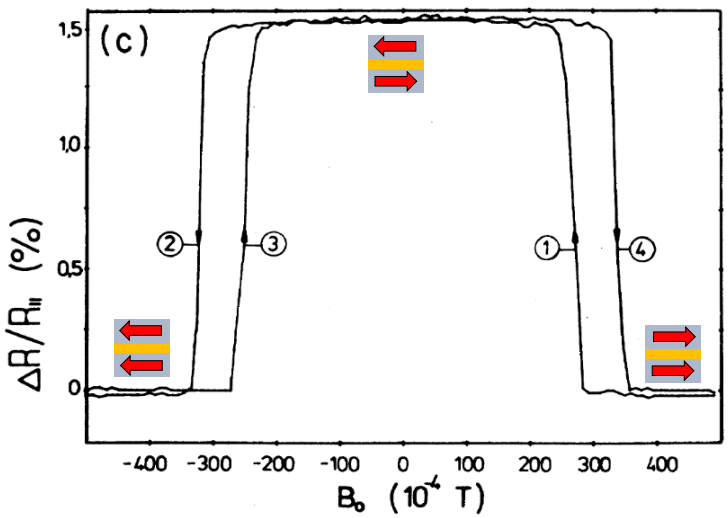

Figure 2.6: **First measurement of the GMR effect.** Magnetoresistance from Fe double layers with anti-ferromagnetic coupling. This means that at zero field the system prefers the antiparallel configuration. By increasing the field, one of the magnetic layer reverses the direction of the magnetization and makes the system to get the parallel configuration. Adapted from [1]

Figure 2.6 is the original work of Peter Grunberg and shows magnetoresistance as a function of in plane magnetic field. At zero magnetic field, that system prefers the antiparallel configuration. However, an applied in-plane magnetic field can switch the direction of the magnetization and get the parallel configuration in both directions.

There are two methods to measure the GMR effect by performing current in plane (CIP) measurement or by performing current perpendicular-to-plane (CPP)measurement, 2.7. There are some advantages of the CIP measurement on thin-film multilayers. First, it is much easier to fabricate the samples than for CPP and therefore we could make and study many sample with different thicknesses. Second, it is convenient to compare with theoretical description due to the translational symmetry in the multilayer plane. However, the CPP magneto-transport on nanopillars has practical and fundamental importance and has been widely studied in the past two decades.

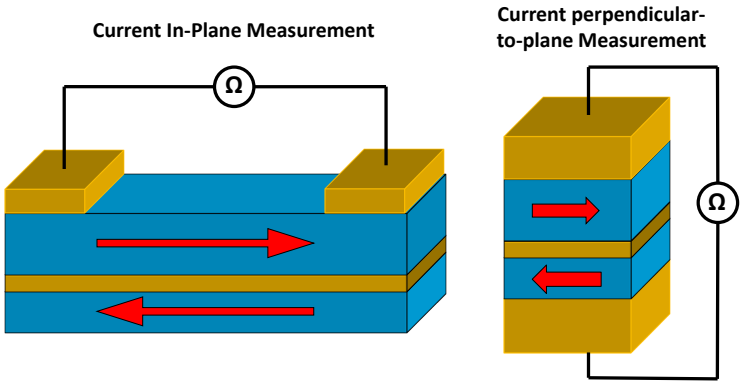

Figure 2.7: **Current in plane and current-perpendicular-to-plane configurations of a GMR SV.** In the left geometry the leads are at the same side of the multilayer making these devices much easier to fabricate than the right geometry which has the leads at opposite side of the multilayer

2.3.2 Tunnel Magnetoresistance

Tunnel magnetoresistance (TMR) can be observed if the metallic spacer of a CPP GMR SV is changed by an ultra thin isolator material such as Al_2O_3 and MgO. This effect is a result of spin polarized quantum tunneling across the isolator material. Similar to GMR, the resistance of the P and AP configurations are different where $R_P < R_{AP}$. This kind of spin valve with isolator spacer is known as magnetic tunnel junction (MTJ). TMR is much higher than GMR, which made TMR an attractive possibility for the next generation of memory devices. In addition, high MR allow us to study the magneto-dynamic phenomena in nanoscale ferromagnets. For example, spin wave modes and the effect of the spin torque on the ferromagnet.

Bibliography

[1] G. Binasch et al. “Enhanced magnetoresistance in layered magnetic structures with antiferromagnetic interlayer exchange”. In: *Phys. Rev. B* 39.7 (1989), pp. 4828–4830. ISSN: 01631829.

[2] M. N. Baibich et al. “Giant Magnetoresistance of (001)Fe/(001)Cr Magnetic Superlattices”. In: *Phys. Rev. Lett.* 61 (21 1988), pp. 2472–2475. URL: https://link.aps.org/doi/10.1103/PhysRevLett.61.2472.

[5] Wh Meiklejohn and Cp Bean. “New Magnetic Anisotropy”. In: *Phys. Rev.* 105.3 (1957), pp. 904–913. ISSN: 0031-899X. URL: http://prola.aps.org/abstract/PR/v105/i3/p904{_}1{\%}5Cnhttp://link.aps.org/doi/10.1103/PhysRev.105.904.

Chapter 3

Background Theory: Superconductivity

Superconductivity phase is one of the states that many metals and alloys can enter below a critical temperature. This is characterized by two effects: zero electrical resistance and perfect diamagnetism. The first effect was discovered by Kamerlingh Onnes in 1911 with the technique of liquefy helium found that mercury has zero electrical resistance below a critical temperature (T_c) of 4.2K. The second effect was discovered by Meissner and Ochsenfeld in 1933. They found that superconductors behave as perfect diamagnets and therefore magnetic flux is completely zero inside of a superconductor. Almost 40 years after the discovery of superconductivity a phenomenological theory was given by Ginzburg and Landau in 1950. They described the superconducting state through a macroscopic wave function which represent a couple of electrons. Then, in 1957 Bardeen, Cooper, and Schrieffer created a microscopic theory of superconductivity. This fascinating quantum-mechanical model is known as BCS Theory. In addition, many other such as London, Josephson, Bogoliubov, Abrikosov, and Andreev made an enormous contribution to have an adequate theoretical picture of conventional superconductivity.

3.1 Phenomenological Theory of superconductivity

3.1.1 Meissner-Ochsenfeld Effect and London Equation

One effect which is a result of the zero electrical resistance is the absence of magnetic flux inside of a superconductor, even in the presence of a external magnetic field. However, Meissner and Ochsenfeld found experimentally that the superconductivity is destroyed in the presence of an applied field higher than a critical magnetic field (H_c) and therefore the magnetic flux can penetrate the entire sample. They also found a reversible transition, it means that the superconducting state and normal state of the sample are in equilibrium at critical magnetic field. This also means that it is equivalent any way to go from the normal state without a external magnetic field to the superconducting state with a small external magnetic field (lower than H_c). For example, first cold down to get the superconducting state and then applied the small magnetic field is equivalent to first applied the small magnetic field and then cold down the sample. The first path is totally explicable with the fact of zero resistivity. However, the second path is unique property for superconducting materials (expulsion of the magnetic field). This is the very known Meissner-Ochsenfeld Effect. The fact that the magnetic flux is zero inside of superconductor implied that $H = -4\pi M$ which is equivalent to say the susceptibility of a superconductor is $\chi = -1/(4\pi)$. This is the reason why a superconductor can be thought as a perfect diamagnet.

In 1961 London proposed an equation to explain the perfect diamagnetism and the Meissner effect of a superconductor.

$$\vec{B} + \lambda_L^2 \vec{\nabla} \times \vec{\nabla} \times \vec{B} = 0$$

where λ_L is known as the London penetration depth and is given by $\sqrt{\frac{mc^2}{4\pi\mu ne^2}}$. With this equation it is possible to infer that the perpendicular component of the magnetic flux is completely vanished at the surface of a superconductor. However, the parallel component decay exponentially into the superconductor in a scale of λ_L.

3.1.2 Ginzburg-Landau (GL) theory

They proposed that the superconductivity is due to a population of superconducting electrons whose density vanishes at the superconducting transition temperature (T_c). They express the density in term of a macroscopic wave function as $n = |\Psi|^2$. Based in the Landau's general theory of second-order phase transformations and the interaction between the vector potential and the wave function, they suggested the free energy to be

$$f = \int \frac{d\vec{r}}{V}\alpha|\Psi|^2 + \frac{\beta}{2}|\Psi^4| + \frac{1}{8\pi}B^2 + \frac{1}{2m^*}\left|\left[\frac{\hbar}{i}\vec{\nabla} + \frac{e^*}{c}\vec{A}(\vec{r})\right]\right|^2 \tag{3.1}$$

where e^* is the effective charge. In 1961 Deaver and Fairbank [6] and Doll and Näbauer [7] discovered experimentally that the effective charge is $2e$. The fact that $e^* = 2e$ suggests that superconductivity is due to a pair of electrons. The minima of the free energy gives the equilibrium states of the system. Minimizing the Ginzburg-Landau free energy independently with respect to the vector potential and the macroscopic wave function gives rise to the

Ginzburg-Landau equations

$$\vec{j}(\vec{r}) = -\frac{2e\hbar}{2im^*}\left[\Psi^*\vec{\nabla}\Psi - \Psi\vec{\nabla}\Psi^*\right] - \frac{4e^2}{m^*c}\vec{A}\Psi^*\Psi \tag{3.2}$$

$$0 = \left[\alpha + \beta|\Psi|^2 + \frac{1}{2m^*}\left(\frac{\hbar}{i}\vec{\nabla} + \frac{e^*}{c}\vec{A}\right)^2\right]\Psi \tag{3.3}$$

with boundary condition

$$\hat{n}\cdot\left(\frac{\hbar}{i}\vec{\nabla} + \frac{e^*}{c}\vec{A}\right)\Psi = 0 \tag{3.4}$$

solving the GL equations is possible to get the London equation and therefore the London penetration depth in terms of GL's parameters as $\lambda_L^2 = \frac{m^*c^2\beta}{4\pi|\alpha|(2e)^2}$. In addition of this length, GL equations depend on the spatial variation of Ψ (order parameter). This length is known as coherence length and is given by $\xi^2 = \frac{\hbar^2}{2m^*|\alpha|}$. The critical field can also be expressed by GL's parameters as $H_c = \sqrt{\frac{4\pi}{\beta}}\alpha$

3.1.3 Type I and II S.C.

The GL theory is very successful to explain the existence of two types of superconductors. In 1957 Abrikosov published a study showing the existence of new type of superconductor which he called Type II. These superconductors have a seconds critical field (H_{c2}) higher than H_c. Therefore, if the sample is below H_c, it is in the superconducting state with the magnetic flux completely expelled from the sample. If the sample is above H_{c2}, it is at normal state and the magnetic flux penetrates completely the sample. Now, if the sample is at a field between H_c and H_{c2}, it will be a mixed state where a superocnductor has some

normal state regions forming vortices where the magnetic field is able to pass through. On the other hand, superconductor type I do not have this second critical field or saying in different way $H_{c2} < H_c$ therefore there is not mixed state because below H_c the sample is completely superconductor. In term of GL's parameters this can be said as

$$\frac{H_{c2}}{H_c} = \sqrt{2}\kappa \tag{3.5}$$

where $\kappa = \lambda/\xi = \frac{m^* c}{e\hbar}\sqrt{\frac{\beta}{8\pi}}$. Then, if $\kappa < 1/\sqrt{2}$ the superconductor is Type I and if $\kappa > 1/\sqrt{2}$ the superconductor is Type II.

3.2 Microscopic Theory of Superconductivity

3.2.1 BCS and Bogoliubov model Hamiltonians

Bardeen, Cooper, and Schrieffer proposed a very successful model of superconductivity. This model consist of pairs of electrons with opposite spins and wave vectors, and therefore with zero center of mass momentum. Latter, in 1958 Bogoliubov proposed a model for a superconductor in a external magnetic field. This model Hamiltonian was a modify version of the BCS model Hamiltonian. Here the center of mass of the pairs of electrons acquire a finite momentum ($\vec{q}$). The BCS and Bogoliubov model Hamiltonians are

$$H_{BCS} = \sum_{\vec{k},\sigma} \epsilon_{\vec{k}} \hat{c}^\dagger_{\vec{k}\sigma} \hat{c}_{\vec{k}\sigma} + \sum_{\vec{k}\vec{k}'} U_{\vec{k}\vec{k}'} \hat{c}^\dagger_{\vec{k}\uparrow} \hat{c}^\dagger_{-\vec{k}\downarrow} \hat{c}_{-\vec{k}'\downarrow} \hat{c}_{\vec{k}'\uparrow} \tag{3.6}$$

$$H_{Bogoliubov} = \sum_{\vec{k}\vec{k}'\sigma} \epsilon_{\vec{k}\vec{k}'} \hat{c}^\dagger_{\vec{k}\sigma} \hat{c}_{\vec{k}\sigma} - \sum_{\vec{k}\vec{q}\vec{k}'} \frac{U_0}{V} \hat{c}^\dagger_{\vec{k}\uparrow} \hat{c}^\dagger_{\vec{q}-\vec{k}\downarrow} \hat{c}_{\vec{q}-\vec{k}'\downarrow} \hat{c}_{\vec{k}'\uparrow} \tag{3.7}$$

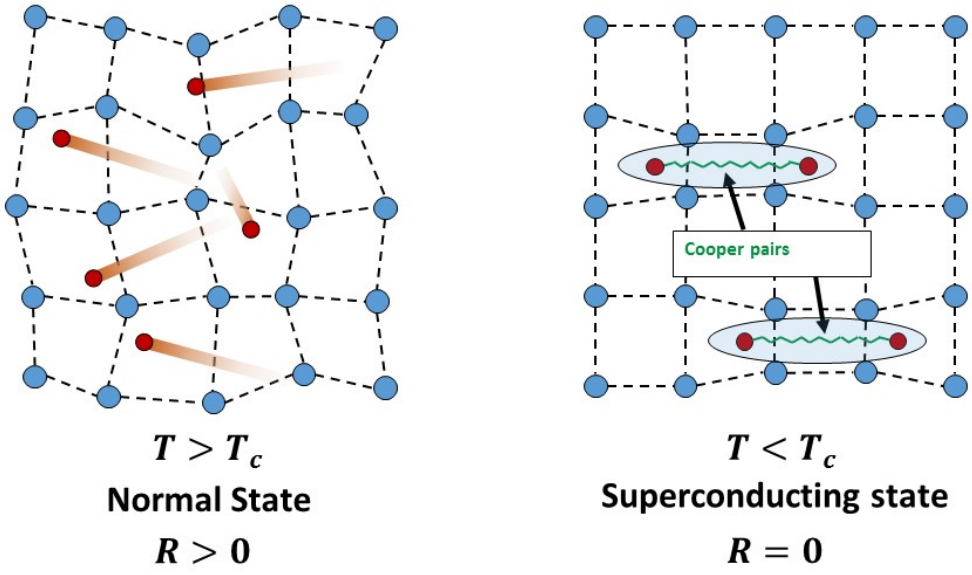

Figure 3.1: **Schematic of a metal in the Normal and superconducting states.** This schematic represents a piece of metallic lattice, the atoms are represented by blue circles and conduction electrons by red dots. Left panel represent the normal state and the right panel the superconducting state.

these hamiltonians describe the dynamics of a pair of electrons. This pair is known as Cooper pair because Cooper was the first person to show that a small attractive interaction between electrons in a metal can bind electrons into pairs.

3.2.2 Cooper pair

The concept of Cooper pair presented in this thesis is for conventional superconductor such as Nb and Ta. This excludes other kind of superconductivity like High-Temperature superconductor. Figure 3.1 shows a schematic representation of the interaction between a lattice of atoms of a metal (blue circles) with its conduction electrons (red circles). If this metal is at a temperature higher than the critical temperature, it behaves like a normal metal. So its conduction electrons encounter resistance, which is caused by collisions and scattering as the particles move through the vibrating lattice of metal atoms. Instead, at low temperature

below a critical temperature, the lattice of atom has coordinated movements with the conduction electrons. This interaction between the electron and the movement of the lattice, known as electron-phonon interaction, creates a small attraction among the electrons. This small attraction is enough to make the electrons condensate in pairs (Cooper pair) and move freely through the metal without resistance.

Cooper pair as a quantum mechanic system is described by a wavefunction. In principle, there are four spin states for a electron pair: $\uparrow\uparrow$, $\downarrow\downarrow$, $\uparrow\downarrow$, and $\downarrow\uparrow$. However, the total wavefunction of a system of two electrons has to be antisymmetric or odd with respect to exchange of the two electrons. The wavefunction can be separated in two parts.

$$\Psi(r_1, s_1; r_2, s_2) = \psi(r_1; r_2) S(s_1, s_2) \tag{3.8}$$

$\psi(r_1; r_2)$ is the orbital part which describe the distribution of the particles in the space and $S(s_1, s_2)$ is the spin part which describe the spin of the particles of the system. In order to have odd wavefunction, one of the parts has to be odd and the other even. Therefore, we have two possibilities: one where the spin part if even and the other where the spin part is odd. In the case of the spin part is even, we have three possible function which are even: $\uparrow\uparrow$, $\downarrow\downarrow$, $\uparrow\downarrow + \downarrow\uparrow$. These three components are called triplet. In the case of the spin part is odd, there is only one possible wavefunction which is odd or antisymmetric: $\uparrow\downarrow - \downarrow\uparrow$. This is called singlet. In principle all these four component could be present in a superconductor. However, in a conventional superconductor the orbital part is symmetric (s-wave), then only the singlet condensation is present. In other words, superconducting correlations in conventional superconductors form Cooper pairs with anti-aligned spins.

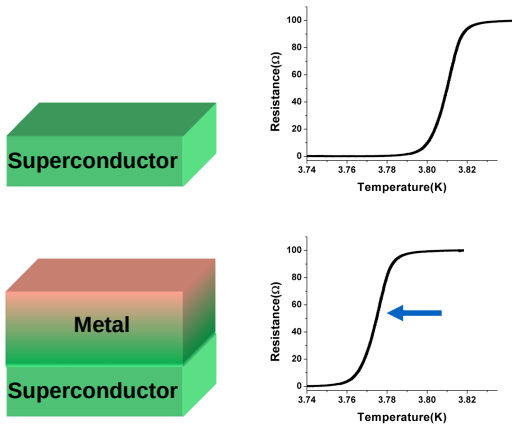

Figure 3.2: **Suppression of the superconducting transition temperature.** This schematic represents how the penetration of the Cooper pair can change the superconducting transition temperature

3.3 Superconducting Proximity Effect

The superconducting proximity effect is the key concept of this work. It has been studied intensively because in proximity structures was possible to see some effects which were not observed in bulk materials. Figure 3.2 shows a phenomenological description of the proximity effect. This schematic representation is relevant for understanding the experimental procedure and results. Figure 3.2(a) shows the representation of a superconductor thin film and its superconducting transition temperature curve, then if there is a metal in proximity, the superconducting transition temperature decrease, Fig 3.2(b). The reason is that there is penetration of the condensate into the non-superconducting layer. Then, part of the non-superconducting layer becomes superconducting by proximity. The price of this transformation is that the whole structure has a lower superconducting transition temperature. So, in simple words, more penetration of the condensate, lower superconducting transition temperature.

Penetration of the condensate depends on the characteristic of the metal such as thickness or the magnetic properties. The proximity effect between a conventional superconductor and

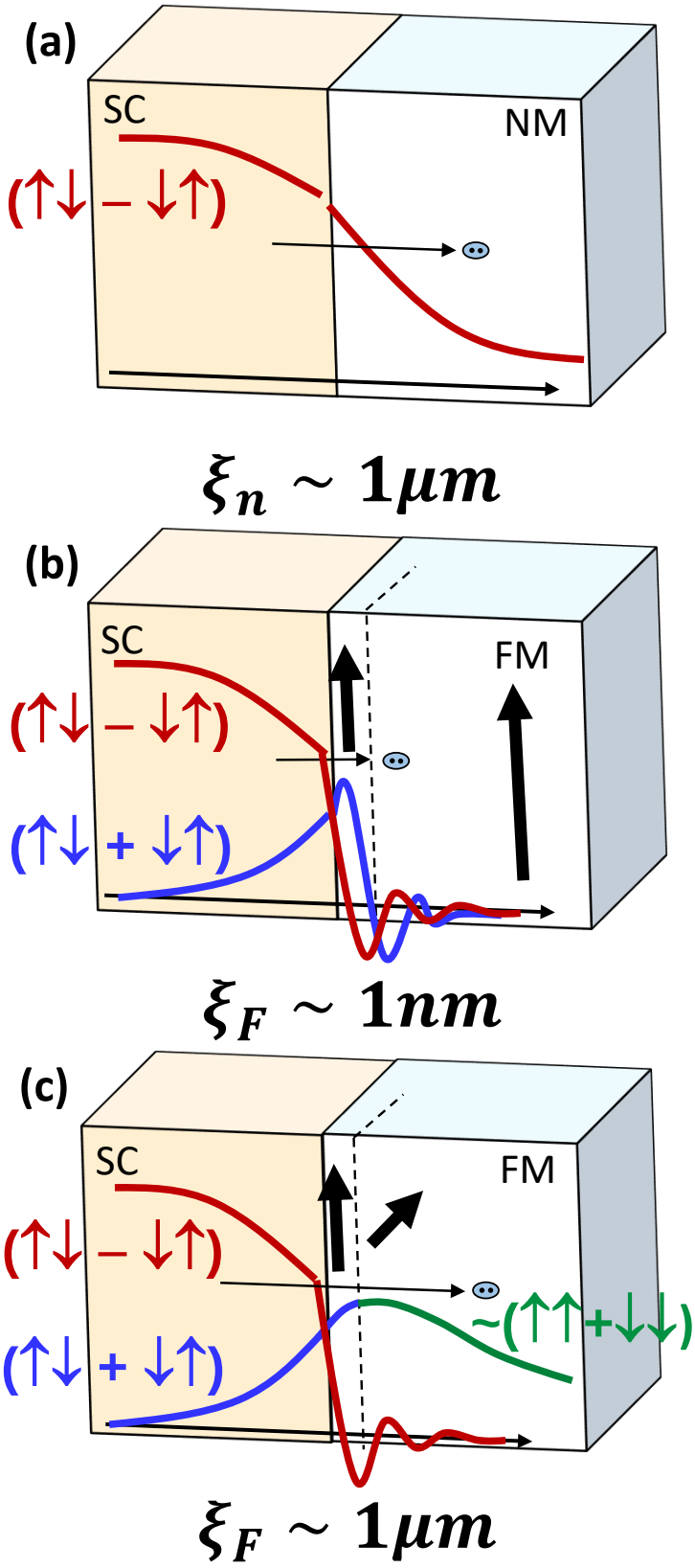

Figure 3.3: **Superconducting proximity effect between a conventional superconductor and a metal:** (a) nonmagnetic metal, (b) ferromagnetic metal with collinear magnetization, and (c) ferromagnetic metal with noncollinear magnetization.

a nonmagnetic metal (Fig.3.3(a)), the singlet Cooper pair amplitude decays monotonically into the nonmagnetic metal in a long range of the order of 1μm.

If the nonmagnetic metal is replaced by ferromagnetic metal, the scenario is quiet different. Superconducting correlations in conventional superconductor form Cooper pairs with anti-aligned spins, while the exchange interaction in the ferromagnetic metals tends to align the spins of the conduction electrons which produce the pair breaking. As a result of the competing interactions, the Cooper pair can not penetrate deep into the ferromagnet. In other words, the proximity effect induces short range state of the order of 1 nm.

However, this is not the end of the story, the real situation is much more complex and interesting. When there are magnetization collinearities (Fig.3.3(b)), each electron of the singlet Cooper pair acquire a different momentum due to the exchange splitting of the conduction band in the ferromagnet layer. Then, the Cooper pair have a finite momentum which produces a change in the amplitude of the cooper pair. By using the Eulers formula, the pair wavefunction can be rewritten as a mixture of singlet and triplet spin states with zero spin projection.

$$(\uparrow\downarrow - \downarrow\uparrow) \rightarrow (\uparrow\downarrow e^{iQ\cdot R} - \downarrow\uparrow e^{-iQ\cdot R}) \tag{3.9}$$

$$\rightarrow (\uparrow\downarrow - \downarrow\uparrow)\mathrm{Cos}(\mathrm{Q}\cdot\mathrm{R}) + i(\uparrow\downarrow + \downarrow\uparrow)\mathrm{Sin}(\mathrm{Q}\cdot\mathrm{R}) \tag{3.10}$$

The new state has a oscillatory behavior in space inside of the ferromagnet. The state is known as FFLO state. It was predicted by Peter Fulde and Richard Ferrell and by Anatoly Larkin and Yurii Ovchinnikov. The S/F proximity effect has an important consequence inducing singlet to Triplet conversion process.

The amplitude of this proximity-induced triplet state depends on the state of magnetization of the ferromagnet. When there are magnetization noncollinearities (Fig.3.3(c)), the proximity effect induces all three components of the triplet condensate. Because there is no preferred quantization axis (and neither the total spin S of the Cooper pairs nor its z-component are conserved). The components with parallel spins are immune to pair breaking by the exchange field and, they can penetrate deep into the ferromagnet and give rise to the long-range triplet component in the ferromagnet of the order of 1μm.

Bibliography

[6] Bascom S. Deaver and William M. Fairbank. "Experimental Evidence for Quantized Flux in Superconducting Cylinders". In: *Phys. Rev. Lett.* 7 (2 1961), pp. 43–46. URL: https://link.aps.org/doi/10.1103/PhysRevLett.7.43.

[7] R. Doll and M. Näbauer. "Experimental Proof of Magnetic Flux Quantization in a Superconducting Ring". In: *Phys. Rev. Lett.* 7 (2 1961), pp. 51–52. URL: https://link.aps.org/doi/10.1103/PhysRevLett.7.51.

Chapter 4

Fabrication

4.1 Introduction

This chapter explains some of the most standard procedures used to fabricate nanodevices in Krivorotov's group. All tools mentioned here are available in Krivorotov's lab, the Irvine Materials Research Institute (IMRI), the Bio-Organic Nanofabrication facility (BiON), and the Integrated Nanosystems Research Facility (INRF). The last three are shared facilities at UCI, where BiON and INRF are cleanrooms. In general, there are four main tasks in the fabrication: deposition, etching, lithography and characterization. The tools used for these tasks, at the moment of writing this thesis, are:

For Deposition

1. AJA magnetron sputtering system (Krivorotov's lab). It is the most used deposition method in the group and primarily used for depositing multilayers, although it is also used for the deposition of leads.

2. Angstrom Engineering EvoVac Glovebox Evaporator (IMRI). This is a thermal and electron beam evaporator with a variable angle substrate stage appropriate for glancing angle deposition (GLAD) technique. This tools is mainly used for deposition of leads and hard masks. There is another old evaporator in INRF (considered as a backup).

3. Plasma-Therm 790 (INRF). This is for depositing dielectrics through Plasma Enhanment Chemical vapor Deposition (PECVD). Dielectrics are useful for electrically insulating some part of the devices such the top and bottom leads of a pillar.

For Etching

1. Intlvac's Nanoquest I (Krivorotov's lab). This is an ion milling system and the most used tool for etching in the group. The etching process is anisotropic (uniform in one direction) which make suitable for fabricating very small well-defined devices such as nanopillars and nanowires.

2. AJA magnetron sputtering system (Krivorotov's lab). Used for plasma cleaning substrate and for etching prior lead deposition. The etching process is isotropic (uniform in all directions).

3. Chemical wet benches (BiON). Chemical etching is a great option to make a selective etching process. For example, buffered oxide etching (BOE) can easily etch oxides but not metals. In our group it has been used to etch SiO_2. Chemical etching of metals can also be done on the wet benches; particularly for Cu, Au, and Cr. For example, removing the metallic film used for e-beam lithography on semiconductor substrates. It can be also useful for making large devices that are sufficiently large and not sensitive to the poor resolution achieved for this method such as leads.

For Lithography

The lithography consist of three steps: spin coat the sample, write the pattern, and develop the resist. The spin coating and development can be performed in Krivorotov's lab, BiON, or INRF. For the writing:

1. FEI Magellan 400 XHR SEM (IMRI). This is a Scanning Electron Microscope (SEM) with the possibility of making e-beam lithography (EBL). It is the best option at UCI for EBL. There is also a low resolution SEM in INRF for EBL and another in IMRI but it has not been used by Krivorotov's group members.
2. Karl Suss MA6 Mask Aligner (INRF). For photolithography when the alignment is required. There is another Mask aligner in BiON but it is not as good as the one in INRF.
3. UV Flood exposure system (INRF and BiON). For photolithography without alignment.

For Characterization

1. Rigaku SmartLab X-ray Diffractometer (IMRI). This tools can be use to make x-ray diffraction (XRD) characterization to study the crystallographic structure of the films and for measuring the thickness of them using X-ray reflectivity (XRR) technique.
2. FEI Magellan 400 XHR SEM (IMRI). To have a view of the sample in during different stages of fabrication. This SEM enables sub-nanometer resolution images by using the immersion mode. There are at least 6 other SEMs available at UCI, but this is the best for imaging.
3. FEI Quanta 3D FEG Dual Beam SEM-FIB (IMRI). To cut site-specific cross-sections using the Focused Ion beam (FIB) characteristic and then view with the SEM.

4. PNI Nano-R AFM (IMRI). This is an Atomic Force Microscope (AFM) which can image an object's surface topography. The resolution is better than 2 nm in the X-Y plane and 0.13 nm in the Z-dimension.

5. Filmetric F40 (IMRI). This is used specially to measure thickness of dielectric films such as SiO_2, MgO and Al_2O_3. It can be also used to measure thickness of very thin metallic films.

6. Optical Microscopes (Krivorotov's lab, BiON, and INRF).

4.2 General aspect of fabrication

This section gives some details of the steps crucial for the fabrication of nanodevices.

4.2.1 Clean sample

This step is very common in the fabrication process. For example, to remove the photoresist or e-beam resist from a sample, or if a sample gets dirty in any step and needs to be cleaned. The standard way to do this is:

1. Take two clean glass beakers and fill one with acetone and the other with IPA.

2. Place the sample in the beaker with acetone and sonicate for 3 min. If the sample is big, like a 4-inch wafer, first spray acetone by swinging the jet around the sample surface above a big beaker to collect the acetone and residues, and then place the sample in the beaker with acetone to sonicate.

3. Transfer the sample to the beaker with IPA and sonicate for 3 min. The transfer from acetone to IPA has to be very quick to avoid the acetone dry in that process. Because

acetone dries ultra fast it is recommended to spray IPA on the surface of the sample during the transfer.

4. Dry with N_2 gas by holding the sample with tweezers over a clean beta wipe. Keep the direction of the gas in one direction in order to have all residues go towards only one side of the sample. For small samples, it is not critical but for big ones (4-inch wafer) it is recommended to do so. The idea is then use the same side for the next cleaning processes.

Extra sonication is totally fine if the sample has a good adhesion layer. However if the multilayer does not have an appropriate adhesion layer, the multilayer can peel off. In fact, this method can be useful to test the adhesion layer. If the multilayer peels off very easily in the order of 10 min, then it might be better to find an alternative before starting the fabrication process. Sonication for many hours will remove even good adhesion layers.

4.2.2 Dicing

Dicing is a step which can be done at the beginning, middle or at the end of the process of fabrication. Dicing SiO_2 is a dirty task, there are many particles that can land on the surface of the sample and become difficult to remove after that. To prevent this issue, it is better to protect the sample with lithographic resist, such as photoresist, PMMA, or MMA. The best protection is with photoresist because it tends to be much thicker (on the order of 1 μm) than e-beam resist (on the order of 100 nm), as well as to be much easier to remove. If spin coat photoresist is not an option, hold the sample with tweezers and then just pour some drops of photoresist on the sample and spread them by moving the sample until the surface is fully covered. It should be done this inside of a big beaker to collect the runoff during the spreading. After the spin coat or the spread of photoresist, dry the resist on a hot plate or in an oven for a few minutes. If the sample is a new substrate or a multilayer

film without any pattern, it is recommended to draw the design of the dicing lines on the back side of the sample before dicing. It is also recommended to label each piece to know the relative position in the original sample. This is particularly useful for multilayer films because they are usually nonuniform. To have a permanent label, use a scriber and write a label ultra gently. The label will keep even if the sample is cleaned as described in Sec.4.2.1. The procedure to dice is:

1. Place the sample on a beta wipe.
2. Scratch the sample along the edge of a glass slide using a diamond scriber.
3. Blow with N_2 gas to remove all particles around the scratch.
4. Place the sample on a glass slide and another glass slide on top of the sample making a sandwich. The scratch and the edges of the glass slides must be aligned.
5. Place a third glass slide on the part of the sample which is out of the sandwich and align it with the scratch line.
6. Press the two glass slides which are on top of the sample to dice it.

It can be also used a clean metallic rule, instead of a glass slide for big samples like 4-inch wafers. Store the new small samples with the photoresist to have extra protection. If it is necessary to polish the edges of the new small samples, it can be done before removing the photoresist. Finally, remove the photoresist by following Sec.4.2.1 just before using them.

4.2.3 Sputtering deposition

Sample holder

There are multiple ways to place chips and wafers on the sample holder. The easy and most versatile is with clamps, for example, it is the only option to make high temperature deposition. However, for some application, vacuum-safe single- or double-sided polyimide (Kapton) tape is the best option. For instead, for a very small sample where the shadow created by the clamps (approximately 1 mm radius) are relevant. It is extremely important to remove all bubbles in the tape because they can expel trapped air once the sample is inside of the main chamber and increase the base pressure. Double sided tape is preferable, in that sense, because it is easier to remove the bubbles. The procedure to use double sided tape is:

1. Cut a small piece of double sided tape, approximately 1/9 of the area of the sample.
2. Peel off the plastic protection of one side of the double sided tape.
3. Stick it on the sample holder such that the other plastic protection is facing up.
4. Remove all possible bubbles by sliding the back side of a tweezers on the tape which is still protected by the other plastic.
5. Peel off the second plastic protection.
6. Place the sample on the tape such that the center of the sample is on the tape.
7. Press the sample with two tweezers at two opposite corners.

To remove the sample, just apply torque to rotate the sample in the plane of the holder (apply force in the plane of the holder on one corner of the sample).

Conditioning system

Conditioning the chamber is crucial for consistent deposition of a series of samples with similar multilayer stack. For example, varying the thickness of the Co free layer in a Nb/Co/Cu/Co superconductor/spin-valve heterostructures. In a series of samples the idea is to have the same condition possible for each sample to maximize the consistency of the film properties. One way is to sputter three dummy samples before starting the series of real samples. Using the Residual Gas Analyzer (RGA), I figured out that similar results can be obtained by conditioning in situ, which is done by doing three dummy depositions with all shutters closed before depositing on the sample. The condition of the chamber before deposition was similar even if the sample was sputtered at different times in the day. Basically, the conditioning process cleans targets and also reduces the residual gas pressure in the main chamber. Specially the residual gas of water. The step-by-step procedure is:

1. Transfer the sample into the main chamber.
2. Sputter all material needed for the multilayer with the shutters close for 1 min.
3. (Optional) Sputter for 2 min Nb, Cr or Al which are good getter to reduce the pressure even more.
4. Wait 5 min to soak the chamber.
5. Repeat steps 2-4 three times.
6. (Optional) Clean the surface with Ar plasma for 20 sec at 40% RF power.
7. Deposit the multilayer stack on the sample.

This way of conditioning is particularly useful when the depositions are made in different days or weeks. This also allows consistency with future depositions of the same multilayer stack.

"Continuous" deposition

There are two method used in the lab to make the deposition of the multilayer: pre-assist deposition and continuous deposition.

The ***pre-assit deposition*** involves two software-layers for each real layer deposited. The first software-layer is to ignite the plasma for the specific material. This can be usually done by setting high pressure (e.g. 20 mTorr) and high power (30 to 50 %). Although, for RF source is better to increase the ramp up/down time, instead of the power. If the plasma is still not ignited, consider to ignite first another gun which is known to ignite easily and then ramp up the power of the gun you want to ignite, then once the plasma is ignited turn off the power of the secondary assistant gun. The important is that the pre-assist software-layer has to keep the shutter(s) close all the time and has to set the idle power at the same value as for the deposition (next software-layer). The parameter of the second software-layer (deposition) are: Delay time of at least 5 second to stabilize the pressure (usually 2 mTorr), then set the power needed to deposit the material (in this part the software do not do anything because the power was already set in the pre-assist software-layer), deposit the corresponding time (Coat Time), and finally set the idle power zero. If you have to deposit a multilayer, you should do the same two steps process for each layer you want to deposit (pre-assist + deposition). The great advantage of this method is ease to make the complete multilayer without error. The disadvantage are: the deposition take more time, expend more material, sometimes the plasma does not ignite between depositions. However, the main problem is the possible oxidation and contamination of the deposited layer during the system is waiting for the next layer deposition.

The idea of the ***"continuous" deposition*** is to reduce the time to almost zero between depositions of one layer to the next one. In this way we reduce the possible oxidation for the

remaining O_2 atoms in the system. To make the "continuous" deposition we have to create a software-process with the following software-layers:

1. Pre-assist for the first material.

2. Deposition of the first material (so far is the same procedure as pre-assist deposition), but 30 seconds before turning off the gun, turn on (with the shutter close) the next gun with a ramp up time of 20 seconds. The idea is that the active gun helps to ignite the next one. As soon as the shutter of the first material close, the shutter of the next material opens. It is important to consider the delay between the program send the order and the shutter actually open or close. Unfortunately, that delay depends on the status of the system, so it is not possible to give numbers. Deposit 20 seconds of the second material before going to the next software-layer. In order to do not interrupt the deposition this software-layer must leave idle power same as for deposition and the shutter open. In this way the software goes from one layer to the next one without interruption.

3. Deposition of the rest of the second material (total time - 20 seconds). If there is a third material, ignite the gun 30 seconds before as the previous step. If this is the last material, set the power zero.

The disadvantage are: take more time to make the software-process, and it also has to be checked with a dummy sample before a real deposition. The advantage are: reduce the oxidation between layers, the process is more reliable because the plasma is always ignited.

4.2.4 Deposition Rate Measurement Using XRR

Magnetron sputtering system does not have an in situ method to measure the thickness of the material deposited. However, it is well known to have very stable deposition rates compared

to others technique such as thermal evaporation. In order to have a 0.1 nm accuracy of the layer thicknesses, it is important to have a method that measures the thickness to about the same accuracy. I confirmed the stability of deposition rates in our system via X-ray reflectivity (XRR) measurements. The uncertainties in the layer thicknesses in the multilayer are given by the uncertainties in the deposition rate measurements. We use the thin film reflectometer Rigaku SmartLab for deposition rate calibration. For such a calibration, we deposit ∼20 nm films with 5 nm of Pt or Au protective capping layers (if needed) and measure their thickness with ∼1-2% precision (depending on the material) via fitting XRR spectra. This allows us to establish deposition rates with ∼1-2% precision. Such uncertainty in the deposition rate allowed us to report the thickness of, for example, a 6 nm Cu film with precision of 0.1 nm. Besides its good precision, it does not need any other step like lithography which is necessary for AFM because the XRR spectra is a collection of reflected signals from the whole sample. Perform XRR measurement in the Rigaku SmartLab is straightforward because the system gives you step-by-step instructions. Below are some recommendations for the calibration:

1. Dice a piece of SiO_2 or Sapphire (if needed) of 1x1 cm^2 following Sec.4.2.2.

2. Write all important information of the sputtering process on the box of the sample (time, power, gun #), for example: Nb(1200s50%G3)Pt(20s15%G4). Other information such as z-position, stage temperature, or process pressure can be omitted if you are using standard parameter: z = 10 mm, T = 16 C, and P = 2 mTorr. If not, add it in the name. For example, Pt(20s15%G4T300C), Pt(20s15%G4z14mm), or Pt(20s15%G4P1mTorr).

3. Use the same name of the box for the XRR data file.

4. Use slit 5 mm if the size of sample is 7x7 mm^2 or bigger and 2 mm if the sample is smaller.

5. Run the measurement between 0 to 12 degrees with a step of 0.02 degrees. The time depends on the film. In general, it should be fine with 15 min for measuring thickness, but if you want to have more information such as roughness, run for 60 min.

6. Transfer the files to the lab computer where the software to fit the data is installed (GlobalFit). I made a bank of files in the lab computer with XRR data used for deposition rate calibration of the common material used in the lab, use that bank (folder) to save the data.

7. Use previous data to have a better guess. If not, create the multilayer structure in the GlobalFit software using your best guess.

8. Click refine button to optimize all parameters and get the fitting.

If you plan to sputter in a big substrate like a 4-inch wafer, nonuniformity can be an issue. I recommend to measure the deposition rate in different parts of the wafer. To reduce the time of characterization, you can assume azimuthal symmetry of deposition, so depositing on a strip of SiO_2 substrate covering from the center to the edge of the sample holder is enough to know how the thickness change in the radial direction.

4.2.5 Ion-Mill etching

The standard ion mill parameter used in the lab are shown in Table 4.1.

Etching rate measurement of SiO_2 and Pt

In order to measure the etching rate of metals using different ion mill parameters, it is important to have a reference. SiO2 is a good reference if the Filmetric F40 is used to measure the thickness, and Pt is the best option if the XRR is used to measure thickness.

Beam Voltage	400 V
Beam Current	30 mA
Acceleration Voltage	80 V
Emission Current	34.5 mA
Spin Speed	20 rmp
Stage Temperature	8 C
Base Pressure	5×10^{-7} Torr
Air flow	10 sccm
Duty Cycle	10-30(on-off)

Table 4.1: Ion milling parameters

In addition to being a good material for measuring thicknesses, they are not affected by external conditions such as oxidation. Au is also a good candidate for XRR, but I found Pt to be more reliable. To know the etching rate of these two materials, measure the thickness before and after etching. The thickness of the film etched in the process divide by the etching time gives the etching rate. Obviously, if you want to have more precision in the calculation of the etching rate, you should etch multiple samples for different time and make a fitting of the thickness of the film etched vs time.

Measurement of the etching time of a multilayer

Knowing the etching time is particularly important if the etching needs to stop in a specific end layer. Filmetric and XRR are useful tools for this task. XRR is more precise than Filmetric, but it takes more time and the sample needs to be roughly 5x5 m^2 or bigger. Instead, Filmetric is fast and the sample can be very small. In order to use the Filmetric, it is necessary to know, first, the etching rate of SiO_2 for the ion milling parameters used. Same for Pt if using XRR. In order to save time and avoid reserving the tools twice, follow the steps shown in Fig.4.1 and are described below,

Material	**Angle** *(degrees)*	**Etching Rate** *(nm/min)*	**Material**	**Angle** *(degrees)*	**Etching Rate** *(nm/min)*
Al	80	6	HSQ	45	16
Al_2O_3	45	6.4	MgO	45	2.6
Al_2O_3	80	3	Nb	45	6.6
Au	45	15.5	Nb	80	6
Au	80	22.4	Pt	45	9
Co	45	8.4	Py	45	10.4
Co	80	8.5	SiO_2	45	10.8
CoOx	45	5	SiO_2	80	7.8
$Cr^{(e)}$	45	10	$SiO_2^{(e\,@45^\circ)}$	45	14.5
Cu	45	8.3	Ta	45	5.8
Cu	80	8.5	TaOx	45	3.4
Fe	45	10.5	$Ti^{(e)}$	45	6.2
HSQ	80	9.8	$Ti^{(e)}$	80	3.8

Table 4.2: Etching rate of some material used in lab. The ion milling parameters are the standard, see Table 4.1. $^{(e)}$ means the material is e-beam evaporated

1. Cover with photoresist half of a chip of SiO_2 substrate [or Pt($\sim$20 nm)]. This can be done by lithography or by spreading with Q-tip and drying on a hot plate or in an oven. The covered area will be used as a reference, Fig.4.1(a) [or (e)].

2. Deposit the multilayer on the chip, Fig.4.1(b) [or (f)].

3. Etch the chip until you get into SiO_2 [or Pt], Fig.4.1(c) [or (g)]. You can make a calculation using etching rate of each layer. Table 4.2 show a list of etching rates for different metals using the standard parameters shown in Table 4.1.

4. Remove the photoresist following Sec.4.2.1

5. Measure the thickness of SiO_2 [or Pt] of the reference part (H_{ne}) and the part exposed by the ion beam (H_e), Fig.4.1(d) [or (h)].

6. Calculate the etching time of the multilayer. First, calculate the difference $\Delta H = H_{ne} - H_e$. Then, using the etching rate of SiO_2 [or Pt], calculate the time to etch ΔH

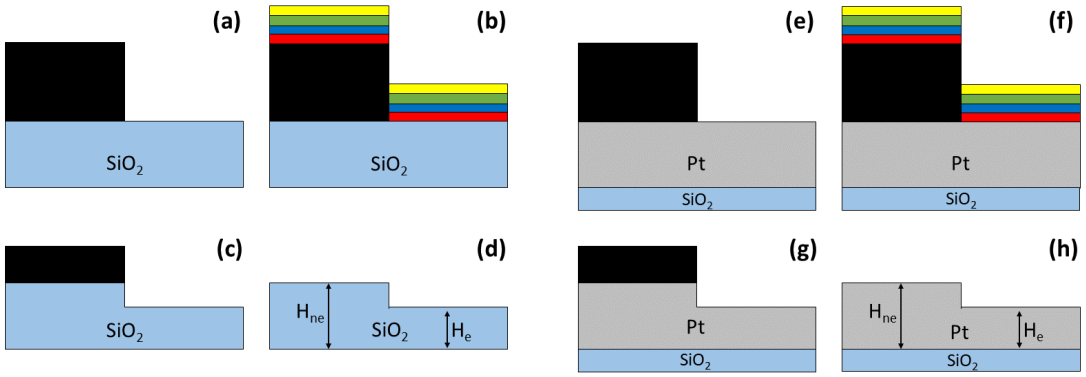

Figure 4.1: **Etching time measurement.** Left panel shows the sequence of steps if a Filmetrics is used to measure the etching time and the right panel if the XRR is used.

($t_{\Delta H} = \Delta H / EtchingRate_{SiO2}$). Finally, subtracting $t_{\Delta H}$ to the total time of etching, get the etching time.

Etching rate measurement of metals and dielectrics

In principle, the same method can be used to calculate the etching rate of Pt to measure, for example, the etching rate of Nb. However, the oxide layer on top of Nb significantly alters the etching time. So to know the etching rate of pure Nb, it is better to protect the surface with 5 nm of Pt or Au. Following the instruction of Sec.4.2.5, calculate the etching time of the multilayer Nb/Pt. Then, subtracting the time to etch Pt, get the time to etch Nb and therefore the etching rate. Now, if Filmetric is used and therefore the deposition of the multilayer Nb/Pt is on top of SiO_2, Nb may oxide by the adjacent SiO_2 layer. To prevent that, measure the etching time of Pt/Nb/Pt, instead. Then substract the corresponding time to etch Pt. It is important to deposit a thick layer of Nb in order to reduce error in the calibration, for example: Nb(40 nm)/Pt(5 nm). If the calibration is critical, consider make a fitting of the thickness vs etching time. Obviously, the same procedure is used for other metals that can oxide. Table 4.2 shows a list of etching rate for different metals using the standard parameters shown in Table 4.1.

4.2.6 E-Beam Lithography

There are three e-beam resists used in this dissertation: MAN, PMMA, and MMA. MAN negative resist is used as hard mask. PMMA and MMA are positive resists which are used to pattern structures followed by a deposition step and a lift-off step. Usually MMA is used a long with PMMA in a bilayer Substrate/MMA/PMMA. This is convenient when the deposition is made by sputtering. One single PMMA has de best resolution among these resists. Figures **??** show some images of small nanowires and nanodot made by MAN resist. Similar size, even smaller can be achieved by PMMA.

Before doing e-beam lithography (EBL), I design and make the NPGS program in Krivorotov's lab. The motivation is to reduce the interaction with the microscope during the lithography due to its likeliness to make mistakes such as not moving the stage between patterns, writing an incorrect pattern, or forgetting to make records. Instead, if you create the program before and save it using the name of the sample and the date of the lithography, you can later see all this information: position, current, dose, etc. Obviously, this is not possible for all applications, so in case there is no way to do this it is recommended to take note of everything possible. Once I have the NPGS program ready, my procedure is the following:

1. Prepare the sample: coat spin the e-beam resist, mount on the sample holder and make a scratch at each corner.

2. Log into the SEM.

3. Open NPGS program in the EBL computer. Sometimes, the computer start an auto DAC calibration. Make sure you don't do anything on the SEM computer or EBL computer during this time. Once completed, it should request a second calibration, press enter on the EBL computer to start it.

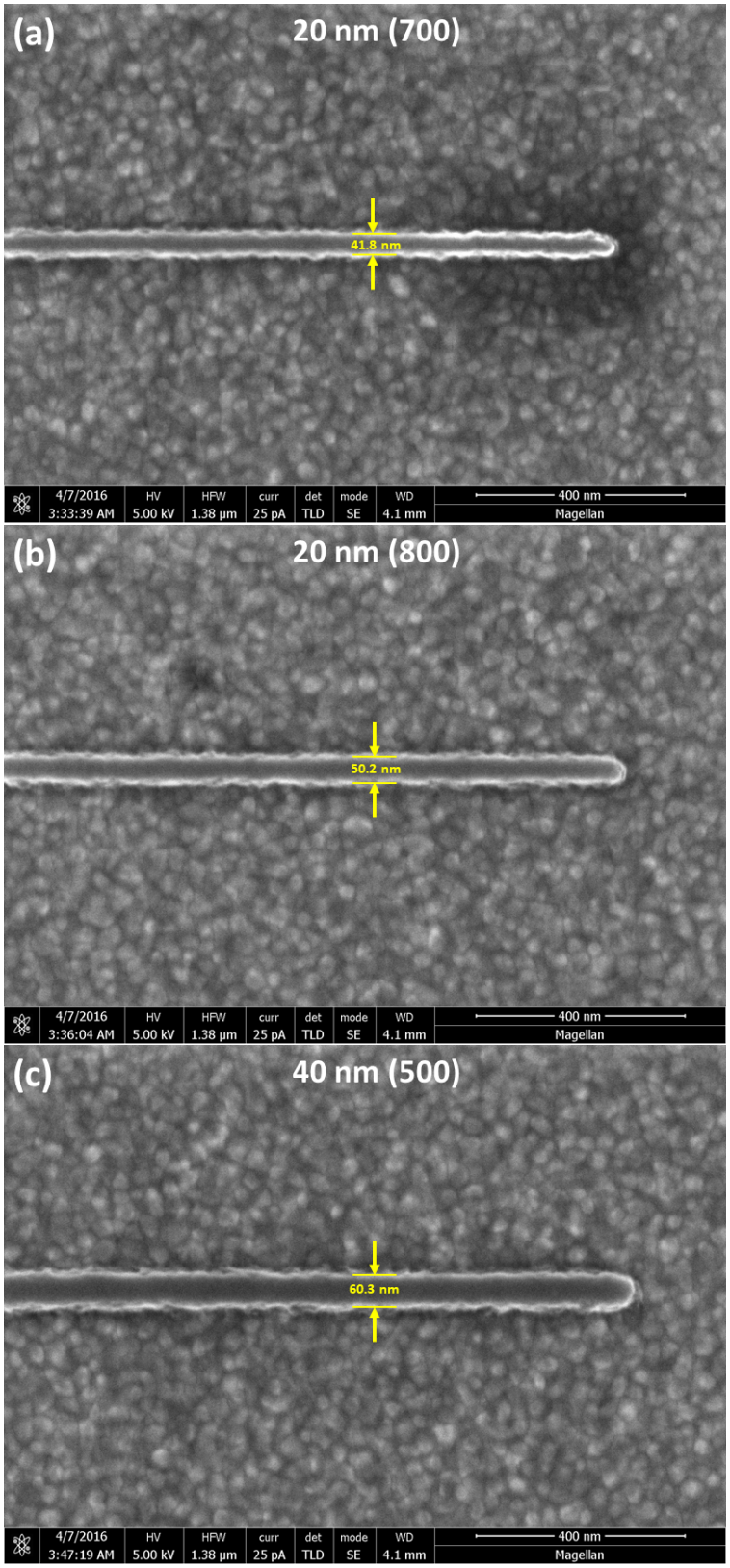

Figure 4.2: **MAN negative resist pattern.** The value on top of the picture is the size of the pattern. The value in parenthesis is the dose used. The result is the size show with the yellow arrows. All three are nanowires.

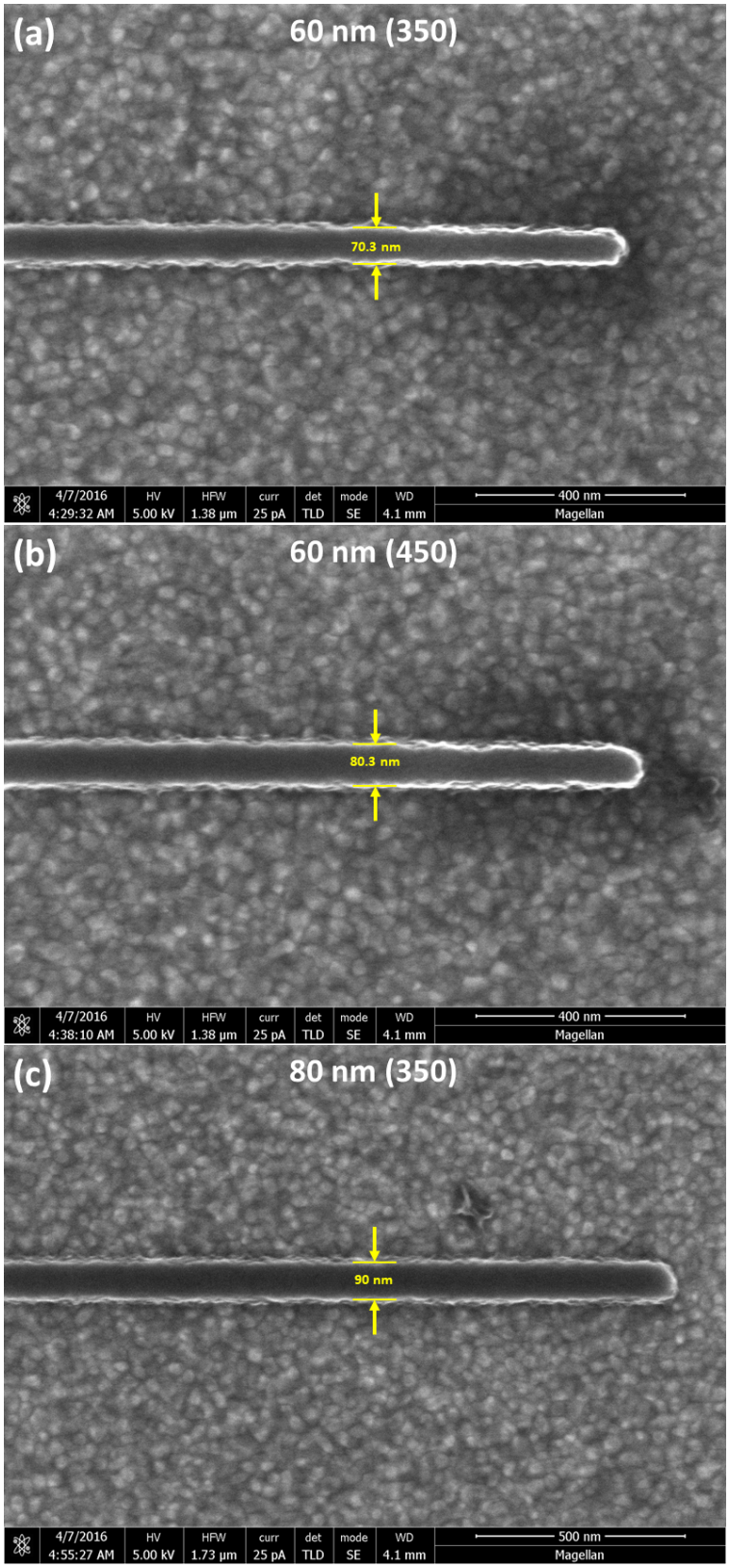

Figure 4.3: **MAN negative resist pattern (cont).** The value on top of the picture is the size of the pattern. The value in parenthesis is the dose used. The result is the size show with the yellow arrows. All three are nanowires.

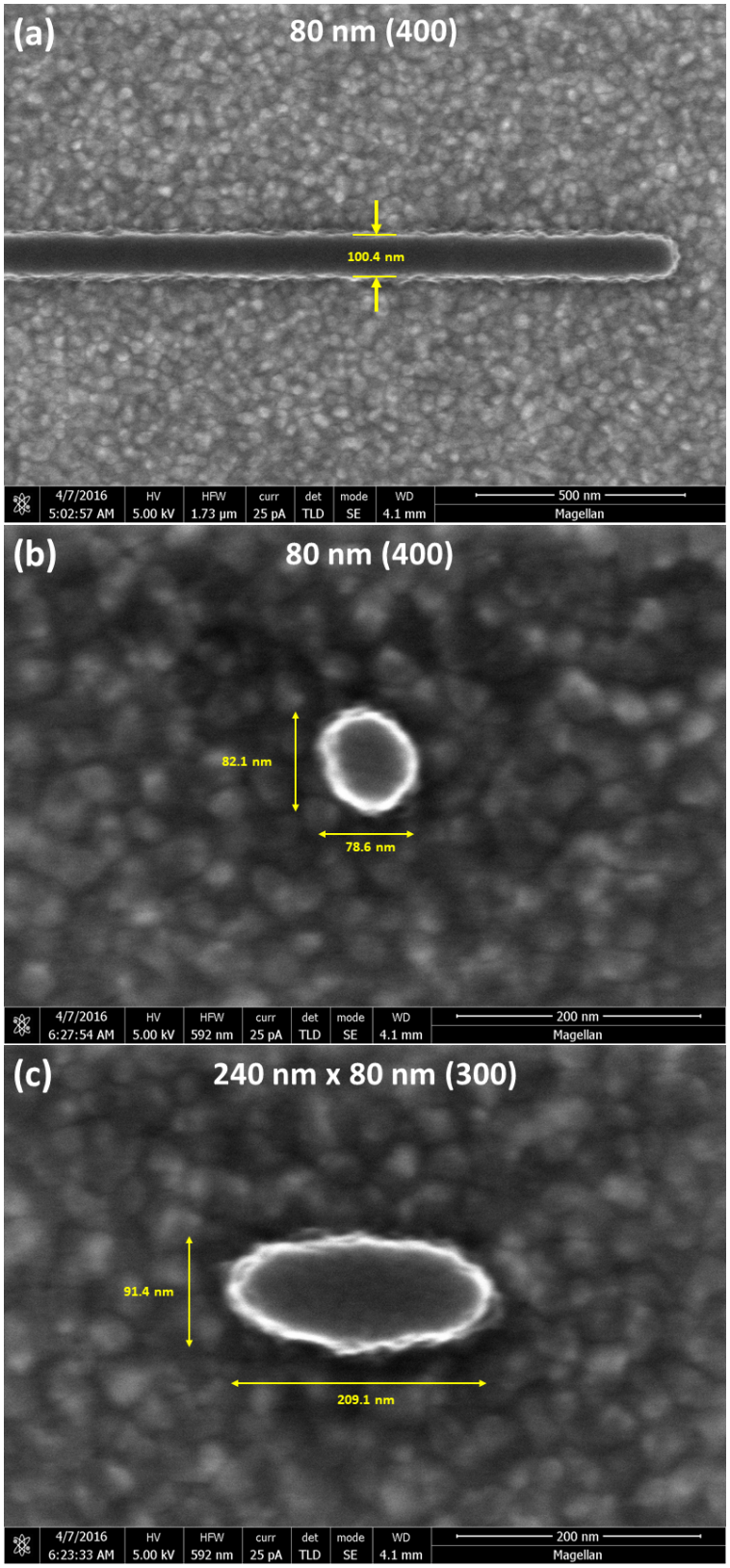

Figure 4.4: **MAN negative resist pattern (cont).** The value on top of the picture is the size of the pattern. The value in parenthesis is the dose used. The result is the size show with the yellow arrows. (a) is a wire, (b) a nanodot, and (c) a nano ellipse

4. Measure the value of the current that will be used in the EBL by using the Faraday cup and the amperimeter next to the SEM. This is to have consistency in the EBL.

5. Load the sample as usual for a SEM session. I recommend loading the sample onto the quick loader holder such that the top edge of the sample faces the chamber when is entering. This avoids the need to reorientate the sample inside of the microscope.

6. Go the the "Stage" drop down menu and select "Take NavCam photo" to take a CCD picture of your sample to aid in positioning the sample.

7. Set the beam current 13 pA and the beam voltage to 30 kV and turn on the beam and focus the beam on the bottom left (scratched) edge of the sample.

8. Click "Link Z-Height" and set the height (z) under the SEM stage position control to 7 mm.

9. Go to the "Stage" drop down menu and select "XT Align Feature". Draw a line going from left to right along the edge of the sample to properly orient the sample. Below in the **"Sample Alignment"** section explains how get better alignment.

10. Go to the position where the lithography will start and save the stage position.

11. Locate a dust particle near the closest scratch.

12. Center the beam for each current that will be used for writing (typically 800 pA and 6400 pA for big patterns) by checking the crossover and then set the current 13 pA again.

13. Get the best image possible (do not spend too much time) by optimizing focus, stigmation, lens modulator, and both stigmator modulators.

14. Select "Direct Stage Control", in the NPGS program, to start the tilt correction program. Follow the instruction of the program. Acquire at least 4 points, one for each

corner, by focusing on a dust particle. Exit out of the protocol by pressing "Enter" twice and then "Esc".

15. Return back to the original position (bottom left) and refocus on the particle.

16. Press the "NPGS" button in the NPGS software and measure the misalignment between current following **"Current misalignment correction"** section below.

17. Write the the corresponding offset in the NPGS program ("Origin Offset").

18. Go to the saved position, step # 10.

19. Run the EBL program.

The position where the EBL starts is typically the center of the bottom edge. However, if this is a second EBL step, it will start in the center of the array. To find the center, first go the the device which is closest to the center and align using the alignment marks of that device. Typically, each device have two set of alignment marks, use the small ones to have more precision. Then, move the stage to the center of the array.

Current misalignment correction

Typically a pattern file (*"pattern.dgs"* or *"pattern.dc2"*) of a device has more than one layer. Each layer is used to write different parts of the device with different currents. For example, big parts of the pattern is convenient to write with very high current to reduce the time of writing, and the small part with low current to have more precision. The problem of working with multiple currents is to consider an overlap between them to ensure continuity. The overlap in general distort the original shape of the pattern. If the application is very critical to this or the idea is to avoid the overlap, pay special attention to the alignment of each current used in the pattern. The procedure is:

1. Set the lowest current that will be used in the pattern.

2. Search a particle as a reference, center the image of that particle and use a zoom larger than 10,000 X.

3. Press the "NPGS" button in the NPGS software and run a program with an alignment pattern as shown Fig. Fig.4.5(a).

4. Check if the particle is in the center of the square, Fig.4.5(a). If not, press the "SEM" button in the NPGS software and recenter the image.

5. Run the same program but change the current in the NPGS program, generally the particle is in a different position, Fig.4.5(b). I recommend to create a NPGS program for each current to avoid to change the program during this step.

6. Move the alignment pattern to have the particle in the same position as in the first image with respect to the pattern, Fig.4.5(c).

7. Record the offset shown in the EBL computer Fig.4.5(d).

8. Use that value (even the sign) as the "Origin Offset" for the corresponding current in all entities of the NPGS program.

Sample Alignment

In particular, in a second or third EBL step, it is crucial to have a better global alignment to save time in the process of alignment. With this it is possible to use only the small set of local alignment marks for each device, instead of performing two local alignment steps. If a misalignment of 1 to 2 μm is fine for your devices, then you can also run a NPGS program which write all pattern without assistance for local alignment for each device. The advantage is significant reduction of the writing time, and avoid human errors if the program

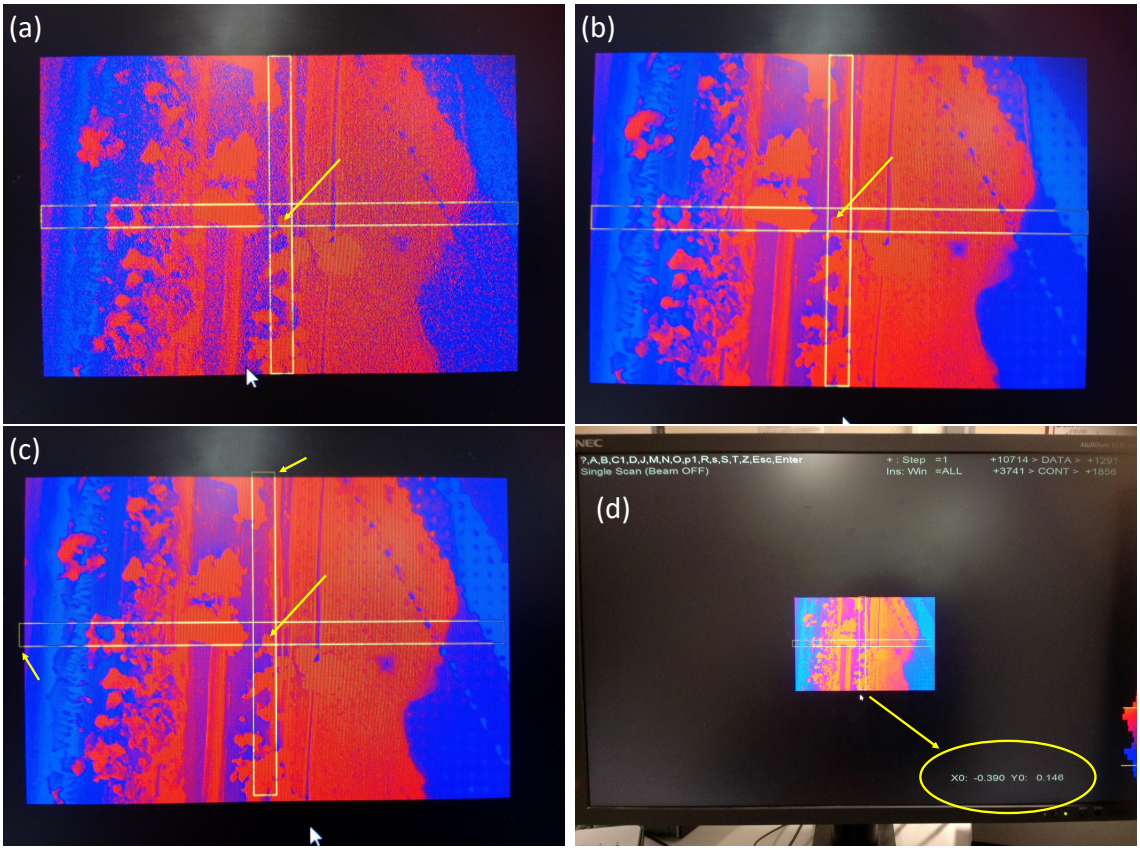

Figure 4.5: **Current misalignment correction procedure.** Images of the monitor of the EBL computer in each step: (a) shows the alignment pattern centered to the reference particle at the smallest current (e.g. 13 pA), (b) shows the same thing at the next current (e.g. 800 pA or 6400 pA) to know the misalignment with respect to the smallest current, (c) shows after centering the alignment pattern to the reference particle, and (d) shows where the offset values are shown in the monitor

is well written. The idea is to use two alignment marks far away from each other (10 mm distance for example), instead of using a local portion of a edge of a pattern. To do this, go to the "Stage" drop down menu and select "XT Align Feature". Draw a line by, first, clicking over one corner of an alignment mark, then move the stage using the stage position tab (relative) to the second alignment mark and make the second click over the equivalent point. This global alignment can also be used in the first EBL step by using the whole longest edge of the sample, this can be specially useful if then you want to dice the sample by the crystallographic directions.

4.3 Nanowires with top contact and square nanopillars

In this section I will explain the process of fabricating pillars using a new non-standard method. The original idea was to make a process which involved only tools that were always available and that were not subject to constant failures. The tools involved in the process are: sputtering system, ion mill, spinner and sonicator (ultrasonic bath) which are in Krivorotov's lab. SEM, XRD (optional), and e-beam evaporator from IMRI. Oxygen plasma cleaner from BiON and Filmetric (optional) from INRF at UCI. The reduction in the number of tools result in a reduction of the time of fabrication.

4.3.1 Multilayer deposition

The first step in the fabrication of nanopillars is the deposition of the multilayer. The typical multilayer stack consists of four parts: a bottom lead layer, a spin-valve, a top layer, and a cap layer. For example, the multilayer for the superconductor/ spin valve nanopillar is Nb(d_S)/Co(d_{F1})/Cu(6 nm)/Co(5 nm)/Cu(10 nm)/Au(30 nm), where d_S ranging from 25 nm to 45 nm, and d_{F1} from 0.6 nm to 5 nm. The cap layer is to prevent further oxidation of

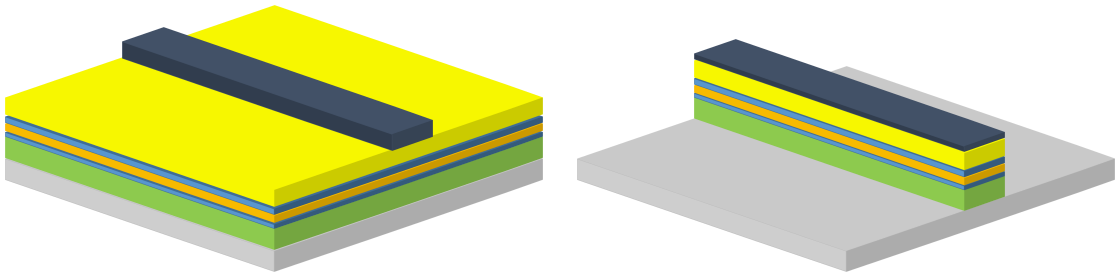

Figure 4.6: **Definition of bottom wires.** Left panel shows the multilayer structure with the e-beam MAN resist pattern on top of the multilayer. The MAN resist is used as hard mask for the etching process. Right panel shows the sample after etching, the nanowires are already defined

the multilayer bulk. In general, a cap layer of 5 nm thickness should be enough, however, for this method Au cap layer must be very thick to ensure there is enough Au after the etching steps. The multilayers are deposited via magnetron sputtering system on a Si/SiO_2(100 nm) substrate wafer. Because superconductivity is very sensitive to impurities, it is necessary to condition the chamber with the same elements of the multilayers before each deposition as described in Sec. 4.2.3 under ***conditioning system*** . In addition, oxidation between the superconducting layer and the spin-valve is an important issue. To prevent that, continuous deposition is chosen, see Sec. 4.2.3 under ***continuous deposition***. Usually a quarter of 4-inch wafer is used to make more than one chip with the same multilayer stack. If that is the case, dice off a chip following Sec. 4.2.2.

4.3.2 Definition of wires

Following the multilayer deposition is the definition of the bottom lead wire. The procedure consists of writing a hard masks on the chip as is illustrated in the Fig. 4.6(left). Then, via the ion mill, etch all material not protected by the hard mask, Fig. 4.6(right). Two types of hard mask can be used for the fabrication of nanopillars: MAN negative resist and evaporated hard mask. In order to simplify this section, I will explain the fabrication using

MAN resist and then in Sec 4.3.7, I will comment the differences in the fabrication using evaporated hard mask.

1. Spin coat MAN negative resist following Sec.4.2.6.

2. Write big alignments and the wires using EBL. The global map of patterns is shown in Fig. 4.7. The pattern of each device includes two sets of alignment marks which are made along with the wire. This is possible because the total thickness of the multilayer is thick enough to be used as alignment marks. An important reason why write the alignment marks along with the wire is to avoid to perform an EBL+deposition process only to write the alignment marks and it help to reduce of misalignment between the wire with the leads. The EBL parameters for the big alignment marks is: dosage of 250 μC/cm^2 and a beam current of 3200 pA, it can be also used the same parameter used for the big leads, see Table 4.3. The pattern for the big alignment is shown in Fig. 4.8. It is not necessary to write a big alignment mark under each column, but it is recommended in case you want to dice the chip to continue the fabrication for each piece independently. The pattern used for the bottom wire is shown in the Fig.4.9. The width of the nanowire can vary and is dependent on the final size of the pillar as will be explained in Sec.4.3.5. The pattern of the bottom lead wire has three layers as shown Fig.4.9: yellow for the nanowire and the small alignment marks (square-shape), green for the medium lead and medium alignment marks (L-shape), and blue for the big lead. Each of them has their own EBL parameters, see Table 4.3.

3. Develop MAN resist following the instruction in Sec. 4.2.6. Optionally, you can dice the substrate before developing to have clean pieces for the next step. Remember to avoid shaking the beaker during development, instead just move the beaker gently. After the development is completed, use optical microscopy to check if the writing process was successful. If the pattern does not look good (clearly overdose, wires are

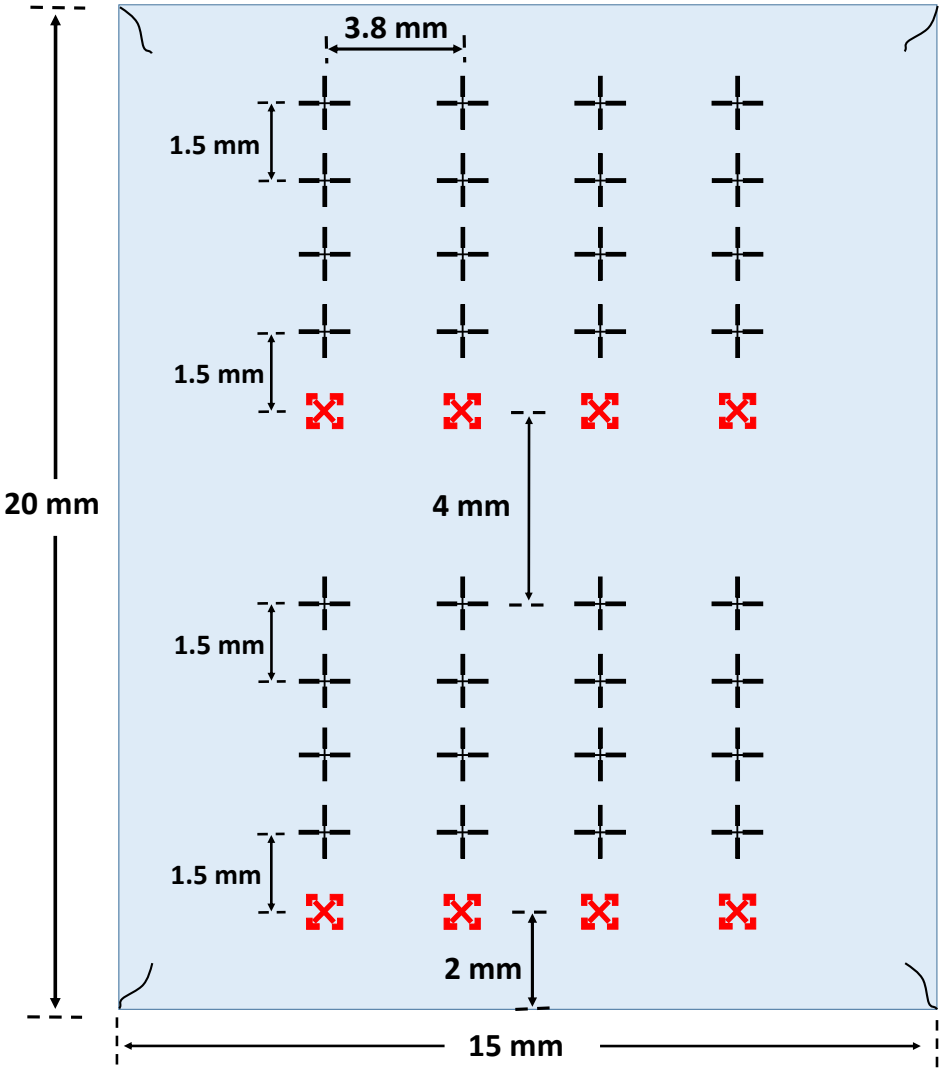

Figure 4.7: **Global map of patterns.** The red square with a X in the center are the big alignment marks. The black cross are the devices (bottom leads, top leads and local alignment marks). There are two horizontal lines of big alignment marks, this is to have the option to divide the sample in two pieces (top and bottom) and continue the fabrication for each piece independently. Two big alignment marks are necessary for piece, however, if you want to subdivide the piece in columns, it good to have an alignment mark for each of those column. That is why in this example each column has their own big alignment marks. Local alignment marks are not shown in this schematic.

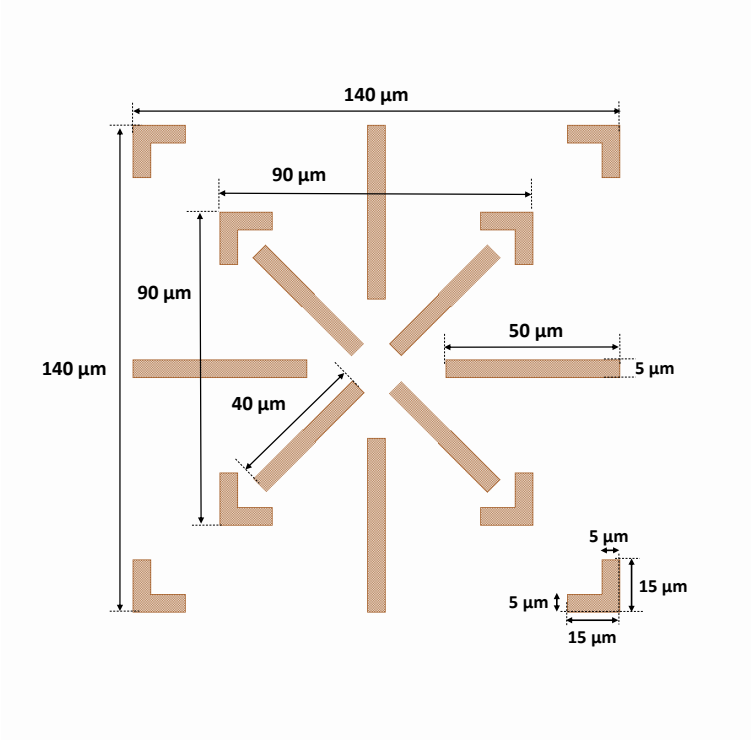

Figure 4.8: **Big alignment mark.** This pattern is completely symmetric. Some dimensions are shown and the rest are evidently known by symmetry.

Parameters	Wire	Medium Lead	Big Lead
Magnification	2100	500	80
Center-to-center Distance	1.04 nm	8.73 nm	27.28 nm
Line Spacing	1.04 nm	8.73 nm	27.28 nm
Spot Size	-6	0	3
Measured Beam Current	13 pA	800 pA	6400 pA
Area Dose	X μ C/cm^2	270 $\mu C/cm^2$	270 $\mu C/cm^2$

Table 4.3: EBL parameters. The dose of the wire X depends on the width of the wire. 250 μ C/cm^2 for width wider than 300 nm. 300 μ C/cm^2 for 150 nm width

disconnect, or they are wavy), it is recommended to repeat the writing process by first removing the MAN resist using acetone and IPA as described in Sec.4.2.1

4. Etch the chip using the ion mill until you get into the SiO_2 substrate. The ion milling parameters chosen to etch are critical. During the etching process usually there is re-deposition of the material etched on the side of the structure. The idea is to select a procedure such that it leaves a clean side-wall to avoid electrical shorting between the top and the bottom wires, this is even more critical in the fabrication of MTJ. To avoid side-wall shorting, a typical trick is to start with near-normal etch ($\sim$80 degrees), tilt to $\sim$45 degrees near the Cu spacer region (MgO for MTJ's) until you get to the end point, then tilt it to near-grazing ($\sim$10 degrees) for side-wall clean. Depending on how thick the stack is, and how much room you have to over-etch, you can switch between 80 degrees and 45 degrees a few times to optimize sidewall angle vs sidewall shorting. For example, for the superconductor/spin-valve multilayer, I do the following sequence of etching steps twice: 80 degrees for 2 min + 45 degrees for 1 min + 10 degrees for 20 seconds. The rest of the ion-milling parameters are given in Table 4.1. It is highly recommended to test the etch process on a piece of substrate with the same multilayer stack before doing on the real devices. The multilayer should be completely etched, slightly over-etched is preferable.

5. (optional) Measure the thickness of the remaining SiO_2 film using Filmetrics F40. This can serve as a reference for the next steps. In addition, it can be useful to check if the etching process was successful (remaining SiO_2 thickness $<$ the original 100 nm SiO_2 thickness). However, if the Filmetrics F40 is not available, you can skip this step. In my experience, the ion mill is very reliable and therefore if you have a very good calibration of the etching process, it is not really necessary to do this step.

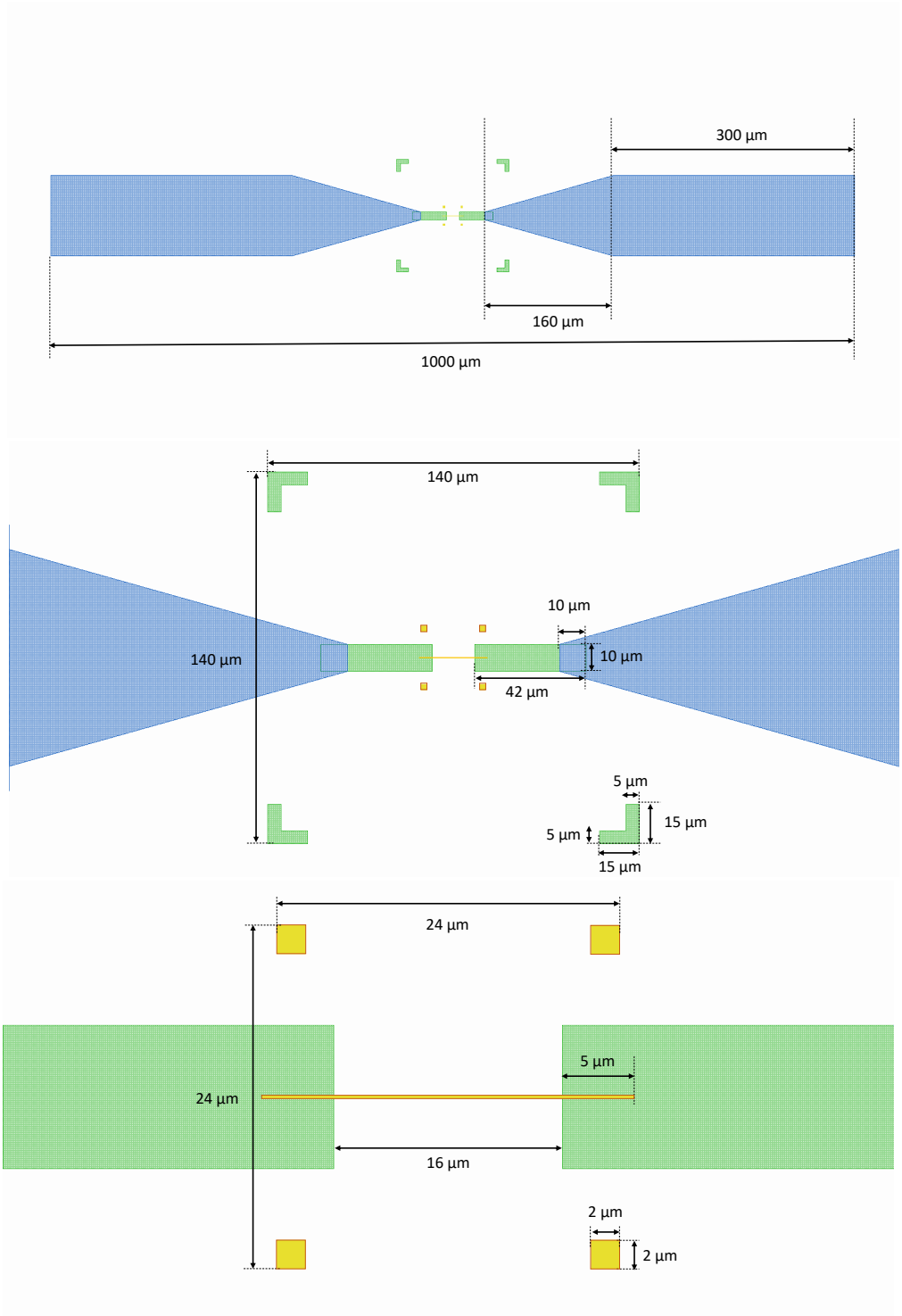

Figure 4.9: **Pattern for e-beam lithography of the bottom lead.** This consists in three parts: blue is the big part of the lead, green is the medium leads with the medium local alignment marks (L-shape), and yellow is the nanowire with the small local alignment marks (squares). In general, the smallest alignment marks have to be written along with the most important part (e.g. nanowire)

4.3.3 Dielectric Oxide Growth

The next step in the fabrication is to grow dielectric material on the side-walls of the bottom wire. This is for preventing any electrical shorting of the top lead through the side wall of the bottom wire. To do that, first, we cover completely the substrate with a dielectric oxide, for example evaporated SiO_2. The idea is to use a method which make the most uniform film possible. The best option is sputtering, but there is no system available for sputtering of SiO_2 at UCI [8]. The second option is PECVD, the problem is that this needs a pre-deposition of SiO_2 using e-beam evaporator to protect against the chemical reaction at high temperature 200 °C, and the tool is very often down for maintenance, in fact, during the time of designing this fabrication process, the tool was not available. For those reasons, evaporated SiO_2 is the best option, in addition, the evaporation is done in a system where the stage can rotate (spin) and it can have different angle of deposition. I use 45 degrees to increase the chances of depositing SiO_2 on the side-walls. The result is a film of SiO_2 with a bump on top of the wire. The thickness of the SiO_2 on top of the wire and the thickness of SiO_2 deposited everywhere else is the same. This is illustrate in Fig.4.10(right). The step by step procedure is:

1. E-beam evaporate 150 nm SiO_2 at 45 degrees from the normal with a spin speed of 20 rpm. It is recommended to include a piece of SiO_2 substrate, a piece of Si substrate and a piece of Pt film on the same sample holder to evaporate the same amount of SiO_2 as for the chip in fabrication. The extra pieces should be half covered as described in Sec.4.2.5. Then, the etch time and the thickness of the evaporated SiO_2(150 nm) film can be measured following Sec.4.2.5. The tool used to evaporate is the Angstrom Engineering EvoVac Glovebox Evaporator from IMRI. The deposition is consistent which is a great advantage over PECVD. I found the film grown does not vary more than 5 nm in 150 nm which is around 3%. This good reproducibility makes it possible to avoid the tedious process of recalculating the etch time if done already.

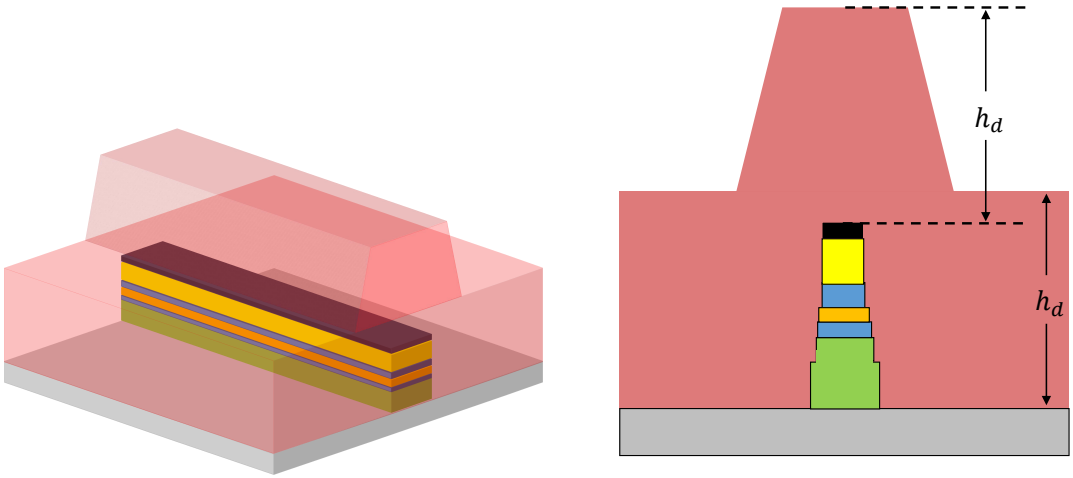

Figure 4.10: **Dielectric Oxide Growth.** The schematic shows how the wire is cover completely by the SiO_2 film creating a bump on top of the wire. The thickness of SiO_2 on top of the wire is the same as the thickness on the rest of the substrate. This is represented in the right panel

2. (optional) Measure the thickness of the SiO_2 film using Filmetrics F40. The total thickness of SiO_2 is equivalent to the sum of the remaining SiO_2 after definition of wire step and the evaporated SiO_2. If you already know the thickness of SiO_2 prior to the deposition you can figure out how much SiO_2 was deposited. Although, it is more precise to measure the SiO_2 deposited on Si substrate than using the chip in fabrication because the chip has an extra interface between the remaining SiO_2 from the previous step (large roughness) and the new SiO_2 film. That interface creates a distortion on the reflectivity signal which reduces accuracy of measured film thickness. Something similar happens if you use the SiO_2 piece, but the interface is not as bad as for the chip in fabrication. The main idea of the SiO_2 piece is to use it for measuring the etch time using Filmetric F40 and the Pt film similarly but using XRR.

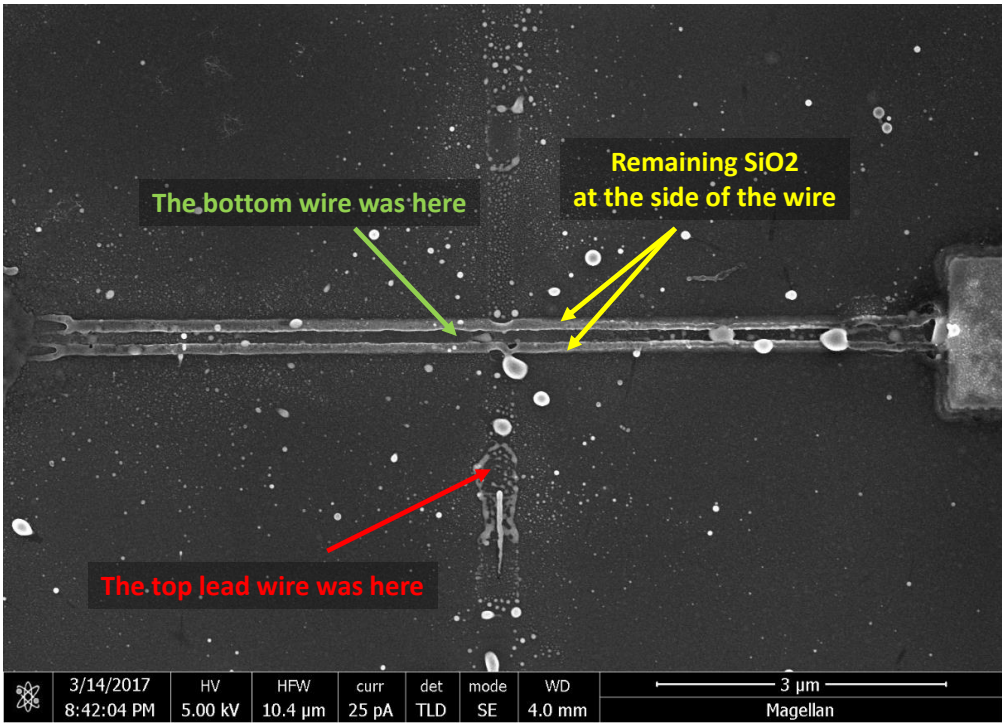

Figure 4.11: **Demonstration of the presence of SiO2 at the side of the wire.** SEM image of a sample destroyed by electric discharge, the two horizontal white line at the center is possible to see the remaining dielectric oxide growth at the side-walls of the wire

4.3.4 Open bottom wires

Now if an oblique etching removes all the SiO_2 from the top of the wire, it will also remove it from the area far from the wire. However, around the wire there will remain some SiO_2 due to the shadow effect during the etching at oblique angle (45 degrees). This is the heart of my idea: adding (isotropic deposition) + removing (anisotropic etching) results in something different than the original, see Fig.4.11. The procedure is:

1. Etch the chip using ion milling at 45 degrees for 11.5 min (or the etching time you measure for the deposited SiO_2) with duty-cycle 30-30 s (the rest of the parameters are the same as for wire definition). To increase the chances of success, it is recommended to measure the etch time as described in Sec.4.2.5 with either the SiO_2 substrate piece or with the Pt film piece placed alongside the main chip in the e-beam evaporator.

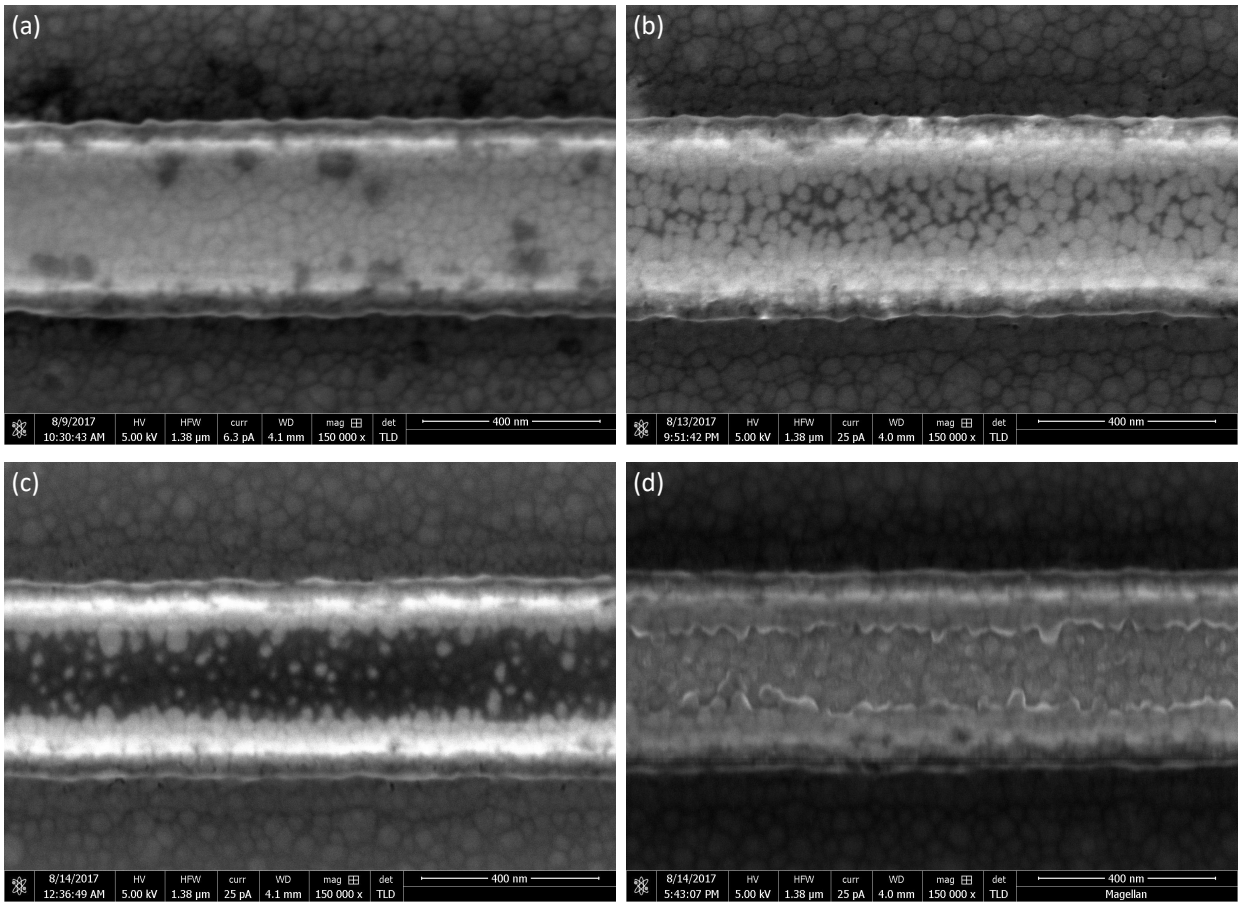

Figure 4.12: **SEM images** of the same wire after etching SiO_2. (a) after etching 10 min, (b) after etching extra 30 sec, total etch time = 10.5 min, (c) after etching a second extra 30 sec, total etch time = 11 min, and (d) after O_2 plasma etching for 3 min.

This will give a more accurate value of the etch time. If for any reason there is no way to measure the etch time, you can under-etch using previous data, suppose 1 min less and then etch until you get the top of the wire. There are two options to do this:

(a) Use the SEM to see the top of the wire for each step. Figure 4.12(a)-(c) shows a sequence of images until the top is visible (black areas is the MAN resist).

(b) Use the Filmetric F40. This was my original method to verify the removal of SiO_2 from the top of the wire. This is possible only if you have already used Filmetric F40 in the previous steps. You should measure a remaining thickness of SiO_2

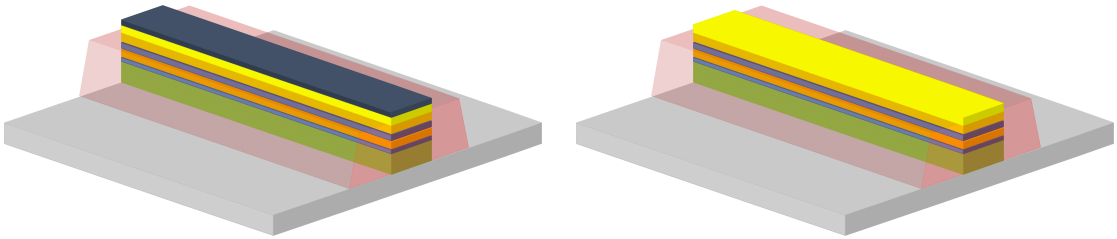

Figure 4.13: **Open bottom wires.** After an anisotropic etching process SiO_2 is removed from everywhere except the side of the wire (left). Right panel represent the sample after remove the MAN resist with O_2 plasma.

lower than the remaining SiO_2 after the definition of the wire. With that you are sure that you removed the SiO_2 on top of the wire.

Figure 4.13(left) shows schematically how the sample will look after ion mill etching. The wire would be protected at the side-walls by the remaining SiO_2 due to the adding+subtracting process. As I said before, the error is just a few nm which is less than 30 second. I found 11.5 min is a good time to etch 150 nm of SiO_2 evaporated at 45 degrees.

2. Oxygen plasma clean the chip for 3 min at high power using Harrick Plasma Cleaner. This step is necessary because there is still MAN negative resist on top of the wire. O_2 plasma in general can damage the sample by oxidizing the surface. However, the top part of the wire is Au which does not oxidize and side-walls are protected by SiO_2. So, a short O_2 plasma cleaning step is okay for the sample. Figure 4.12(d) shows how the wire looks after removing the MAN negative resist.

4.3.5 Deposition of the top lead wires

Once the top part of the wire is exposed and the side-walls are protected by SiO_2, it is ready for depositing the top lead. If your plan is only to create a top contact, you can

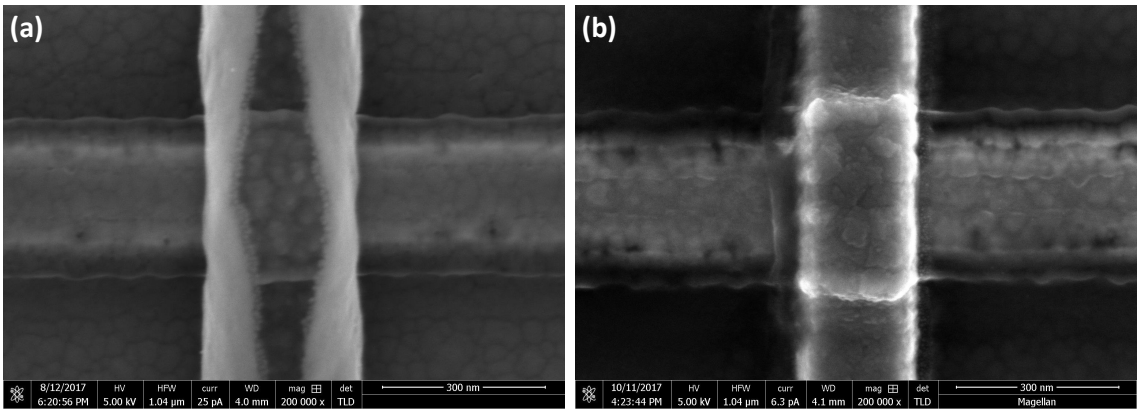

Figure 4.14: **Comparison between sputter and evaporated top lead.** Left panel shows the sputter top vertical lead, this lead is not very-well define. There is a huge side-wall and the center of the top lead looks thinner than the evaporated. This may be due to a shadow effect during deposition. The e-beam resist probably block the access to the material inside of the cavity. Instead, the right panel has an e-beam evaporated well-defined top wire which looks much thicker than the sputtered one. That is why the evaporated top lead is desirable as hard mask for the last step (definition of pillars).

sputter deposit the top lead. But if the plan is to create the pillars, e-beam evaporation is necessary. The advantage of sputtering is that the vacuum is much lower than the e-beam evaporator, which takes a few hours to just get a pressure of the order of 10^{-7} Torr. In addition, inside of the sputter chamber it is possible to do in situ cleaning with Ar plasma. The evaporator does not have this function. In general, sputtering is much easier to make good top contacts than with the e-beam evaporator. However, the shape of the top lead deposited by sputtering is more irregular than the one deposited by e-beam evaporator. Figure 4.14 shows the comparison between these two methods, Fig. 4.14(a) shows some "tongues" at the side of the top lead. This is because the metal is also deposited at the wall of the e-beam resist. After lift-off they fall into or outside the wire. That does not happen with e-beam evaporated lead Fig. 4.14(b). The step by step process is:

1. Spin coat MMA/PMMA bilayer resist by following Sec.4.2.6. This is the only option for sputter deposit top lead, for the e-beam evaporator you might also use a bilayer of PMMA. A single layer of PMMA is probably not enough for the thick top lead.

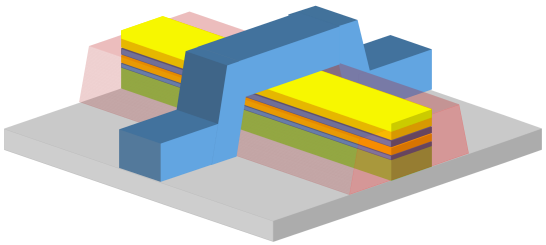

Figure 4.15: **Deposition of the top wire.** The top lead in the illustration is represented by blue color because this can be either normal lead or superconducting material lead.

2. Write top lead using EBL. There are two ways to align the top lead with respect to the bottom wire, using local alignment or just a global alignment as described in Sec. 4.2.6 under **"Sample Alignment"**. The pattern used for the top lead is shown in Fig. 4.16. Parameter of the EBL can be the same as for the bottom wire, see Table 4.3.

3. Develop the resist following the instruction in Sec. 4.2.6. Optionally, you can dice the substrate before developing to have clean pieces for different deposition conditions. Shake the beaker vigorously during the development and after the development is completed, use the optical microscopy to check if the writing process is successful. If not, repeat the EBL.

4. Deposit the top lead. For sputtering system Nb(5 nm)/Au(40 nm), for e-beam evaporator Cr(5 nm)/Au(40 nm)/Ti(40 nm). Nb, Ta, and Cr are good adhesion layers available in the sputtering system. Cr is the best option for the evaporator because Ti oxidizes very fast and makes poor top contact. To have better vacuum in the evaporator and avoid further oxidation of the adhesion layer, you can make a dummy evaporation (with the shutter close) of Ti or Cr to just decrease the pressure and therefore reduce the amount of O_2 gas in the chamber. The deposition of those metals in the wall of the chamber serves like getter. The 40 nm of Ti is used as hard mask for the definition

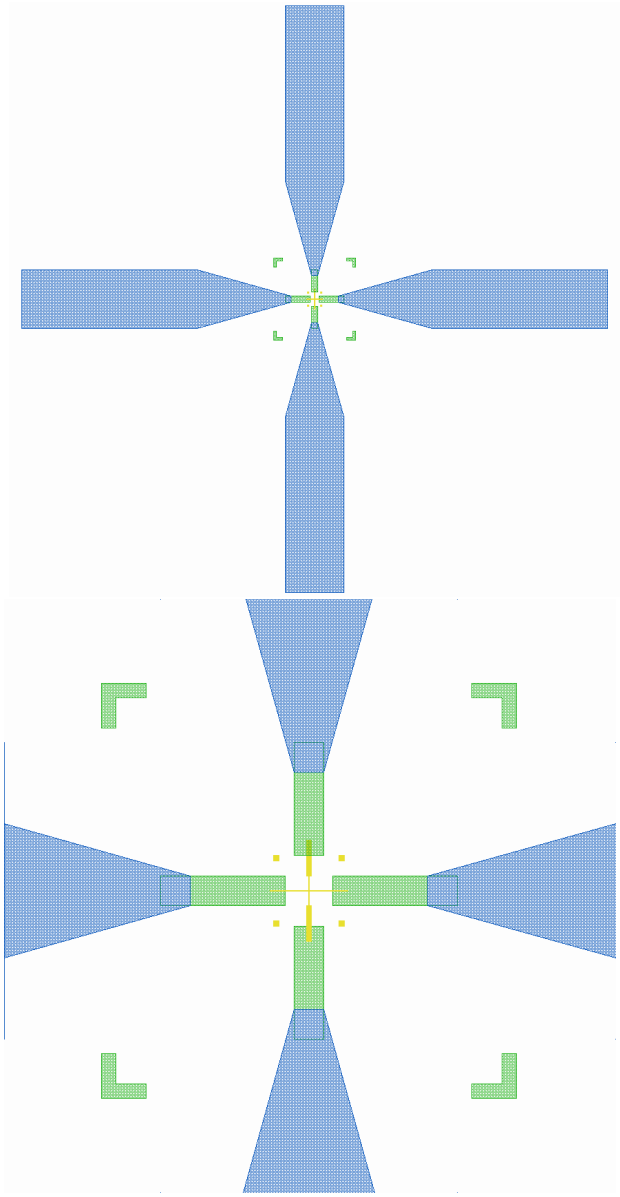

Figure 4.16: **Pattern for e-beam lithography of the top lead.** Two images of the dgs file program to make the top lead (vertical structure). The dimensions are the same as for the bottom lead layer. The only different is the top lead wire is wider in some part to reduce the resistance and the distance between the medium leads are longer than fro the bottom leads. However, the dimensions will depend on the application.

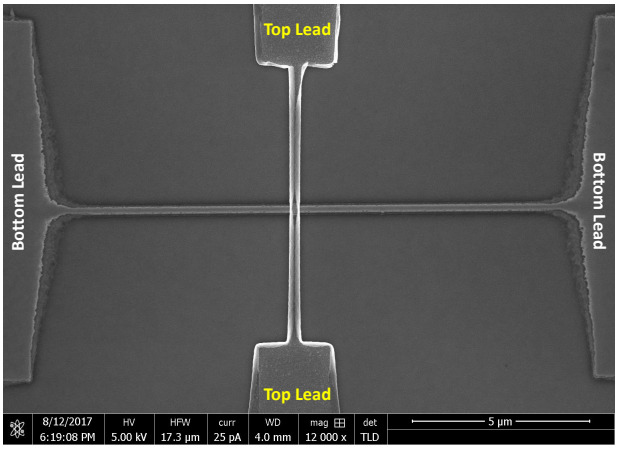

Figure 4.17: **SEM image of the structure after depositing the top lead** Vertical wire is the top lead wire and the horizontal wire is the bottom lead wire. The top lead of this sample was sputtered, that is why there is some strutures at the edges of the wire.

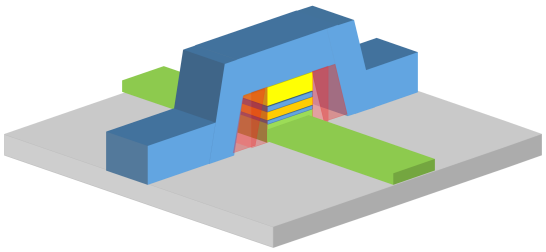

Figure 4.18: **Definition of the pillars.** The schematic shows how the nanopillar would look after the last etching process.

of the pillar (next step). Another option of hard mask is Al_2O_3 which has a very low etch rate. The structure looks like Fig. 4.17.

4.3.6 Definition of pillars

At this point of the fabrication, there is a wire with top contact. To have a complete definition of the pillar an extra etch step is needed to remove part of the wire not protected by the top lead. The end point is at the middle of the bottom lead layer. The top lead has to be evaporated to have a well-defined nanopillar. Figure 4.18 represent the final step of the fabrication.

4.3.7 Notes Regarding the Fabrication

First of all, I want to emphasize that this method of fabrication of nanopillars or nanowires with top contact is new and therefore subject to improvement. The most important is related with the top contact and the choice of the hard mask. In the last section, I described the procedure using MAN negative resist.

The advantages are:

1. One step to create the hard mask (a EBL step).
2. No extra calibration needed to ensure the mask is removed, because the thickness of the remaining MAN resist does not matter, it will be removed by O_2 plasma which is very selective (it does not etch Au or SiO_2).

The disadvantage are:

1. It is not good for small devices because negative resist is very hard to remove, even with O_2 plasma, basically because it is trapped by SiO_2. Most likely it needs further refinement to be successful with small devices on the order of 100 nm or smaller
2. The removal of the MAN resist is not a repeatable process. Figure 4.19 shows two images of same stage of fabrication of two different samples. Both samples were fabricated at the same time, the only difference was the removal of MAN resist by O_2 plasma. Clearly, this is not good for the consistency between devices, because sometimes the resistance fluctuates significantly or simply has no contact. An extra step of O_2 plasma cleaning is not guaranteed to solve the problem of contact, instead it can cause damage in the devices by oxidizing them.

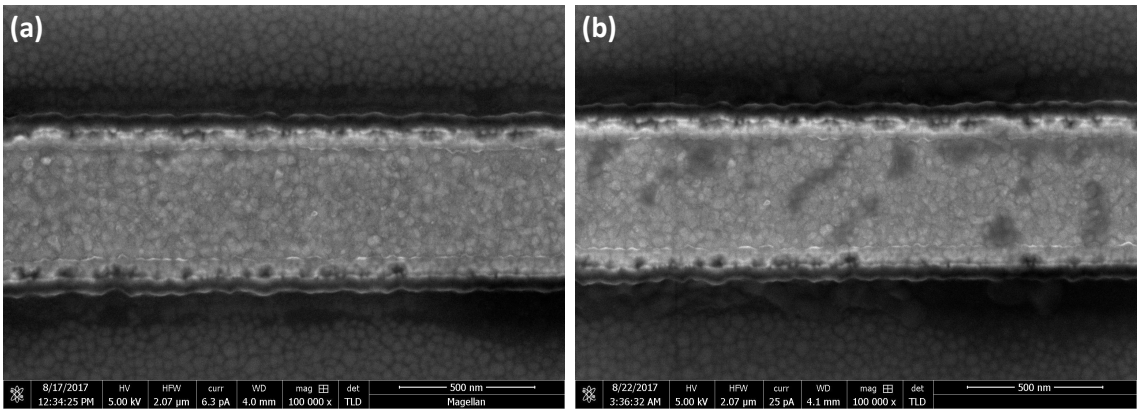

Figure 4.19: **Dirty surface using MAN resist.** In this SEM images is shown the MAN resist in not remove in the same way every time

One possible solution to continue using MAN negative resist is to find a good method to remove the resist without O_2 plasma. Piranha is an alternative that I have not explored yet. That chemical can etch MAN resist very easily, but it can not etch Au nor SiO_2. Because the top of the wire has Au and the side-wall has SiO_2 it can be a good option.

The solution of the top contact could be solved by evaporating a hard mask. Possible hard masks are Ti, Cr, Ti/Al_2O_3, Cr/Al_2O_3, or any material which can be evaporated and has low etching rate. I already made some devices using Ti hard mask. The procedure is basically the same than using MAN negative resist. The main differences between them are in the definition of the wires:

1. Spin coat e-beam resist (PMMA, 2 layers of PMMA, or MMA/PMMA depend on the thickness of the top lead) instead of MAN negative resist following Sec.4.2.6.

2. Develop the e-beam resist following Sec.4.2.6.

3. Deposit the hard mask using e-beam evaporator, for example, Cr/Al_2O_3. Previously, it is necessary to calculate the etching time for this hard mask. The time has to be the same as the time to etch the wire to ensure the hard mask is completely removed. This is critical if the hard mask does not have ohmic contact with the multilayer, because

even if you try to get good contact with the top lead, the interface between the hard mask and the multilayer will produce an extra resistance to the contact or simply will not be in ohmic contact at all. In my experience, Ti is a good hard mask because the etching rate is low, but oxides very easily and therefore introduces the problem described before. So I had to remove it in the etching step. On the other hand, Cr is not a good hard mask (its etching rate is similar to any other metal $\sim$ 10 nm/min), but it is a good adhesion layer and does not oxide as fast as Ti. It would be good to test Cr to make better contact.

4. Lift-off the hard mask. Now it is ready for etching.

The rest of the steps are the same except for the O_2 plasma cleaning step which is to remove MAN resist, so skip it.

4.4 Testing Results

The following summarizes some of the measurement results taken with a device fabricated in the discussed fabrication approach. In these devices was possible to measure current perpendicular-to-plane magnetoresistance. Figure 4.20 shows the resistance as a function of the magnetic field along the direction of the bottom wire. It is possible to measure the typical GMR curve for this kind of devices at normal state and the superconducting state. This result demonstrates the successful fabrication process. However, this is not very strong effect and therefore some refinements in the process are needed.

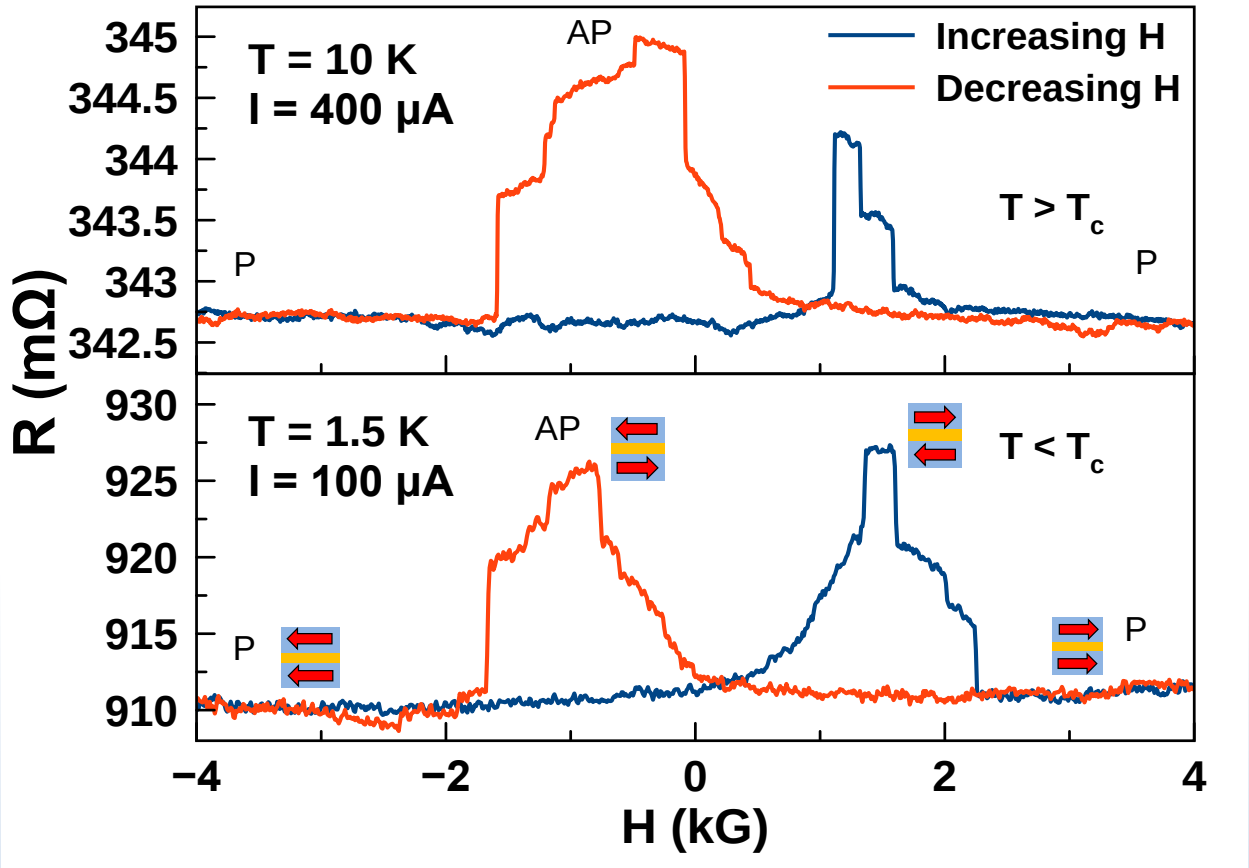

Figure 4.20: **Current perpendicular-to-plane measurement.** Resistance versus field along the bottom wire direction. Top plot shows the data when the system is at normal state and the bottom plot when is at superconducting state

Bibliography

[8] Muhammad Rizwan Amirzada et al. “Surface roughness analysis of SiO2 for PECVD, PVD and IBD on different substrates”. In: *Applied Nanoscience* 6.2 (2016), pp. 215–222. ISSN: 2190-5517. URL: https://doi.org/10.1007/s13204-015-0432-8.

Chapter 5

Angular dependence of superconductivity in superconductor / spin valve heterostructures

The contents of this chapter are adapted from work originally published as *Phys. Rev. B 89, 184502 (2014)*. This is a collaborative work between an experimental group at UC Irvine leading by professor Ilya Krivorotov and a theoretical group at the University of Minnesota, Minneapolis leading by professor Oriol Valls.

5.1 Introduction

Competition between superconducting (S) and ferromagnetic (F) ordering in S/F heterostructures can lead to unusual types of superconductivity emerging from the proximity effect at the S/F interfaces [9–17]. Penetration of spin-singlet Cooper pairs from the S into the F material can result, when more than one magnetic orientation is present, in mixing of the

spin-triplet and spin-singlet states by the exchange field and generation of a spin-triplet component of the condensate [14, 15, 18–23]. The amplitude of this proximity-induced triplet state sensitively depends on the state of magnetization of the F material. In particular, the triplet components with nonzero projection of the spin angular momentum of the Cooper pair ($S_z = \pm 1$) can only occur when there are magnetization noncollinearities. These components of the condensate are immune to pair breaking by the exchange field and, unlike the singlet and the $S_z = 0$ triplet components, they can penetrate deep into the F material [15, 23, 24]. This long-range triplet condensate can be manipulated via changing the relative orientation of the magnetizations, which creates opportunities for the development of a new class of superconducting spintronic devices. Recent progress in this direction is demonstration of Josephson junctions with noncollinear magnetic barriers, in which the supercurrent is carried by the long-range triplet component of the condensate [25–27].

Thin-film multilayers of S and F materials are a convenient experimental platform for studies of the proximity-induced triplet condensate [28–36]. The advantages of the F/S multilayers include (i) well-established methods of the multilayer deposition, (ii) easy and controllable manipulation of the magnetic state of the F layers via application of external magnetic field, and (iii) convenience of theoretical description of the condensate owing to the translational symmetry in the multilayer plane. Here we present studies of the dependence of T_c in CoO/Co/Cu/Co/Nb multilayers on the in-plane angle α between the magnetic moments of the Co layers. We compare our experimental results to numerical solutions of the Bogoliubov–de Gennes equations and find that excellent quantitative agreement with the experiment can be achieved when scattering at the multilayer interfaces is taken into account. This solution also reveals that T_c suppression observed for the orthogonal state of the Co magnetic moments originates from enhanced penetration of the long-range triplet condensate into the Co/Cu/Co spin valve in this maximally non-collinear magnetic state. Comparison between the theoretical and experimental $T_c(\alpha)$ allows us to quantify the induced triplet pair amplitude in the spin valve, which reaches values greater than 1% of the singlet pair

amplitude in the Nb layer for the maximally noncollinear ($\alpha = \pi/2$) configuration of the spin valve.

5.2 Sample Preparation and Characterization

The CoO(2 nm)/ Co(d_p)/ Cu(d_n)/ Co(d_f)/ Nb(17 nm)/ (substrate) multilayers, schematically shown in Fig. 5.1(a), were prepared by magnetron sputtering in a vacuum system with a base pressure of 8.0×10^{-9} Torr. The deposition was performed onto thermally oxidized Si substrates at room temperature under an Ar pressure of 2 mTorr. The 2 nm thick CoO layer was formed by oxidation of the top part of the Co layer in air for at least 24 hours. The native CoO film is antiferromagnetic at cryogenic temperatures and its purpose is to pin the direction of the top Co layer via the exchange bias phenomenon [37]. Three series of multilayers, each series with varying thickness of one of the layers (pinned d_p, free d_f, and nonmagnetic d_n) were deposited in continuous runs with minimal breaks between the samples within the series. This ensured that samples within each of the series were prepared in similar residual gas environments. The three multilayer series reported in this work were designed to elucidate the dependence of the triplet condensate pair amplitude on the spin valve parameters. The description of the series geometries is as follows:

Series 1: CoO(2 nm)/ Co(2.5 nm)/ Cu(6 nm)/ Co(d_f)/ Nb(17 nm) with d_f ranging from 0.5 nm to 1.0 nm

Series 2: CoO(2 nm)/ Co(2.5 nm)/ Cu(d_n)/ Co(0.6 nm)/ Nb(17 nm) with d_n ranging from 4 nm to 6.8 nm

Series 3: CoO(2 nm)/ Co(d_p)/ Cu(6 nm)/ Co(0.6 nm)/ Nb(17 nm) with d_p ranging from 1.5 nm to 5.5 nm.

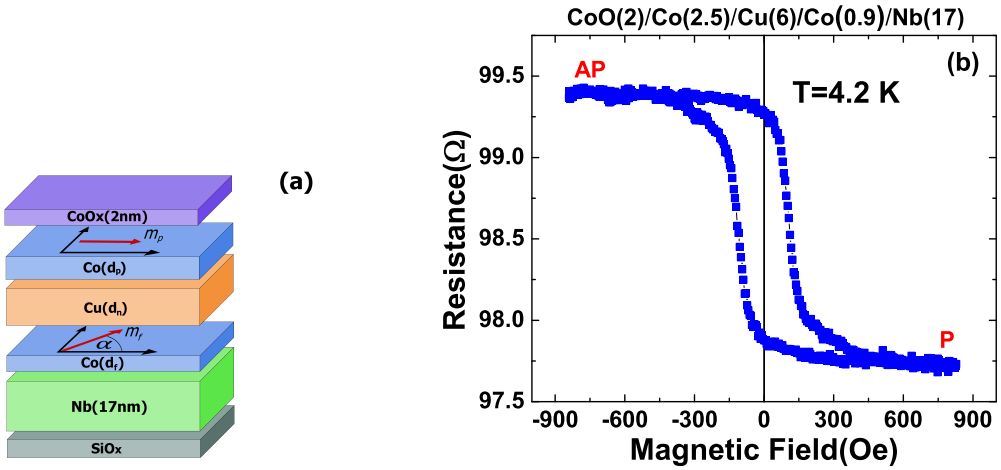

Figure 5.1: **Schematic and resistance versus magnetic field.** (a) Schematic of the CoO(2 nm)/ Co(d_p)/ Cu(d_n)/ Co(d_f)/ Nb(17 nm) multilayer, where α is the in-plane angle between the magnetic moments of the Co layers. (b) Resistance versus the in-plane magnetic field applied parallel to the pinned layer magnetization at $T = 4.2$ K (above the superconducting transition temperature).

The multilayers were patterned into 200 μm-wide Hall bars using photolithography and liftoff. Four-point resistance measurements of the samples were performed in a continuous flow ^{4}He cryostat. The magnetization direction of the top Co layer was pinned in the plane of the sample by a strong ($\sim$ 1 T) [37] exchange bias field from the antiferromagnetic CoO layer. The exchange bias field direction was set by a 1500 Oe in-plane magnetic field applied to the sample during cooling from the room temperature. As we demonstrate below, the magnetization of the free Co layer can be easily rotated in the plane of the sample by a relatively small ($\sim$ 500 Oe) magnetic field. The role of the nonmagnetic Cu spacer layer is to decouple the magnetic moments of the Co layers, and it is chosen to be thick enough ($d_n >$4 nm) so that both the direct and the RKKY [38] exchange interactions between the Co layer are negligibly small. In all magnetoresistance measurements reported here, care is taken to align the applied magnetic field with the plane of the sample so that vortex flow resistance is negligible [39].

Figure 5.1(b) shows the resistance of a CoO(2 nm)/ Co(2.5 nm)/ Cu(6 nm)/ Co(0.9 nm)/ Nb(17 nm) sample as a function of the magnetic field applied along the exchange bias

direction measured at $T = 4.2$ K (above the superconducting transition temperature T_c). At $T = 4.2$ K, all samples show the conventional giant magnetoresistance (GMR) effect originating from the Co/Cu/Co spin valve. Given that there is significant current shunting through the Nb layer, the magnitude of the GMR ($\sim$2%) is large, demonstrating good quality of both Co/Cu interfaces [38]. The GMR curve also demonstrates that external in-plane magnetic field of ≥ 500 Oe fully saturates the free layer magnetization along the applied field direction. The lack of an offset in the GMR hysteresis loop from the origin demonstrates that the interlayer exchange coupling between the Co layers is negligible.

5.3 Angular Dependence of T_c

We next make measurements of the multilayer superconducting transition temperature T_c as a function of the angle α between magnetic moments of the pinned and free layers. We define T_c as the temperature at which the sample resistance becomes equal to half of its normal state value. For these measurements, we use an 800 Oe in-plane magnetic field to set the direction of magnetization of the free layer. As discussed in the previous section, this field completely saturates the magnetization of the free layer in the direction of the field. Furthermore, this field is much smaller than the exchange bias field acting on the pinned layer and thus we assume that the pinned layer magnetization remains in the direction of the cooling field for all our measurements. Figure 5.2 shows resistance versus temperature measured in the parallel (P, $\alpha = 0$), antiparallel (AP, $\alpha = \pi$), and perpendicular (90°, $\alpha = \pi/2$) configurations of the two Co layers for the samples with 0.5 nm and 1.0 nm thick Co free layers, and 2.5 nm thick Co pinned layer. In this measurement, the angle between the magnetic moments is pinned by the in-plane external field while the temperature is swept across the superconducting transition. To ensure that the sample remains in thermal equilibrium with the bath, the temperature for each measurement is swept at a sufficiently slow rate of 2 mK per minute. For both values of the free layer thickness, we find that the perpendicular configuration of

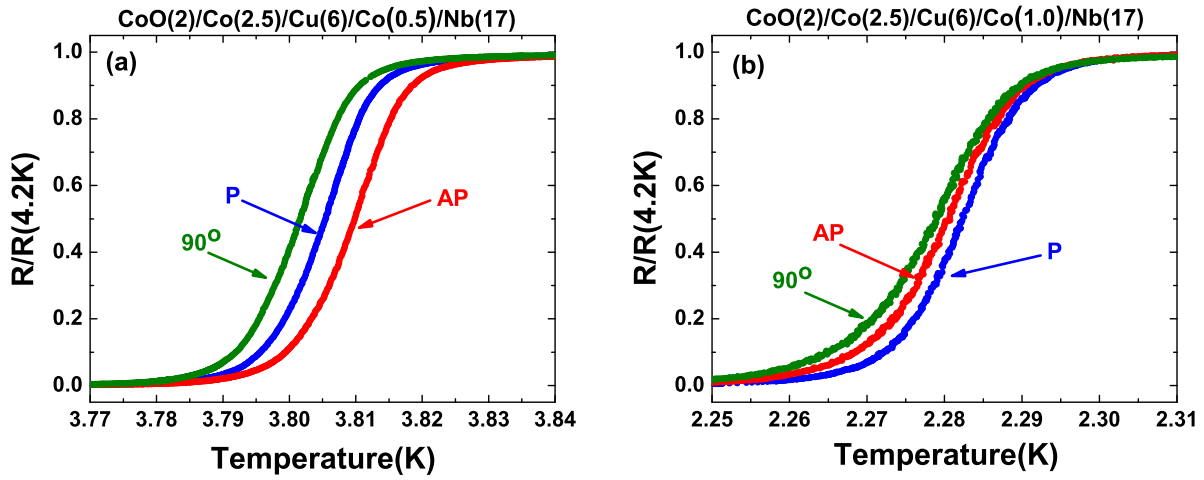

Figure 5.2: **Resistance versus temperature** for parallel (P, $\alpha = 0$), antiparallel (AP, $\alpha = \pi$), and perpendicular (90°, $\alpha = \frac{\pi}{2}$) orientations of magnetic moments of the Co layers for multilayer samples with (a) $d_f = 0.5$ nm and (b) $d_f = 1.0$ nm. The resistance is divided by its normal state value measured at $T = 4.2$ K.

the spin valve ($\alpha = \pi/2$) gives the lowest transition temperature T_c. We find this to be universally true for all samples studied in this work: $T_c(\pi/2) < T_c(0)$ and $T_c(\pi/2) < T_c(\pi)$. In contrast, the relation between T_c in the P and AP configurations depends on the thickness of the free layer. Figure 5.2 shows that $T_c(0) < T_c(\pi)$ for $d_f = 0.5$ nm, while $T_c(\pi) < T_c(0)$ for $d_f = 1.0$ nm. Similar trends in the angular and thickness dependence of T_c were recently observed in Pb/ Fe/ Cu/ Fe/ CoO multilayers [31].

To understand the angular dependence of T_c in greater detail, we fix the temperature in the middle of the superconducting transition and measure the sample resistance R as a function of in-plane angle α between the magnetic moments of the pinned and free layers. This measurement is made by applying an 800 Oe saturating magnetic field and rotating it through 360° in the plane of the sample. Figure 5.3 shows $R(\alpha)$ measured at $T = 2.92$ K (the middle of the superconducting transition) for a CoO(2 nm)/ Co(2.5 nm)/ Cu(6 nm)/ Co(0.6 nm)/ Nb(17 nm) sample. Because resistance is a steep function of temperature in the middle of the superconducting transition, we take great care to stabilize the temperature to within ±0.1 mK during these measurements in order to reduce the level of thermal noise in the $R(\alpha)$ data.

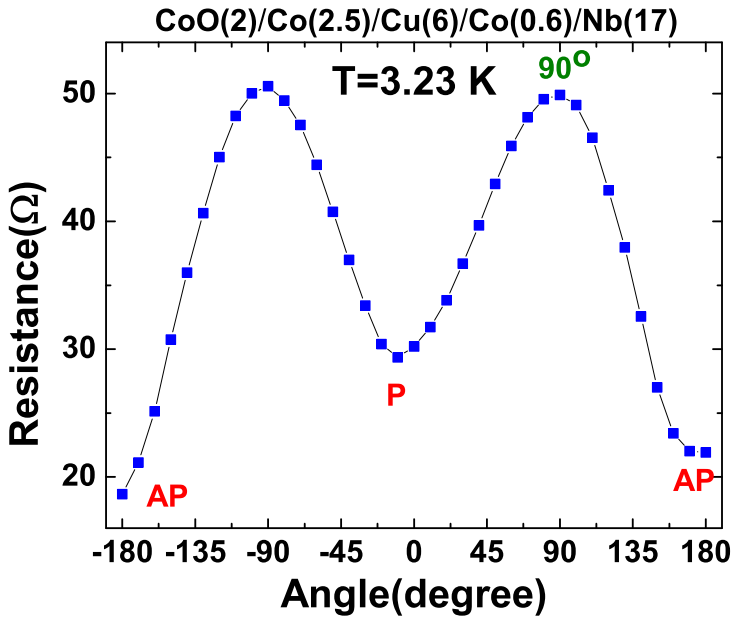

Figure 5.3: **Resistance versus angle.** Resistance of a CoO(2 nm)/ Co(2.5 nm)/ Cu(6 nm)/ Co(0.6 nm)/ Nb(17 nm) structure versus magnetic field angle, α , measured at $T = 2.92$ K in the middle of the superconducting transition, at a field of 800 Oe.

Measurements of $R(\alpha)$ are much faster than those of $R(T)$ because reliable $R(T)$ data require sweeping temperature at slow rates. Thus we employ the $R(\alpha)$ data in order to evaluate $T_c(\alpha)$ instead of direct measurements of $T_c(\alpha)$ at multiple values of α, such as those shown in Fig. 5.2. We therefore need a reliable method of extracting $T_c(\alpha)$ from the $R(\alpha)$ data. The simplest method for such extraction is to use the slope of the $R(T)$ curve at T_c for $\alpha = 0$ and to calculate $T_c(\alpha)$ as $T_c(\alpha) = T_c(0) - (dT/dR)\,[R(\alpha) - R(0)]$, where $R(\alpha)$ is the experimentally measured angular dependence of resistance at $T = T_c(0)$. This simple method assumes approximately linear variation of resistance with temperature near T_c and already gives qualitatively satisfactory results. However, the maximum uncertainty in the resulting $T_c(\alpha)$ can be as large as 5 mK. The purple dotted curve in Fig. (5.4) shows $T_c(\alpha)$ calculated by this method for a CoO(2 nm)/ Co(2.5 nm)/ Cu(6 nm)/ Co(0.6 nm)/ Nb(17 nm) multilayer.

In order to take into account deviations of $R(T)$ from a linear function and thereby improve the procedure for extracting $T_c(\alpha)$ from the $R(\alpha)$ data, we calculate $T_c(\alpha)$ based on the

experimentally measured $R(T,0)$ and $R(T^*,\alpha)$ curves, where $T^* \approx T_c(0)$ is the temperature at which the angular dependence of resistance is measured. In this method, we assume that the shape of the $R(T)$ curve is the same for all values of α, and that the curves at different α can be obtained by simply translating the experimentally measured $R(T,0)$ curve along the temperature axis by $\Delta T_c(\alpha) = T_c(\alpha) - T_c(0)$. With this assumption, $T_c(\alpha) = T_c(0) + \Delta T_c(\alpha)$ can be found by numerically solving the implicit equation $R(T^*,\alpha) = R(T^* - \Delta T_c(\alpha), 0)$ for $\Delta T_c(\alpha)$. The blue squares in Fig. (5.4) show $T_c(\alpha)$ evaluated by this method using the transition curve from the P ($\alpha = 0$) state. The red triangles and green dots represent the same method used with the other two measured curves. We find this method of evaluating $T_c(\alpha)$ to be quite reliable for our samples with an estimated error of ~ 1 mK.

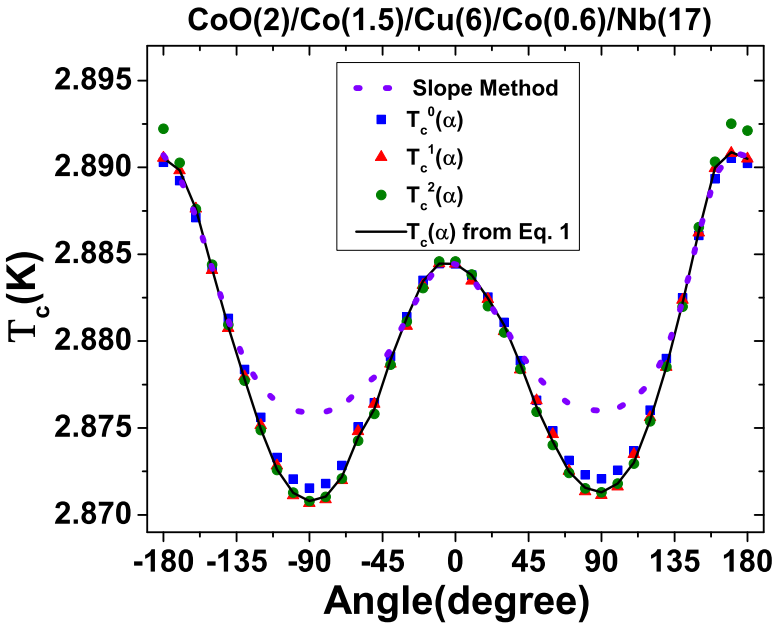

Figure 5.4: T_c **versus angle.** $T_c(\alpha)$ for a CoO(2 nm)/ Co(1.5 nm)/ Cu(6 nm)/ Co(0.6 nm)/ Nb(17 nm) multilayer calculated from the $R(\alpha)$ data by different methods described in the text.

An even more refined method of evaluating $T_c(\alpha)$ takes into account that the shape of the $R(T)$ curve (not only its position along the temperature axis) may depend on α. Here we first calculate $\Delta T_c(\alpha)$ based on the experimentally measured $R\,(T,\pi/2)$ and $R(T,\pi)$ curves using the method described above: we calculate $T_c(\alpha)$ by numerically solving the implicit

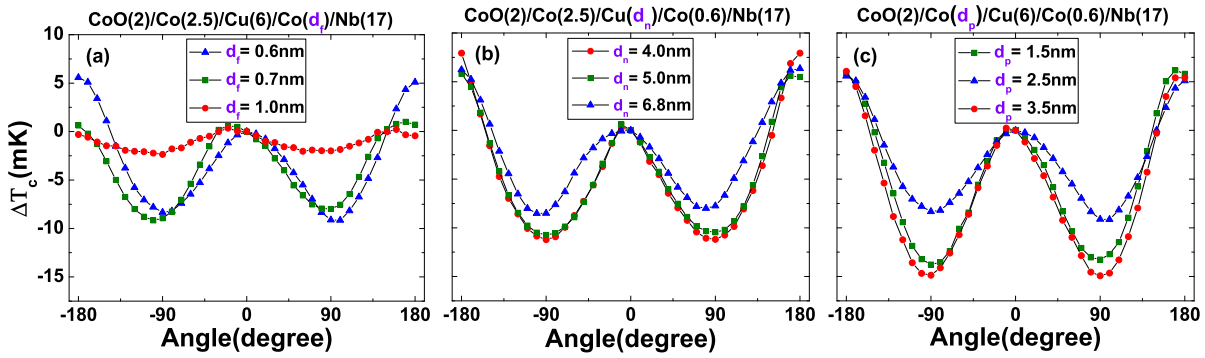

Figure 5.5: T_c **versus angle and thicknesses.** $T_c(\alpha)$ for representative samples from the three series of samples studied in this paper. (a) From the d_f series, (b) from the d_n series, (c) from the d_p series.

equations $R(T^*, \alpha) = R\left(T^* - \Delta T_c(\alpha), n\pi/2\right)$ for $\Delta T_c(\alpha)$, where $\Delta T_c(\alpha) = T_c(\alpha) - T_c\left(n\pi/2\right)$, $n = 1, 2$. These $T_c(\alpha)$ values calculated for $n = 1, 2$ are shown in Fig. (5.4) as green circles and red triangles, respectively. Figure (5.4) clearly illustrates that all three functions $T_c(\alpha)$ calculated by numerically solving the implicit equations written above for $n = 0, 1, 2$ are very similar to each other. The average of these three functions $T_c^n(\alpha)$, which we now explicitly label by the index $n = 0, 1, 2$, would give a reasonable result for $T_c(\alpha)$. However, a better estimate is given by the following equation:

$$T_c(\alpha) = \sum_{n=0}^{2} T_c^n(\alpha) w_n(\alpha) \tag{5.1}$$

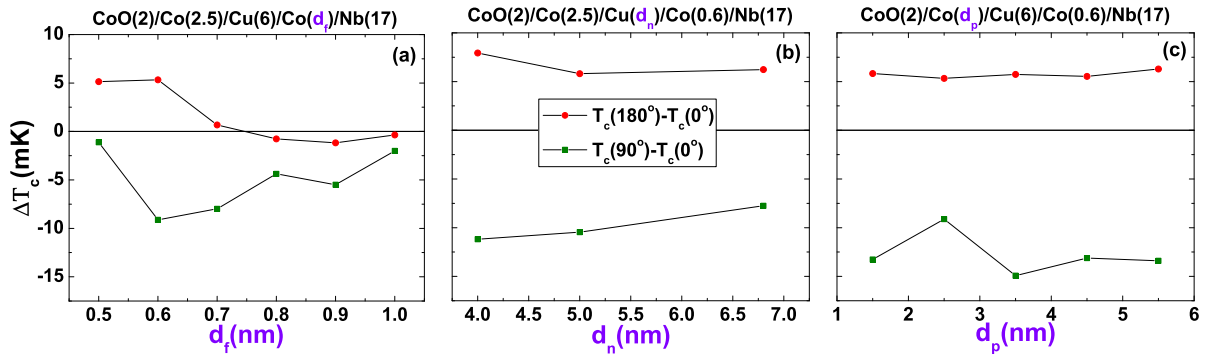

Figure 5.6: ΔT_c **versus thicknesses.** Dependence of $T_c(\pi) - T_c(0)$ (red circles) and $T_c(\frac{\pi}{2}) - T_c(0)$ (green squares) on the free Co layer thickness d_f (a), nonmagnetic spacer thickness d_n (b), and pinned layer thickness d_p (c).

where $w_n(\alpha)$ are extrapolation functions with maxima at $\alpha = \pm n\pi/2$. The extrapolation functions also satisfy the normalization condition $\sum_{n=0}^{2} w_n(\alpha) = 1$ on the interval of α from $-\pi$ to π. We make the following choice of the extrapolation functions: $w_0(\alpha) = \cos^2(\alpha)\Theta\left(\pi/2 - |\alpha|\right)$, $w_1(\alpha) = \sin^2(\alpha)$ and $w_2(\alpha) = \cos^2(\alpha)\Theta\left(|\alpha| - \pi/2\right)$, where $\Theta(x)$ is the Heaviside step function. The advantage of Eq. (5.1) over the simple average is that at $\alpha = 0, \pi/2, \pi$, the expression for $T_c(\alpha)$ reduces to the exact value of T_c directly measured at these angles in the $R(T)$ measurements. The black solid line in Fig. (5.4) shows $T_c(\alpha)$ evaluated by this method. We use this method for calculating $T_c(\alpha)$ from the experimental data throughout the rest of the paper.

Figure 5.5 shows a representative angular variation of T_c, $\Delta T_c(\alpha) = T_c(\alpha) - T_c(0)$, for the three series of samples employed in our study. We find that for all samples employed in our experiment, $T_c(\alpha)$ is a nonmonotonic function in the interval of α from $-\pi$ to π with a minimum near perpendicular orientation of the free and pinned layers ($\alpha = \pi/2$). As we demonstrate in the analysis section of this paper, this minimum in T_c arises from the enhanced long-range triplet pair amplitude in the maximally noncollinear configuration of the spin valve. We also note that our previous studies of the angular dependence of T_c in NiFe/Nb/NiFe trilayers [40] found monotonic dependence of T_c on α in the 0 to π range, which serves as indication of a much weaker triplet pair amplitude induced in the system with two ferromagnetic layer separated by a superconductor.

Figure 5.6 summarizes the dependence of $T_c(\alpha)$ on the thickness of the Co/Cu/Co spin valve layers. Figure 5.6(a) shows the difference of T_c in the P and AP states as a function of the free layer thickness d_f. The data demonstrate that $T_c(\pi) - T_c(0)$ oscillates and changes sign as a function of d_f, which is a consequence of interference of the pair wave function in the free layer. Figures 5.6(b) and 5.6(c) show the dependence of $T_c(\pi) - T_c(0)$ on the nonmagnetic spacer thickness d_n and the pinned layer thickness d_p. This dependence is weak, which implies that (i) the pair amplitude decays slowly in the Cu spacer layer and (ii)

the pair amplitude decays to nearly zero over the pinned layer thickness greater than 1.5 nm (the thinnest pinned layer employed in our studies). The behavior of T_c will be discussed in general later in this work.

Figure 5.6 also illustrates the thickness dependence of T_c in the maximally noncollinear geometry of $\alpha = \pi/2$. The green squares in Fig. 5.6 show the dependence of $T_c(\pi/2) - T_c(0)$ on the spin valve layer thicknesses. This figure clearly shows that $T_c(\pi/2)$ is always lower than $T_c(0)$ and $T_c(\pi)$. Figure 5.6(c) illustrates that $T_c(\pi/2)$ shows variation with the pinned layer thickness for d_p as large as 3.5 nm. This serves as evidence of the long-range (> 3.5 nm) penetration of the triplet component of the condensate into the pinned ferromagnetic layer.

5.4 Theoretical Methods

The theoretical method we adopted is thoroughly discussed in Refs. [17, 23, 41]; therefore, we only present here the essential parts that are necessary for our discussion. In particular, the theoretical method we used to find T_c can be found in Refs. [40, 41]. We modeled the Nb/Co/Cu/Co heterostructures as $S/F_f/N/F_p$ layered systems, where S represents the superconducting layer, F_f and F_p are the inner (free) and outer (pinned) magnets, and N denotes the normal metallic intermediate layer. The layers are assumed to be infinite in the x-z plane with a total thickness d in the y direction, which is perpendicular to the interfaces between layers. In accordance with the experiment, F_p has width d_p, and fixed direction of magnetization. The normal layer with width d_n is sandwiched between this pinned layer and a magnetic layer F_f of width d_f with experimentally controlled magnetization direction. The superconducting layer of thickness d_S is in contact with the free layer. The in-plane magnetizations in the F layers are modeled by effective Stoner-type exchange fields $\mathbf{h}(y)$ which vanish in the nonferromagnetic layers. To accurately describe the physical properties of our

systems with sizes in the nanometer scale and moderate exchange fields, where semiclassical approximations are inappropriate, we numerically solve the microscopic Bogoliubov–de Gennes (BdG) equations in a fully self-consistent manner. The geometry of our system allows one to express the BdG equations in a quasi-one-dimensional form (natural units $\hbar = k_B = 1$ are assumed),

$$\begin{pmatrix} \mathcal{H}_0 - h_z(y) & -h_x(y) & 0 & \Delta(y) \\ -h_x(y) & \mathcal{H}_0 + h_z(y) & \Delta(y) & 0 \\ 0 & \Delta(y) & -(\mathcal{H}_0 - h_z(y)) & -h_x(y) \\ \Delta(y) & 0 & -h_x(y) & -(\mathcal{H}_0 + h_z(y)) \end{pmatrix} \begin{pmatrix} u_{n\uparrow}(y) \\ u_{n\downarrow}(y) \\ v_{n\uparrow}(y) \\ v_{n\downarrow}(y) \end{pmatrix} = \epsilon_n \begin{pmatrix} u_{n\uparrow}(y) \\ u_{n\downarrow}(y) \\ v_{n\uparrow}(y) \\ v_{n\downarrow}(y) \end{pmatrix}, \tag{5.2}$$

where $h_i(y)$ $(i = x, z)$ are components of the exchange fields $\mathbf{h}(y)$. In Eq. (5.2), the single-particle Hamiltonian $\mathcal{H}_0 = -1/(2m)d^2/dy^2 - E_F + U(y)$ contains the Fermi energy, E_F, and an effective interfacial scattering potential described by delta functions of strength H_j (j denotes the different interfaces); namely,

$$\begin{aligned} U(y) =& H_1\delta(y - d_S) + H_2\delta(y - d_S - d_f) \\ &+ H_3\delta(y - d_S - d_f - d_n), \end{aligned} \tag{5.3}$$

where $H_j = k_F H_{Bj}/m$ is written in terms of the dimensionless scattering strength H_{Bj}. We assume $h_x(y) = h_0 \sin(-\alpha/2)$ and $h_z(y) = h_0 \cos(-\alpha/2)$ in $\mathrm{F_f}$, where h_0 is the magnitude of exchange field. In $\mathrm{F_p}$, we have $h_x(y) = h_0 \sin(\alpha/2)$ and [24] $h_z(y) = h_0 \cos(\alpha/2)$. The functions $u_{n\sigma}$ and $v_{n\sigma}$ ($\sigma =\uparrow, \downarrow$) in Eq. (5.2) represent quasiparticle and quasihole wave functions. By applying the generalized Bogoliubov transformations (see Ref. [23]), the self-consistent singlet pair potential $\Delta(y)$ can be expressed in terms of quasiparticle and quasihole

wave functions; that is,

$$\Delta(y) = \frac{g(y)}{2}\sum_{n}{}' \left[u_{n\uparrow}(y)v_{n\downarrow}(y) + u_{n\downarrow}(y)v_{n\uparrow}(y)\right] \tanh\left(\frac{\epsilon_n}{2T}\right), \tag{5.4}$$

where the primed sum means summing over all eigenstates with energies ϵ_n that lie within a characteristic Debye energy ω_D, and $g(y)$ is the superconducting coupling strength, taken to be constant in the S region and zero elsewhere. We have assumed that the quantization axis lies along the z direction, but one can easily obtain the spin-dependent quasiparticle amplitudes with respect to a different spin quantization axis rotated by an angle θ in the x-z plane via the rotation matrix [23]:

$$\hat{U}_0(\theta) = \cos(\theta/2)\hat{\mathrm{I}} \otimes \hat{\mathrm{I}} - i\sin(\theta/2)\rho_z \otimes \sigma_z, \tag{5.5}$$

where $\boldsymbol{\rho}$ and $\boldsymbol{\sigma}$ are vectors of Pauli matrices in particle-hole and spin space, respectively.

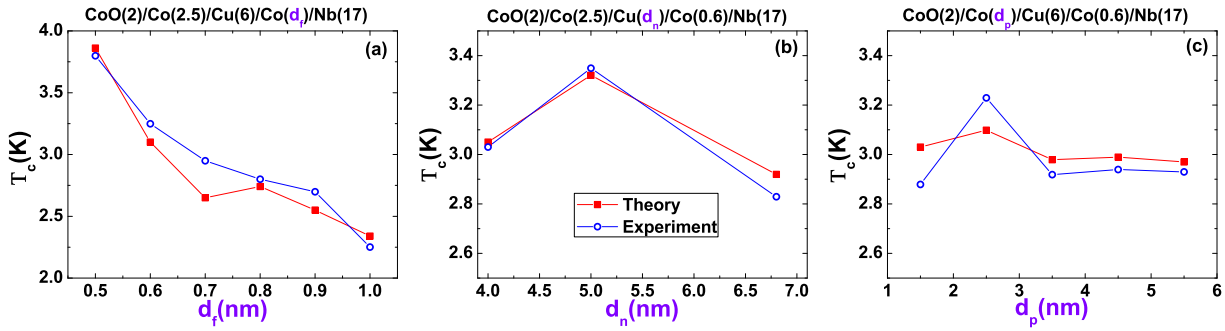

Figure 5.7: **Experimental data and theoretical fitting** of T_c in the P state as a function of (a) the Co free layer thickness d_f (with $d_n = 6$ nm and $d_p = 2.5$ nm), (b) the Cu normal metal layer thickness d_n (with $d_p = 2.5$ nm and $d_f = 0.6$ nm), and (c) the Co pinned layer thickness d_p (with $d_n = 6$ nm and $d_f = 0.6$ nm).

In principle, one can obtain the superconducting transition temperatures by computing the temperature dependence of $\Delta(y)$ and identifying the critical temperature where $\Delta(y)$ vanishes. However, the property that the pair potential is vanishingly small near T_c permits

one to linearize the self-consistency condition, that is, to rewrite it near T_c in the form

$$\Delta_i = \sum_q J_{iq} \Delta_q, \tag{5.6}$$

where the Δ_i are expansion coefficients in a given basis and the J_{iq} are the appropriate matrix elements with respect to the same basis. To determine T_c, one can simply compare the largest eigenvalue, λ, of the matrix J with unity at a given temperature. The system is in the superconducting state when λ is greater than unity. More details of this efficient technique are discussed in Refs. [40, 41].

To analyze the correlation between the behavior of the superconducting transition temperatures and the existence of odd triplet superconducting correlations in our systems, we compute the induced triplet pairing amplitudes which we denote as f_0 (with $m = 0$ spin projection) and f_1 with ($m = \pm 1$) according to the equations [22, 23]

$$f_0(y,t) = \frac{1}{2} \sum_n \left[u_{n\uparrow}(y) v_{n\downarrow}(y) - u_{n\downarrow}(y) v_{n\uparrow}(y) \right] \zeta_n(t), \tag{5.7a}$$

$$f_1(y,t) = \frac{1}{2} \sum_n \left[u_{n\uparrow}(y) v_{n\uparrow}(y) + u_{n\downarrow}(y) v_{n\downarrow}(y) \right] \zeta_n(t), \tag{5.7b}$$

where $\zeta_n(t) \equiv \cos(\epsilon_n t) - i \sin(\epsilon_n t) \tanh(\epsilon_n/(2T))$. These triplet pair amplitudes are odd in time t and vanish at $t = 0$, in accordance with the Pauli exclusion principle.

5.5 Analysis

In this subsection, we present our theoretical analysis and compare the theoretical results with the experimental data. To find the theoretical T_c, we adopted the linearization method as discussed in Sec. 5.4. The fitting process is rather time-consuming since for every parameter set, one must evaluate T_c numerically as a function of the misalignment angle α,

making a least-squares fit unfeasible. The same situation occurs in Refs. [40, 42]. As in those works, we search within plausible regions of parameter space, and display here results of the best fit that we have found, which is not necessarily the best possible fit. There are a number of parameters at one's disposal and, when computing the theoretical values of T_c, we first have to keep the number of fitting parameters as small as possible. All of the relevant physical parameters that are related to the properties of the materials involved, such as the exchange field, and the effective superconducting coherence length, are required to be the same for all of the different samples when performing the fitting. However, for parameters that are affected by the fabrication processes such as the interfacial barrier strength, one can reasonably assume, as we do, that their values are somewhat different from sample to sample. We do find that the variation is small between different samples in each series. For the material parameters we have found that the best value of the effective Fermi wave vector is $k_F = 1\mathring{A}^{-1}$ and the effective superconducting coherence length $\xi_0 = 11.5\,\mathrm{nm}$. For the dimensionless exchange field $I \equiv h_0/E_F$ (normalized to Fermi energy), we have used, for Co, $I = 0.145$, which is consistent with previous work [23] ($I = 1$ corresponds to the half-metallic limit). For the superconducting transition temperature for a putative pure superconducting sample of the same quality as the material in the layers, we have used $T_c^0 = 4.5$ K. This is the same value previously found [40]. It is of course lower than the true bulk transition temperature of Nb but even for pure thin films a decrease in T_c is to be expected [43]. All of these parameters are kept invariant across all of the different samples, as mentioned earlier. Only the three interfacial barrier strengths are treated as adjustable from sample to sample during the fitting process. We assume, however, that the barrier strength is the same on both sides of the normal metal layer while that between the free ferromagnetic layer and the superconductor are weaker. For each series, the barrier varies somewhat from batch to batch.

They are found to be as follows: $H_{B1} = 0.2$, and both H_{B2} and H_{B3} vary from 0.64 to 0.7 for different batches in the d_f series. For the d_p series, we have $H_{B1} = 0.15$, $0.53 < H_{B2}$,

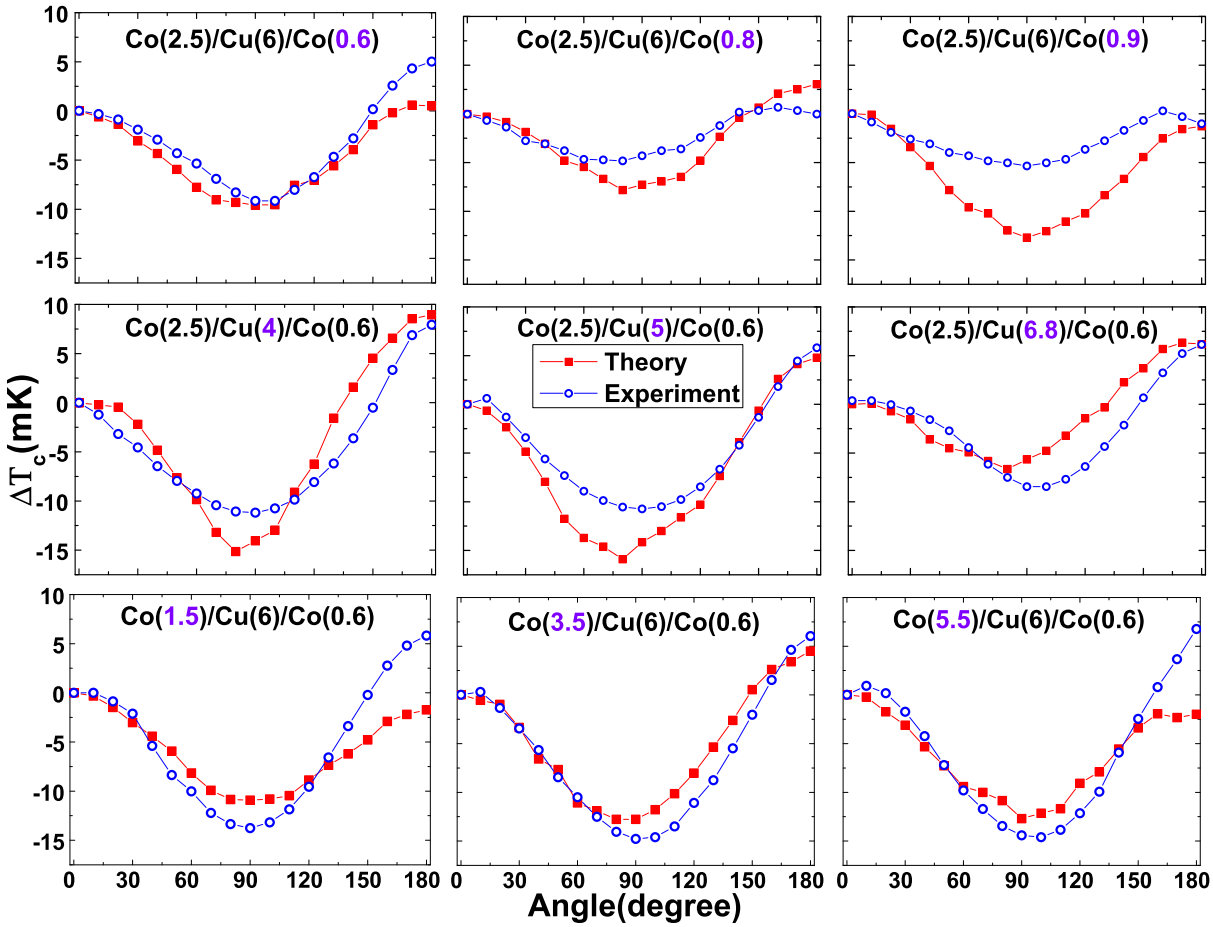

Figure 5.8: **Experiment and theory comparisons** of ΔT_c [defined as $\Delta T_c(\alpha) \equiv T_c(\alpha) - T_c(0)$] as a function of relative magnetization angle are shown for the three batches of samples. Top row: Three different free layer thicknesses, $d_f = 0.6$ nm, 0.8 nm, 0.9 nm, and with $d_p = 2.5$ nm, $d_n = 6$ nm. Middle row: Three different nonmagnetic layer thicknesses: $d_n = 4$ nm, 5 nm, 6.8 nm, and with $d_f = 0.6$ nm, $d_p = 2.5$ nm. Bottom row: Three different pinned layer thicknesses: $d_p = 1.5$ nm, 3.5 nm, 5.5 nm, and with $d_f = 0.6$ nm, $d_n = 6$ nm.

and $H_{B3} < 0.58$. The d_n series have H_{B1} ranges from 0.3 to 0.45 and $H_{B1} = H_{B2} = 0.62$. The thicknesses of the different layers are taken of course from their experimental values. As in Ref. [42] we find a thin magnetic "dead layer" between the normal metal and the free ferromagnetic layer of a small thickness in the range $0.27\,\text{nm} \sim 0.35\,\text{nm}$.

We now compare the experimental and theoretical values of T_c as a function of layer thicknesses and angle α for three different batches of samples: in one we vary d_f, in the second, d_n, and in the last, d_p. First, in Fig. 5.7, we present comparisons between experiment and theory, for the T_c results in the parallel state ($\alpha = 0$) as a function of thickness for the three

different series mentioned above. In all three series, the experimental and theoretical T_c are in very good agreement with each other. For the d_f series, one should notice that both experimental and theoretical T_c are very sensitive to the thicknesses of the free layers. When the thickness of the free ferromagnetic layer is increased, T_c decreases nonmonotonically by almost 50%. However, the d_n and d_p series do not show the same sensitivity, even though the ranges of thicknesses for these two series are much larger compared to that of the d_f series. This lower sensitivity is physically reasonable for the following reason: because of the presence of ferromagnets, we find that the magnitude of the singlet pairing amplitude decreases very fast beyond the boundary, in non-S regions away from the F/S interface. The exchange field reduces the proximity effect. Therefore, the size effects from the thicknesses of normal metal layers and pinned ferromagnetic layers are less. We also observe the trend that both theoretical and experimental T_c are often found to be a nonmonotonic function of the thicknesses of the F layers. In fact, except for the experimental T_c for d_f series, which does not show a clear oscillatory behavior, all other series clearly exhibit the nonmonotonicity of T_c. Oscillatory behavior of transition temperatures as one varies the thickness is standard in hybrid S/F heterostructures due to the oscillatory character of the pair amplitude [44] itself. The reason for the exception found might be that the data points are too widely spaced. This nonmonotonic behavior has been noted in past works [45, 46] and is often found [24] in FFS trilayers.

In Fig. 5.8, we present a detailed comparison of theoretical and experimental results for ΔT_c as a function of angle α between the magnetizations in the free and pinned layers for the d_f, d_n, and d_p series. Each panel in the first row in Fig. 5.8 represents different samples for d_f series. Results for the d_n and d_p series are plotted in the second and third row, respectively. One can clearly see that the behavior of the highly nonmonotonic angular dependencies of the theoretical results presented here describe very well the experimental results, not only qualitatively but also quantitatively: the magnitudes of the experimental and theoretical results for ΔT_c are comparable; both experimental and theoretical results

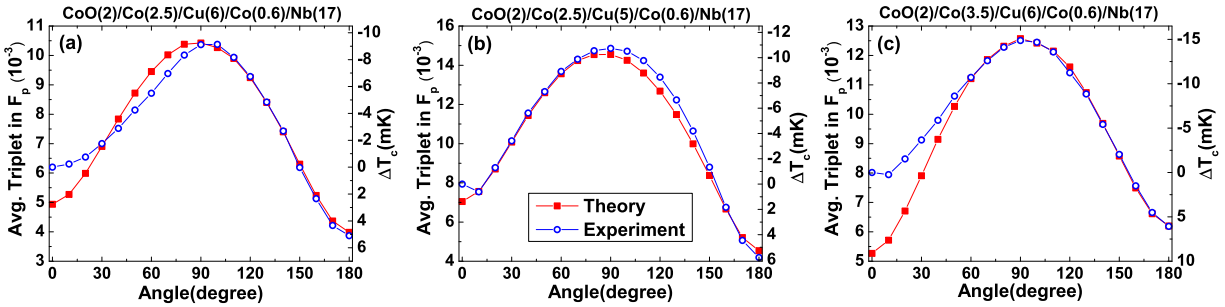

Figure 5.9: **Average triplet amplitudes in the pinned ferromagnet layer as a function of relative magnetization angle**. The quantity plotted is the average of $F_t(y,t)$ [Eq. (5.8)] in this region, at $\omega_D t = 4$. The quantity ΔT_c is also shown (right scale). Red squares are the theoretical triplet amplitudes (left scale) and the blue circles are the experimental ΔT_c (right inverted scale) as a function of angle. The ΔT_c data correspond to one set chosen from each batch of samples in Fig. 5.8. (a) From the d_f series, (b) from the d_n series, (c) from the d_p series.

indicate the switching effects are in about the 25 mK range. It is well worth recalling than in another recent work [40] results for the magnitude of this quantity differed by more than one order of magnitude. In contrast, here, taking into account the existence of numerical and experimental uncertainties (the former we estimate at ~ 1.5 mK), we find theory and experiment in very good agreement. This great improvement over Ref. [40] follows from the more careful treatment of the interface barriers from sample to sample and a much more extensive search in parameter space. For the d_f series, we see that the switching range for both experimental and theoretical $T_c(\alpha)$ varies nonmonotonically when d_f is increased. This occurs for the same reason already mentioned in the discussion of Fig. 5.7: the behavior of $T_c(\alpha)$ is very sensitive to the inner ferromagnetic layer thicknesses due to the proximity effect. Similarly, we observe that the switching ranges are less sensitive to the thickness of the outer ferromagnetic layer (see in the d_p series) and also to the normal metal layer thickness in the d_n series.

We now turn to the role that induced triplet correlations in the nonmonotonic behavior of $T_c(\alpha)$. This has been the subject of recent theoretical interest [24, 47, 48] but little has been done on quantitatively comparing theory and experiment. To examine this question in a quantitative way, we have computed the induced odd triplet pairing correlations. These

correlations (as well of course as the ordinary singlet correlations) can be self-consistently calculated using the methods previously described. As noted in Sec. 5.4, with the presence of nonhomogeneous magnetization the triplet pair amplitudes in general can be induced when $t \neq 0$. We present our study in terms of the quantity

$$F_t(y,t) \equiv \sqrt{|f_0(y,t)|^2 + |f_1(y,t)|^2}, \tag{5.8}$$

where the quantities involved are defined in Eq. (5.7). This quantity accounts for both triplet components, the equal spin and opposite spin triplet correlations. The reason to use this quantity is that via Eq. (5.5), one can easily show that, when the spin quantization axis is rotated by an angle θ, the rotated triplet pair amplitudes $\tilde{f}_0$ and $\tilde{f}_1$ after the transformation are related from the original f_0 and f_1 by

$$\tilde{f}_0(y,t) = \cos(\theta) f_0(y,t) - \sin(\theta) f_1(y,t), \tag{5.9a}$$

$$\tilde{f}_1(y,t) = \sin(\theta) f_0(y,t) + \cos(\theta) f_1(y,t). \tag{5.9b}$$

Therefore the quantity $F_t(y,t)$ that we focus on obviates any ambiguity issues related to the existence of generally non-collinear "natural" axes of quantization in the system.

We have computed this quantity as a function of position and α. It turns out to be particularly useful to focus on the average value of $F_t(y,t)$ in the pinned layer $\mathrm{F_p}$. We normalize this averaged quantity, computed in the low-T limit, to the value of the singlet pair amplitude in the bulk S. This normalized averaged quantity is plotted as a function of α in Fig. 5.9 (left vertical scale) at a dimensionless characteristic time $\omega_D t = 4.0$. This time value is unimportant, provided it be nonzero, of course. In the three panels, an example taken from each of the series is displayed, as explained in the caption. One can observe that the maxima of this average F_t occur when $\alpha = \pi/2$ and its minima are at either $\alpha = 0$ or $\alpha = \pi$. In the same figure (right vertical scale) the experimental values of $\Delta T_c(\alpha)$, for the

same cases, which have minima near $\pi/2$, are plotted in an inverted scale. The agreement is truly striking. The anticorrelation can be easily understood: the magnitude of the low-T singlet pair amplitudes is of course positively correlated to T_c. Here the fact that triplet pair amplitudes are anticorrelated to T_c (or to the singlet amplitudes) indicates a singlet-triplet conversion process: when more singlet superconductivity leaks into the ferromagnet side, T_c is suppressed and triplet superconductivity is enhanced. The average magnitude of the triplet pair amplitudes in the free and normal layer regions is only weakly dependent on α: Of importance is the propagation of triplet pairs throughout the entire system, generated by the symmetry-breaking interfaces and magnetic inhomogeneity created from the two misaligned ferromagnets. This clearly demonstrates a singlet to triplet process which is related to the nonmonotonicity of the transition temperature.

Bibliography

[9] L. N. Bulaevski, V. V. Kuzi, and A. A. Sobyanin. *Superconducting system with weak coupling to the current in the ground state*. 1977. URL: http://adsabs.harvard.edu/abs/1977JETPL..25..290B.

[10] A. I. Buzdin, L. N. Bulaevskii, and S. V. Panyukov. "Critical-current oscillations as a function of the exchange field and thickness of the ferromagnetic metal (F) in an S-F-S Josephson junction". In: *JETP Lett.* 35.l (1982), p. 178. URL: http://www.jetpletters.ac.ru/ps/1314/article{_}19853.pdf.

[11] T. Tokuyasu, J. A. Sauls, and D. Rainer. "Proximity effect of a ferromagnetic insulator in contact with a superconductor". In: *Phys. Rev. B* 38.13 (1988), pp. 8823–8833. ISSN: 01631829.

[12] V. V. Ryazanov et al. "Coupling of two superconductors through a ferromagnet: Evidence for a π junction". In: *Phys. Rev. Lett.* 86.11 (2001), pp. 2427–2430. ISSN: 00319007. arXiv: 0008364 [cond-mat].

[13] T Kontos et al. "Josephson Junction through a Thin Ferromagnetic Layer: Negative Coupling". In: *Phys. Rev. Lett.* 89.13 (2002), p. 137007. ISSN: 0031-9007. arXiv: 0201104v2 [cond-mat]. URL: http://link.aps.org/doi/10.1103/PhysRevLett.89.137007.

[14] A. I. Buzdin. "Proximity effects in superconductor-ferromagnet heterostructures". In: *Rev. Mod. Phys.* 77.3 (2005), pp. 935–976. ISSN: 00346861. arXiv: 0505583 [cond-mat].

[15] F. S. Bergeret, A. F. Volkov, and K. B. Efetov. "Odd triplet superconductivity in superconductor ferromagnet structures: A survey". In: *Appl. Phys. A Mater. Sci. Process.* 89.3 (2007), pp. 599–601. ISSN: 09478396. arXiv: 0602522 [cond-mat].

[16] Matthias Eschrig. "Spin-polarized supercurrents for spintronics". In: *Phys. Today* 64.1 (2011), pp. 43–49. ISSN: 00319228. arXiv: 1509.02242.

[17] Klaus Halterman and Oriol T. Valls. "Proximity effects and characteristic lengths in ferromagnet-superconductor structures". In: *Phys. Rev. B* 66.22 (2002), p. 224516. ISSN: 0163-1829. arXiv: 0205518 [cond-mat]. URL: http://arxiv.org/abs/cond-mat/0205518$\backslash$nhttp://link.aps.org/doi/10.1103/PhysRevB.66.224516.

[18] R S Keizer et al. “A spin triplet supercurrent through the half-metallic ferromagnet CrO2.” In: *Nature* 439.7078 (2006), pp. 825–7. ISSN: 1476-4687. arXiv: 0602359 [cond-mat]. URL: http://www.ncbi.nlm.nih.gov/pubmed/16482152.

[19] Jian Wang et al. “Interplay between superconductivity and ferromagnetism in crystalline nanowires”. In: *Nat. Phys.* 6.5 (2010), p. 389. ISSN: 1745-2473. URL: http://dx.doi.org/10.1038/nphys1621.

[20] C. Visani et al. “Equal-spin Andreev reflection and long-range coherent transport in high-temperature superconductor/half-metallic ferromagnet junctions”. In: *Nat. Phys.* 8.7 (2012), pp. 539–543. ISSN: 1745-2473.

[21] F. H{\”u}bler et al. “Observation of Andreev bound states at spin-active interfaces”. In: *Phys. Rev. Lett.* 109.8 (2012), pp. 1–5. ISSN: 00319007. arXiv: 1012.3867.

[22] Klaus Halterman, Paul H. Barsic, and Oriol T. Valls. “Odd triplet pairing in clean superconductor/ferromagnet heterostructures”. In: *Phys. Rev. Lett.* 99.12 (2007), pp. 1–4. ISSN: 00319007. arXiv: 0704.1820.

[23] Klaus Halterman, Oriol T. Valls, and Paul H. Barsic. “Induced triplet pairing in clean s -wave superconductor/ferromagnet layered structures”. In: *Phys. Rev. B - Condens. Matter Mater. Phys.* 77.17 (2008), pp. 1–14. ISSN: 10980121.

[24] Chien-Te Wu, Oriol T. Valls, and Klaus Halterman. “Proximity effects and triplet correlations in ferromagnet/ferromagnet/superconductor nanostructures”. In: *Phys. Rev. B* 86.1 (2012), p. 014523. ISSN: 1098-0121. arXiv: arXiv:1207.1325v1. URL: http://link.aps.org/doi/10.1103/PhysRevB.86.014523.

[25] J W A Robinson, J D S Witt, and M G Blamire. “Controlled Injection of Spin-Triplet Supercurrents into a Strong Ferromagnet”. In: *Science (80-.).* 329.5987 (2010), pp. 59–61. ISSN: 0036-8075, 1095-9203. URL: http://www.sciencemag.org/content/329/5987/59.

[26] Trupti S. Khaire et al. “Observation of spin-triplet superconductivity in co-based josephson junctions”. In: *Phys. Rev. Lett.* 104.13 (2010), pp. 2–5. ISSN: 00319007. arXiv: 0912.0205.

[27] M. S. Anwar et al. “Long range supercurrents in ferromagnetic CrO 2 using a multilayer contact structure”. In: *Appl. Phys. Lett.* 100.5 (2012), pp. 2–5. ISSN: 00036951. arXiv: arXiv:1111.5809v1.

[28] S.D. Gu, J.Y. ; You, C.-Y. ; Jiang, J. S.; Pearson, J.; Bazaliy, Ya. B.; Bader. “Magnetization-Orientation Dependence of the Superconducting Transition Temperature in the Ferromagnet-Superconductor-Ferromagnet System: CuNi=Nb=CuNi”. In: *Phys. Rev. Lett.* 89.15 (2002), p. 157004. ISSN: 0031-9007. URL: http://link.aps.org/doi/10.1103/PhysRevLett.89.157004.

[29] Ion C. Moraru, W. P. Pratt, and Norman O. Birge. “Observation of standard spin-switch effects in ferromagnet/superconductor/ ferromagnet trilayers with a strong ferromagnet”. In: *Phys. Rev. B - Condens. Matter Mater. Phys.* 74.22 (2006), pp. 1–4. ISSN: 10980121.

[30] J. Y. Gu, Jefery Kusnadi, and Chun Yeol You. "Proximity effect in a superconductor/exchange-spring-magnet hybrid system". In: *Phys. Rev. B - Condens. Matter Mater. Phys.* 81.21 (2010), pp. 1–6. ISSN: 10980121.

[31] P. V. Leksin et al. "Evidence for triplet superconductivity in a superconductor-ferromagnet spin valve". In: *Phys. Rev. Lett.* 109.5 (2012), pp. 1–5. ISSN: 00319007. arXiv: arXiv:1207.0727v1.

[32] Yaohua Liu et al. "Effect of interface-induced exchange fields on cuprate-manganite spin switches". In: *Phys. Rev. Lett.* 108.20 (2012), pp. 1–5. ISSN: 00319007. arXiv: 1201.2707.

[33] V. I. Zdravkov et al. "Experimental observation of the triplet spin-valve effect in a superconductor-ferromagnet heterostructure". In: *Phys. Rev. B - Condens. Matter Mater. Phys.* 87.14 (2013), pp. 1–6. ISSN: 10980121.

[34] L. Y. Zhu et al. "Unanticipated proximity behavior in ferromagnet-superconductor heterostructures with controlled magnetic noncollinearity". In: *Phys. Rev. Lett.* 110.17 (2013), pp. 1–5. ISSN: 00319007. arXiv: 1304.6071.

[35] Bin Li et al. "Superconducting spin switch with infinite magnetoresistance induced by an internal exchange field". In: *Phys. Rev. Lett.* 110.9 (2013), pp. 1–5. ISSN: 00319007.

[36] G Nowak, K Westerholt, and H Zabel. "Asymmetric superconducting spin valves based on the Fe/V layer system grown on MgO(100)". In: *Supercond. Sci. Technol.* 26.2 (2013), p. 025004. ISSN: 0953-2048. URL: http://stacks.iop.org/0953-2048/26/i=2/a=025004?key=crossref.1cc6e458e47c52ef6da752e42d1d66a7.

[37] T. Gredig et al. "Rotation of exchange anisotropy in biased Co/CoO bilayers". In: *J. Appl. Phys.* 87.9 III (2000), pp. 6418–6420. ISSN: 00218979.

[38] K. P. Parkin, S. S. P. ; Bhadra, R. ; Roche. "Oscillatory Magnetic Exchange Coupling through Thin Copper Layers". In: *Phys. Rev. Lett.* 66.16 (1991), pp. 2152–2155.

[39] J. Zhu et al. "Origin of the inverse spin switch effect in superconducting spin valves". In: *Phys. Rev. Lett.* 103.2 (2009), pp. 1–4. ISSN: 00319007. arXiv: 0903.0044.

[40] Jian Zhu et al. "Angular dependence of the superconducting transition temperature in ferromagnet-superconductor-ferromagnet trilayers". In: *Phys. Rev. Lett.* 105.20 (2010), pp. 1–4. ISSN: 00319007. arXiv: 1010.1752.

[41] Paul H. Barsic, Oriol T. Valls, and Klaus Halterman. "Thermodynamics and phase diagrams of layered superconductor/ferromagnet nanostructures". In: *Phys. Rev. B - Condens. Matter Mater. Phys.* 75.10 (2007), pp. 1–12. ISSN: 10980121.

[42] F. Chiodi et al. "Supra-oscillatory critical temperature dependence of Nb-Ho bilayers". In: *EPL (Europhysics Lett.* 101.3 (2013), p. 37002. ISSN: 0295-5075. arXiv: arXiv:1211.1169v1. URL: http://stacks.iop.org/0295-5075/101/i=3/a=37002?key=crossref.4541cbc0372719e1539fa2523d56b198.

[43] Stuart A. Wolf, James J. Kennedy, and Martin Nisenoff. "Properties of superconducting rf sputtered ultrathin films of Nb". In: *J. Vac. Sci. Technol.* 13.1 (1976), pp. 145–147. ISSN: 0022-5355. URL: http://scitation.aip.org/content/avs/journal/jvst/13/1/10.1116/1.568809$\backslash$nhttp://scitation.aip.org/deliver/fulltext/avs/journal/jvst/13/1/1.568809.pdf?itemId=/content/avs/journal/jvst/13/1/10.1116/1.568809{\&}mimeType=pdf{\&}containerItemId=content/avs/journal/j.

[44] E. a. Demler, G. B. Arnold, and M. R. Beasley. "Superconducting proximity effects in magnetic metals". In: *Phys. Rev. B* 55.22 (1997), pp. 15174–15182. ISSN: 0163-1829.

[45] Zoran Radovi\'{c} et al. "Transition temperatures of superconductor-ferromagnet superlattices". In: *Phys. Rev. B* 44.2 (1991), pp. 759–764. ISSN: 01631829.

[46] J. S. Jiang et al. "Oscillatory superconducting transition temperature in Nb/Gd multilayers". In: *Phys. Rev. Lett.* 74.2 (1995), pp. 314–317. ISSN: 00319007.

[47] Ya. V. Fominov et al. "Superconducting triplet spin valve". In: *JETP Lett.* 91.6 (2010), pp. 308–313. ISSN: 0021-3640. arXiv: 1002.2113.

[48] T. Yu Karminskaya, A. A. Golubov, and M. Yu Kupriyanov. "Anomalous proximity effect in spin-valve superconductor/ferromagnetic metal/ferromagnetic metal structures". In: *Phys. Rev. B - Condens. Matter Mater. Phys.* 84.6 (2011), pp. 1–5. ISSN: 10980121.

Chapter 6

Highly textured $IrMn_3(111)$ thin films grown by magnetron sputtering

The contents of this chapter are adapted from work originally published as *IEEE Magn. Lett.* ***7****, 3104805 (July 2016).*

6.1 Introduction

In spintronics, antiferromagnets (AFs) are almost exclusively used for pinning of magnetization direction of ferromagnets via exchange bias [5, 49–52]. However, many intrinsic AF properties are superior to those of ferromagnets, which makes the AFs promising candidates for a broader class of spintronic applications [53–66]. Zero magnetization makes the AF order parameter immune to perturbations by magnetic fields, which is attractive for high-density AF-based memory applications [54–57]. Furthermore, high magnetic anisotropy fields found in many uniaxial AFs can be used to achieve high thermal stability of nano-magnetic devices. The high group velocity of spin-waves in AFs [58, 59] is attractive for spin-wave based logic.

Recently, AFs have been shown to transmit spin-currents originating from an adjacent ferromagnet. In addition, the spin-orbit interaction in metallic AFs can be employed to detect spin currents via inverse spin Hall effect (ISHE) [60–64]. To fully exploit the potential of AFs, a means to read out their magnetic state and to detect magnetization excitations must be established [65]. It has been pointed out recently that non-collinear spin states in AFs can be efficiently used for spin-charge conversion. Non-trivial spin structures can allow charge carriers to acquire a Berry phase, leading to significant spin-charge coupling [66].

The chemically ordered $L1_2$ phase of $IrMn_3$ supporting a non-collinear AF spin ground state has been predicted [67] to exhibit large anomalous Hall effect (AHE) [68, 69]. This makes $IrMn_3$ a promising candidate for antiferromagnetic spintronics and motivates our study of growth of this material by magnetron sputtering. $IrMn_3$ in the $L1_2$ phase has an fcc-type crystallographic structure with lattice parameter 0.3778 nm. As shown in Fig. 6.1(a), Ir atoms occupy the corners of the cubic unit cell [70–74] while the Mn atoms occupy the six faces of the unit cell. The Mn atoms form a kagome lattice in the {111}-planes (Fig. 6.1(b)). Due to the large magnetic anisotropy and exchange energies, the Mn spins order in the non-collinear T1 ground state within the {111}-planes as shown in Fig. 6.1. This non-collinear ground state causes deflection of electric current flowing in the (111)-plane and gives rise to the AHE [67]. Signatures of this effect have been recently observed in polycrystalline IrMn films and also in similar systems such as $SnMn_3$ [75], and $GeMn_3$ [76].

In this study, we present a method of growth of highly textured (111) thin films of $L1_2$-$IrMn_3$ by sputter deposition. We employ X-ray diffraction (XRD) to investigate the crystallographic texture, epitaxial order, lattice parameter, and chemical order of the films.

Sample	d_{MgO}	d_{Ir}	d_{IrMn_3}	d_{Ir}	d_{Ge}
1	5	6	120	5	10
2	30	30	80	5	10
3	5	3	40	3	10
4	0	5	40	3	10
5	0	3	40	3	10

Table 6.1: Thickness of the layers in nanometers.

6.2 Film Preparation

We deposited a series of continuous film samples with the structure: MgO(111) substrate / MgO (d_0) / Ir (d_1) / $IrMn_3$ (d_2) / Ir (d_3) / Ge (10 nm), the thicknesses are shown in Table 1. The MgO substrate was treated by *in situ* annealing at 400 °C for 30 min. For a subset of samples, an MgO buffer layer ($d_0 > 0$) was deposited by evaporation at room temperature. Without breaking the vacuum, a buffer layer of Ir was deposited by sputtering, followed by the $IrMn_3$ layer which was co-sputtered from Ir and $Ir_{20}Mn_{80}$ targets at 0.14 nm/s. The composition of $IrMn_3$ was confirmed by X-ray fluorescence on test films. To prevent oxidation of $IrMn_3$, a bilayer cap of Ir and Ge was deposited. The deposition of Ir and $IrMn_3$ was carried out at a substrate temperature of 250 °C with subsequent annealing at 400 °C for 30 min. A set of samples that differ by the thicknesses of the layers d_n was fabricated.

6.3 Film Characterization

The XRD measurements were performed using a Rigaku SmartLab diffractometer at room temperature, employing K_α(Cu) radiation and a scintillator detector combined with a diffraction beam monochromator.

We carried out grazing incidence X-ray diffraction (GIXRD) measurements. The inset in Fig. 6.2 shows the schematic of the experiment. $\vec{S}$ is the diffraction vector which bisects the

angle between the incident and scattered beam. The angle ω between the incident beam and the sample surface was adjusted for each sample to an optimal value of approximately 1° in order to increase the intensity of the diffracted beam. Figure 2 shows GIXRD spectra of five representative $IrMn_3$ samples, labeled from 1 to 5. Two types of samples are presented: with MgO buffer layer (samples 1, 2, and 3) and without MgO buffer layer (samples 4 and 5). The samples with MgO buffer layer show several peaks arising from $IrMn_3$. The presence of multiple peaks indicates that the samples have no strong out-of-plane texture. Samples with thick Ir buffer layer, such as sample 2, present observable peaks of Ir. The samples without MgO buffer layer do not show any diffraction peaks, indicating that they are either strongly textured or amorphous.

We performed the $\theta/2\theta$ XRD measurements. The data were collected after alignment of the diffraction vector $\vec{S}$ parallel to the [111] direction of the MgO substrate. In Fig. 6.3, the $\theta/2\theta$ XRD data show that for the samples without MgO buffer layer, only the (111) and (222) reflection peaks appear. Consequently, these samples must be strongly out-of-plane textured. In contrast, samples with MgO buffer layer show negligible out-of-plane texture because of the presence of other peaks such as (200) and the absence of the (222) peak.

We focus on the samples without MgO buffer layer (4 and 5) exhibiting high degree of out-of-plane texture. Figure 4(a) shows the $\theta/2\theta$ XRD measurement of the out-of-plane (111) peak for sample 4. By applying the Scherrer equation, we deduce the vertical grain size to be at least 15 nm, which is comparable to the values reported for $IrMn_3$ samples prepared by molecular beam epitaxy [73]. Using the same alignment procedure as for $\theta/2\theta$ XRD measurements, a rocking curve was obtained for the out-of-plane $IrMn_3$ (111) peak. As shown in Fig. 6.4(b), the full width at half-maximum of the peak is 2.8°. This result is comparable to the mosaic spread of 2° for the epitaxial film grown by molecular beam epitaxy reported by Kohn *et al.* [74].

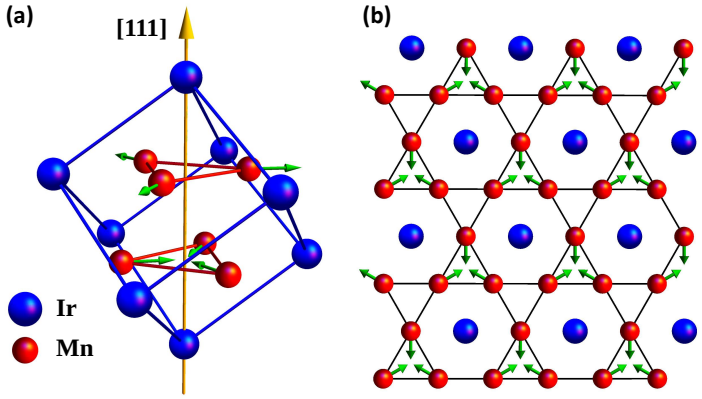

Figure 6.1: **Crystallographic structure of $IrMn_3$.** (a) Unit cell of $IrMn_3$ in the $L1_2$ phase. Green arrows indicate the magnetic moments of Mn. (b) A (111) plane of $IrMn_3$ in the $L1_2$ phase.

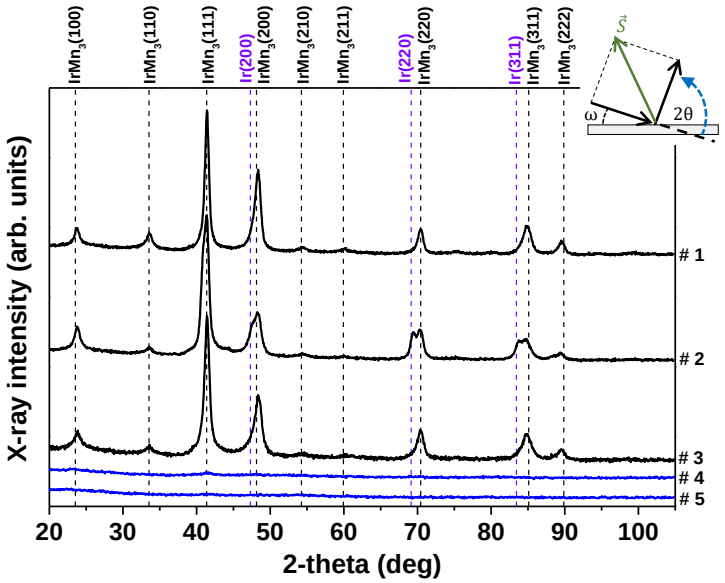

Figure 6.2: **Grazing incident XRD profiles.** The vertical axis is linear. The inset shows the schematic of the experiment.

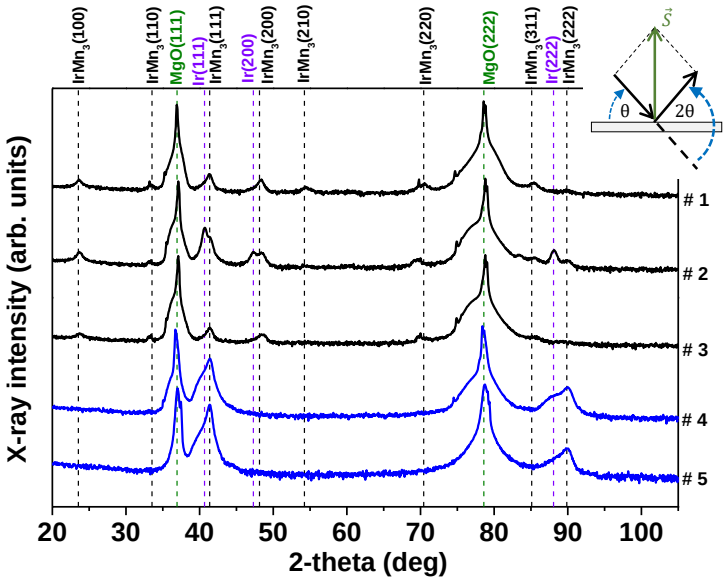

Figure 6.3: **XRD $\theta/2\theta$ scans.** The vertical axis is logarithmic. The inset shows the schematic of the experiment.

In order to evaluate the in-plane texture, we carried out XRD measurements where the diffraction angle 2θ and thus the magnitude of the diffraction vector is fixed. By rotating the sample, the diffracted intensity is measured as a function of azimuthal and polar angles of the diffraction vector in the hemisphere around the film normal. This measurement provides pole figures for two reflections, (100) and (111), from the $IrMn_3$ layer. The diffraction angles for these measurements are $2\theta = 23.53°$ and $41.36°$, respectively. Figures 5(a) and 5(b) show pole figures of an untextured sample. By performing XRD 2θ scan along the direction of the small sharp peaks present in Fig. 6.5(b), we find that these are artifacts due to a residual signal from the tail of the high-intensity MgO (200) reflection peaks. Besides this artifact, there is no anisotropic intensity distribution and therefore the sample has no texture – the crystallographic grains of the sample are randomly oriented.

Figures 5(c) and (d) show pole figures of a sample with out-of-plane texture for the (100) and (111) diffraction peaks. Each pole figure shows a set of peaks with a six-fold symmetry. The presence of the six peaks can be interpreted as two groups of three-fold peaks rotated with respect to each other by 60° in the sample plane. The intensity of one group is slightly

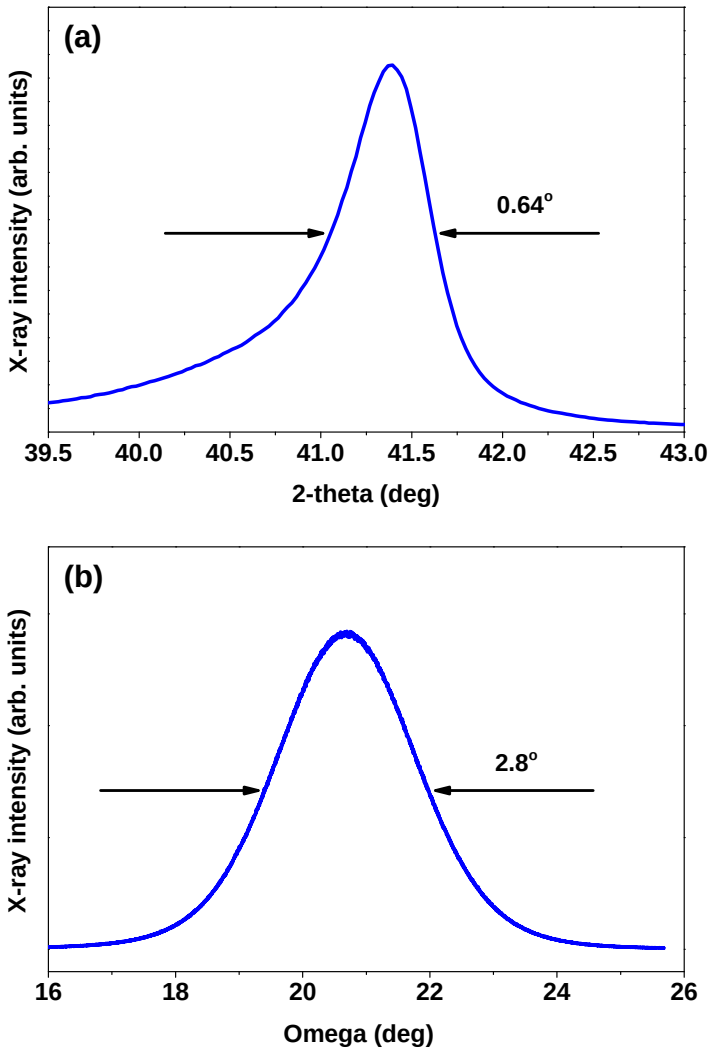

Figure 6.4: **XRD analysis of a peak.** XRD analysis of the out-of-plane (111) $IrMn_3$ reflection of the textured sample 4: (a) $\theta/2\theta$ and (b) Rocking curve.

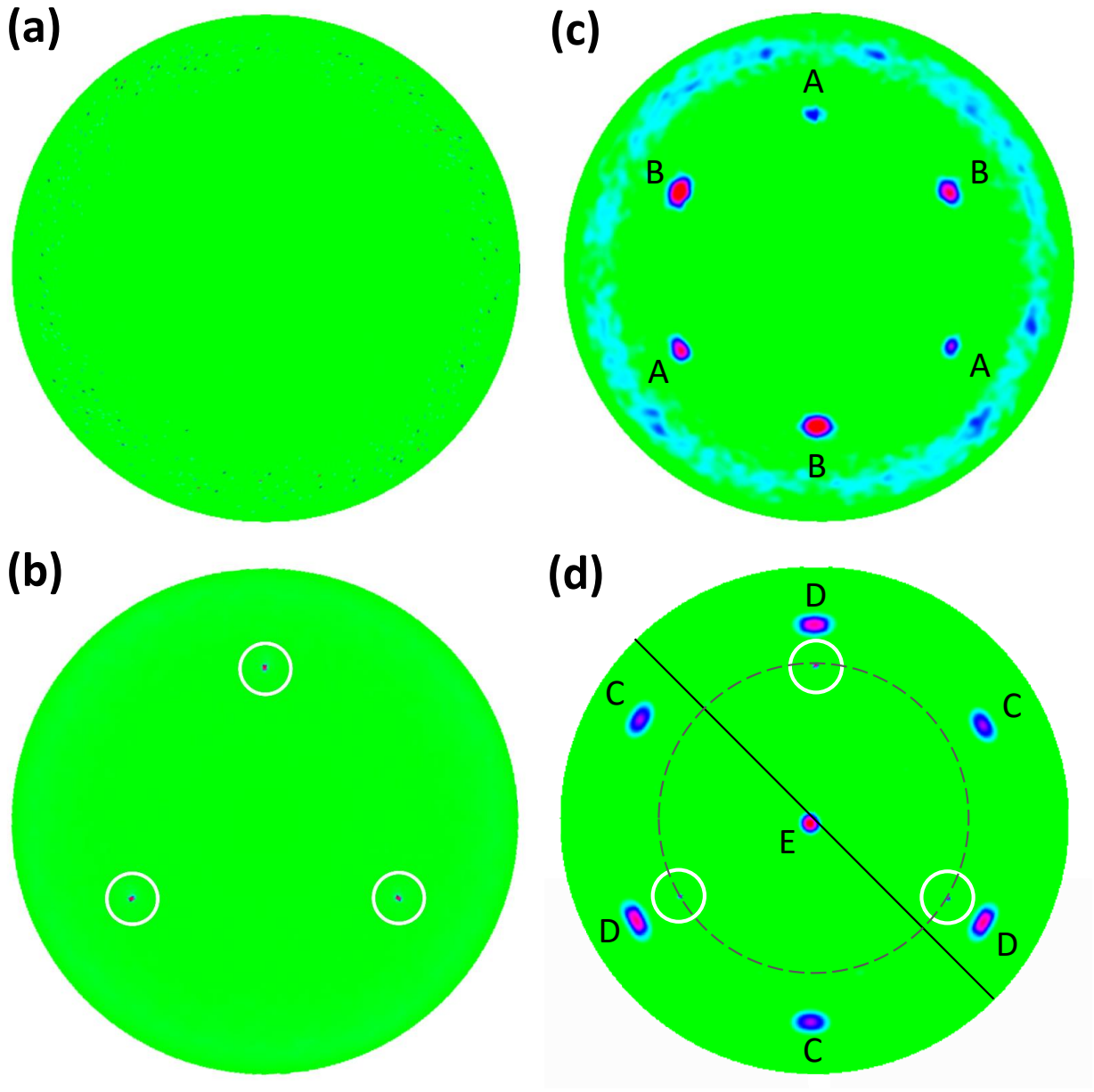

Figure 6.5: **XRD pole figures.** XRD pole figures of the (100) reflections ($2\theta = 23.53°$) of the untextured sample 3 (a) and textured sample 4 (c); the (111) reflections ($2\theta = 41.36°$) of untextured sample 3 (b) and textured sample 4 (d). The sets of peaks A and B have a polar angle of 54.7° which is the same as for the $\langle 100 \rangle$ directions of $IrMn_3$. C and D peaks have a polar angle of 70.5°, corresponding to $\langle 111 \rangle$ peaks of $IrMn_3$. A and C are sets of peaks of the weak phase, B and D represent the strong phase. E marks the [111] peak of $IrMn_3$ which is shared by both phases. Enclosed in a white circles are the residual signal from the tail of the MgO (200) reflection peaks.

higher than that of the other. The dominant set of peaks is 60° in-plane rotated from crystallographically analogous MgO peaks. The flanks of the (200) MgO peaks in Fig. 6.5(d) have the same position as the (100) peaks of the weaker $IrMn_3$ phase in Fig. 6.5(c), indicating parallel sets of directions. The presented experimental data suggest crystal twinning. Such rotational twinning was found in epitaxial ultrathin Pt films on sapphire. Typically in an fcc-structure, twin crystals form at the stacking faults on consecutive {111} planes. Our data cannot contribute to determining which of the many stacking faults are predominant in the films [77].

The (100) and (111) peaks in Figs. 5(c,d) lie on a circle. The center of the circle is 2° off the center of the pole figure, whereas we ensured that the figure center coincides with the out-of-plane (111) MgO peak. In Fig. 6.5(d), the dashed circle overlaps with the (200) MgO peaks confirming the perfect alignment of our measurement with the substrate crystal structure. The diametral line does not collide with the (111) $IrMn_3$ peak which therefore does not have the same position as the (111) MgO peak. The miscut of the MgO substrate is negligible (less than 0.1°), as we confirmed by surface reflectivity measurements. The [111] direction of the $IrMn_3$ is tilted off the sample normal in a direction not coinciding with any principal crystallographic axis. The films were sputtered using a rotating sample stage, such that oblique deposition can be excluded. A possible explanation of this small tilt of the crystallographic axis is spontaneous symmetry breaking at the initial stage of the film growth, facilitated by the lattice mismatch between the substrate and the film layers ($a_{\mathrm{MgO}} = 0.421\,\mathrm{nm}$, $a_{\mathrm{Ir}} = 0.384\,\mathrm{nm}$, and $a_{\mathrm{IrMn}} = 0.3778\,\mathrm{nm}$). The lattice parameter of $0.3777(3)\,\mathrm{nm}$ for the untextured samples indicates growth of unstrained material (bulk lattice parameter $0.3778\,\mathrm{nm}$). For the textured samples, the distance between the {111} planes along the film normal is $d_{\{111\}}^{[111]} = \sqrt{1/3} \cdot 0.378\,\mathrm{nm}$, which is very close to the bulk value of $IrMn_3$. However, for the oblique [100] direction, the lattice parameter $a = 0.380\,\mathrm{nm}$ is larger than bulk value, indicating the presence of in-plane tensile strain, which in consistent with the fact that the Ir seed layer has a larger bulk lattice parameter $a = 0.384\,\mathrm{nm}$.

After the crystallographic structure has been deduced, we evaluate the chemical order. The fundamental (F) peaks of $IrMn_3$, such as (200), are present for both chemically ordered and disordered phases. The sublattice (S) peaks, such as (100), are present for the ordered phase only. By comparing the intensities of the fundamental and sublattice peaks it is thus possible to determine the chemical order (C) of the sample. The chemical order parameter ranges from 0 for samples lacking any chemical order to 1 for samples with the perfect $L1_2$ order. As detailed in Ref. xx, the chemical order is:

$$C = \sqrt{\frac{I_S(f_{Ir} + 3f_{Mn})^2 L(\theta_F) P(\theta_F) e^{-2M(\theta_F)}}{I_F(f_{Ir} - f_{Mn})^2 L(\theta_S) P(\theta_S) e^{-2M(\theta_S)}}} \tag{6.1}$$

Here, I, $L(\theta)$, $P(\theta)$, and $e^{-2M(\theta)}$ are the integrated intensity, Lorentz factor, polarization factor, and absorption factor, respectively. In Eq. 6.1, $(f_{\mathrm{Ir}} - f_{\mathrm{Mn}})$ and $(f_{\mathrm{Ir}} + 3f_{\mathrm{Mn}})$ are the structural factors of the superlattice and fundamental peaks, respectively. The (100) and (200) peaks were chosen as the superlattice and fundamental peaks. For untextured samples, the chemical order parameter was calculated using the GIXRD data. We find the chemical order parameter to be 0.75. For the textured samples, the Lorentz factor can be omitted in Eq. 6.1. In order to assess the intensity of the (100) and (200) peaks, we align the diffraction vector along the [100] direction and observe the diffraction intensity while varying its magnitude in a 2θ measurement (see Fig. 6.6). We find the chemical order parameter for textured samples to be 0.45. We conclude that the additional evaporated MgO buffer layer increases the chemical ordering parameter, but destroys the crystallographic (111) texture of the $IrMn_3$ films.

Observation of the anomalous Hall effect in $IrMn_3$ films requires the $L1_2$ chemical order, strong (111) out-of-plane texture, and the T1 non-collinear spin order. The presence of the superlattice (100) peak in our highly textured films (Fig. 6.6) indicates a significant fraction,

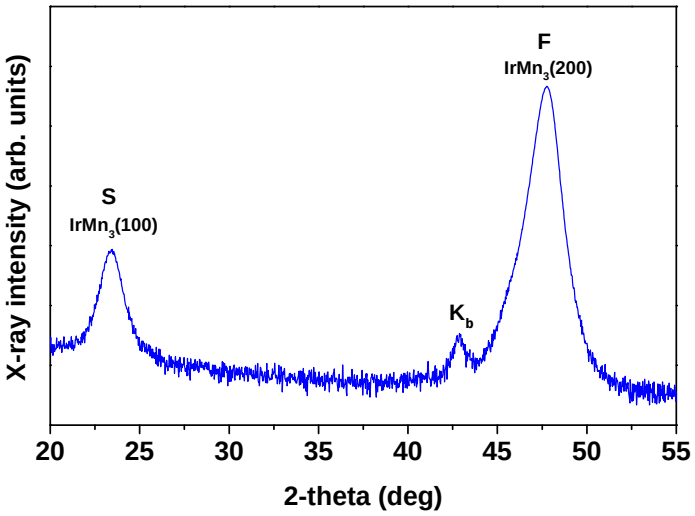

Figure 6.6: **XRD 2θ scan along [100] direction.** XRD 2θ scan along [100] direction of the strong phase for the textured sample 4. The vertical axis is logarithmic intensity. The feature marked K_β at 42.85° is an artifact due to residual K_β(Cu) radiation. F and S indicate the fundamental and the superlattice peaks.

C, of $L1_2$ ordered crystallites embedded in a matrix of other crystallites lacking this chemical order. The $L1_2$ crystallites can be expected to establish the T1 spin order [67] and give rise to AHE signal in these films, which will be only partially shunted by the chemically disordered matrix. The $T1_2$ spin structure in $IrMn_3$ is expected to maintain a small magnetic moment oriented perpendicular to the {111} plane due to small spin canting [67]. Thus, a sufficiently strong external out-of-plane magnetic field can be used to switch the $IrMn_3$ AF domains into a single-domain (111) out-of-plane state necessary for the observation of a large AHE signal [67].

6.4 Conclusion

In conclusion, we deposited $IrMn_3$ thin films onto MgO(111) substrates with MgO/Ir and Ir buffer layers by magnetron sputtering and examined their crystallographic properties via X-ray diffractometry. We find that the films grown on MgO/Ir buffer layers exhibit a high

degree of $L1_2$ chemical ordering but lack any crystallographic texture; conceivably, MgO deposition at higher temperatures may improve the film growth. The films grown on Ir buffer layer are highly textured with strong out-of-plane and in-plane crystallographic order. For these highly textured films, the vertical grain size is 15 nm and the out-of-plane mosaic spread is 2.8°, which is comparable to $IrMn_3$ films grown by MBE. The films exhibit crystallographic twinning with two sets of grains, which are in-plane rotated by 60° to each other. The $L1_2$ chemical order parameter for these highly textured $IrMn_3$ films is determined to be 0.45. These highly textured films of $IrMn_3$ exhibit the crystallographic and chemical ordering required for observation of anomalous Hall effect in this non-collinear antiferromagnet.

Bibliography

[5] Wh Meiklejohn and Cp Bean. "New Magnetic Anisotropy". In: *Phys. Rev.* 105.3 (1957), pp. 904–913. ISSN: 0031-899X. URL: http://prola.aps.org/abstract/PR/v105/i3/p904{_}1{\%}5Cnhttp://link.aps.org/doi/10.1103/PhysRev.105.904.

[49] J Nogués and Ivan K Schuller. "Exchange bias". In: *J. Magn. Magn. Mater.* 192.2 (1999), pp. 203–232. ISSN: 03048853.

[50] A.E. Berkowitz and Kentaro Takano. "Exchange anisotropy a review". In: *J. Magn. Magn. Mater.* 200.1-3 (1999), pp. 552–570. ISSN: 03048853. URL: http://www.sciencedirect.com/science/article/pii/S0304885399004539.

[51] Miguel Kiwi. "Exchange bias theory". In: *J. Magn. Magn. Mater.* 234.3 (2001), pp. 584–595. ISSN: 03048853. arXiv: 0107097v1 [cond-mat].

[52] J. Nogués et al. "Exchange bias in nanostructures". In: *Phys. Rep.* 422.3 (2005), pp. 65–117. ISSN: 03701573. URL: http://linkinghub.elsevier.com/retrieve/pii/S0370157305003303.

[53] A. H. MacDonald and M. Tsoi. "Antiferromagnetic metal spintronics". In: *Philos. Trans. R. Soc. A Math. Phys. Eng. Sci.* 369.1948 (2011), pp. 3098–3114. ISSN: 1364-503X. URL: http://rsta.royalsocietypublishing.org/cgi/doi/10.1098/rsta.2011.0014.

[54] B. G. Park et al. "A spin-valve-like magnetoresistance of an antiferromagnet-based tunnel junction". In: *Nat. Mater.* 10.5 (2011), pp. 347–351. ISSN: 1476-1122. URL: http://www.nature.com/doifinder/10.1038/nmat2983.

[55] X. Marti et al. "Room-temperature antiferromagnetic memory resistor". In: *Nat. Mater.* 13.4 (2014), pp. 367–374. ISSN: 1476-1122. URL: http://www.nature.com/doifinder/10.1038/nmat3861.

[56] P. Merodio et al. "Penetration depth and absorption mechanisms of spin currents in Ir20Mn80 and Fe50Mn50 polycrystalline films by ferromagnetic resonance and spin pumping". In: *Appl. Phys. Lett.* 104.3 (2014), p. 032406. ISSN: 0003-6951. URL: http://www.scopus.com/inward/record.url?eid=2-s2.0-84893418000{\&}partnerID=tZOtx3y1.

[57] J. H. Han et al. “Antiferromagnet-controlled spin current transport in <math> <mrow> <msub> <mi>SrMnO</mi> <mn>3</mn> </msub> <mo>/</mo> <mi>Pt</mi> </mrow> </math> hybrids”. In: *Phys. Rev. B* 90.14 (2014), p. 144431. ISSN: 1098-0121. URL: http://link.aps.org/doi/10.1103/PhysRevB.90.144431.

[58] Erlend G. Tveten, Alireza Qaiumzadeh, and Arne Brataas. “Antiferromagnetic Domain Wall Motion Induced by Spin Waves”. In: *Phys. Rev. Lett.* 112.14 (2014), p. 147204. ISSN: 0031-9007. URL: http://link.aps.org/doi/10.1103/PhysRevLett.112.147204.

[59] Tobias Kampfrath et al. “Coherent terahertz control of antiferromagnetic spin waves”. In: *Nat. Photonics* 5.1 (2011), pp. 31–34. ISSN: 1749-4885. URL: http://www.nature.com/doifinder/10.1038/nphoton.2010.259.

[60] A. B. Shick et al. “Spin-orbit coupling induced anisotropy effects in bimetallic antiferromagnets: A route towards antiferromagnetic spintronics”. In: *Phys. Rev. B* 81.21 (2010), p. 212409. ISSN: 1098-0121. URL: http://link.aps.org/doi/10.1103/PhysRevB.81.212409.

[61] Frank Freimuth, Stefan Blügel, and Yuriy Mokrousov. “Anisotropic spin Hall effect from first principles”. In: *Phys. Rev. Lett.* 105.December (2010), pp. 1–4. ISSN: 00319007. arXiv: 1011.2714.

[62] J. B S Mendes et al. “Large inverse spin Hall effect in the antiferromagnetic metal Ir20 Mn80”. In: *Phys. Rev. B* 89.14 (2014), p. 140406. ISSN: 1550235X.

[63] Wei Zhang et al. “Spin Hall Effects in Metallic Antiferromagnets”. In: *Phys. Rev. Lett.* 113.19 (2014), p. 196602. ISSN: 0031-9007. URL: http://link.aps.org/doi/10.1103/PhysRevLett.113.196602.

[64] X Zhou et al. “Mapping motion of antiferromagnetic interfacial uncompensated magnetic moment in exchange-biased bilayers”. In: 3 (2015), pp. 1–5.

[65] Tobias Kosub et al. “All-Electric Access to the Magnetic-Field-Invariant Magnetization of Antiferromagnets”. In: *Phys. Rev. Lett.* 115.9 (2015), p. 097201. ISSN: 0031-9007. URL: http://link.aps.org/doi/10.1103/PhysRevLett.115.097201.

[66] Christoph Sürgers et al. “Large topological Hall effect in the non-collinear phase of an antiferromagnet”. In: *Nat. Commun.* 5 (2014), p. 3400. ISSN: 2041-1723. URL: http://www.nature.com/doifinder/10.1038/ncomms4400.

[67] Hua Chen, Qian Niu, and a. H. Macdonald. “Anomalous hall effect arising from noncollinear antiferromagnetism”. In: *Phys. Rev. Lett.* 112.1 (2014), p. 017205. ISSN: 00319007. arXiv: 1309.4041.

[68] R Shindou and N Nagaosa. “Orbital ferromagnetism and anomalous Hall effect in antiferromagnets on the distorted fcc lattice.” In: *Phys. Rev. Lett.* 87.c (2001), p. 116801. ISSN: 0031-9007. arXiv: 0108322 [cond-mat].

[69] Naoto Nagaosa et al. “Anomalous Hall effect”. In: *Rev. Mod. Phys.* 82.2 (2010), pp. 1539–1592. ISSN: 0034-6861. URL: http://link.aps.org/doi/10.1103/RevModPhys.82.1539.

[70] Takashi Yamaoka. *Antiferromagnetism in gamma-phase Mn-Ir alloys*. 1974.

[71] Ken Ichi Imakita, Masakiyo Tsunoda, and Migaku Takahashi. "Thickness dependence of exchange anisotropy of polycrystalline Mn3Ir/Co-Fe bilayers". In: *J. Appl. Phys.* 97.10 (2005), pp. 95–98. ISSN: 00218979.

[72] L. Szunyogh et al. "Giant magnetic anisotropy of the bulk antiferromagnets IrMn and <math display="inline"> <mrow> <msub> <mrow> <mtext>IrMn</mtext> </mrow> <mn>3</mn> </msub> </mrow> </math> from first principles". In: *Phys. Rev. B* 79.2 (2009), p. 020403. ISSN: 1098-0121. URL: http://link.aps.org/doi/10.1103/PhysRevB.79.020403.

[73] Chih-Hao Lee et al. "The Exchange Bias of a Permalloy and Ordered Epitaxial IrMn Thin Film Prepared From the Growth of Ultrathin [Ir/Mn] Multilayer". In: *Ieee Trans. Magn.* 47.10 (2011), pp. 3497–3500.

[74] a Kohn et al. "The antiferromagnetic structures of IrMn3 and their influence on exchange-bias." In: *Sci. Rep.* 3 (2013), p. 2412. ISSN: 2045-2322. URL: http://www.pubmedcentral.nih.gov/articlerender.fcgi?artid=3740276{\&}tool=pmcentrez{\&}rendertype=abstract.

[75] Satoru Nakatsuji, Naoki Kiyohara, and Tomoya Higo. "Letter". In: *Nature* 527.7577 (2015), pp. 212–215. ISSN: 0028-0836. URL: http://dx.doi.org/10.1038/nature15723.

[76] Ajaya K Nayak et al. "Large anomalous Hall effect driven by a nonvanishing Berry curvature in the noncolinear antiferromagnet Mn 3 Ge". In: April (2016), pp. 1–6.

[77] S. Mahajan et al. "Formation of annealing twins in f.c.c. crystals". In: *Acta Mater.* 45.6 (1997), pp. 2633–2638.

Chapter 7

Giant resonant nonlinear damping in nanoscale ferromagnets

The contents of this chapter are adapted from a collaborative work of I. Barsukov, H. K. Lee, A. A. Jara, Y.-J. Chen, A. M. Gonçalves, C. Sha, J. A. Katine, R. E. Arias, B. A. Ivanov, and I. N. Krivorotov

7.1 Introduction

Nonlinear interactions among spin wave eigenmodes of a ferromagnet give rise to a number of spectacular magneto-dynamic phenomena such as Suhl instability of the uniform precession of magnetization [78, 79], spin wave self-focusing [80] and magnetic soliton formation [81–83]. In bulk ferromagnets, nonlinear interactions generally couple each spin wave eigenmode to a continuum of other modes via energy- and momentum-conserving multi-magnon scattering [78]. This kinematically allowed scattering limits the amplitude of spin wave modes achievable in bulk ferromagnets to relatively small values. In nanoscale ferromagnets,

geometric confinement discretizes the spin wave spectrum and thereby generally eliminates the kinematically allowed multi-magnon scattering. This suppression of nonlinear scattering enables persistent excitation of spin waves with very large amplitudes [84] as observed in nanomagnet-based spin torque oscillators [85, 86]. However, tunability of the spin wave spectrum by external magnetic field can lead to restoration of the energy-conserving scattering at particular (resonant) field values [87].

Here we show that the effect of multi-magnon scattering on magnetization dynamics in nanomagnets is qualitatively different from that in bulk ferromagnets and requires a new theoretical framework for its description. Our measurements reveal that the spectral lineshape of a spin wave resonance undergoing three-magnon scattering can exhibit a minimum at the resonance frequency in sharp contrast to the amplitude maximum seen in the linear resonance regime. This unusual behavior is observed because the nonlinear damping parameter of a spin wave ceases to be frequency-independent and itself becomes a resonant function of the oscillation frequency.

We also demonstrate that such resonant nonlinear damping dramatically alters the response of a nanomagnet to spin torque. Spin torque arising from injection of spin currents polarized opposite to the direction of magnetization acts as negative damping [85]. We find, however, that such currents can also increase the damping of a spin wave mode undergoing nonlinear resonant scattering. This counterintuitive behavior is expected to have significant impact on the operation of spin torque based memory [88], oscillators [85, 89–93] and microwave detectors [94–96].

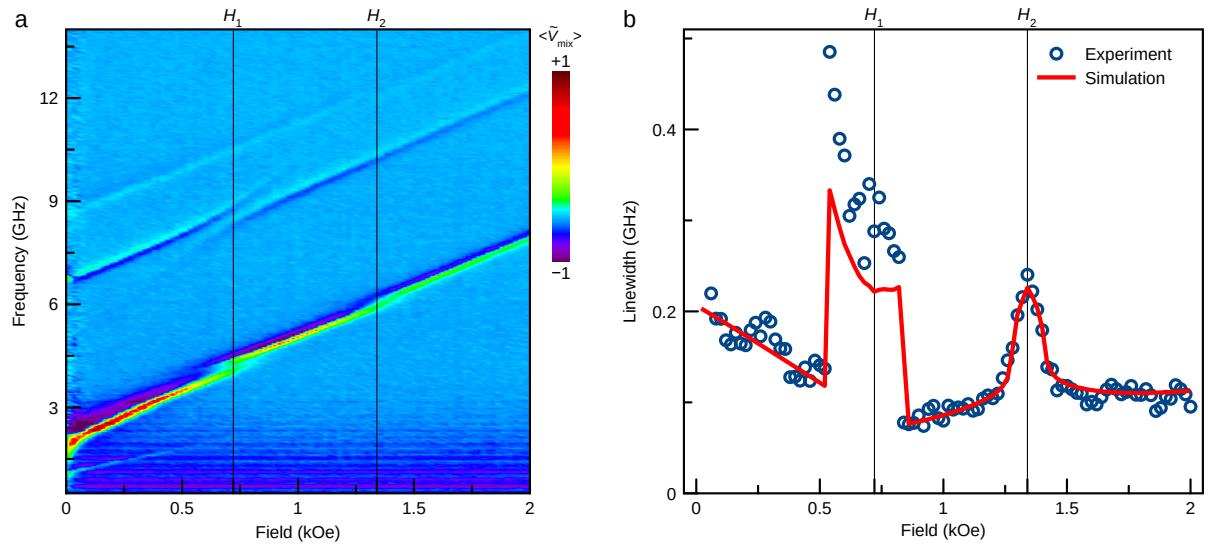

Figure 7.1: **Spin wave spectra in a nanoscale MTJ. a** Normalized ST-FMR spectra $\langle \tilde{V}_{\mathrm{mix}}(f) \rangle$ of spin wave eigenmodes in a perpendicular MTJ device (Sample 1) measured as a function of out-of-plane magnetic field. Resonance peaks arising from three low frequency modes of the MTJ free layer $|0\rangle$, $|1\rangle$, and $|2\rangle$ are observed. **b** Spectral linewidth of the quasi-uniform $|0\rangle$ spin wave mode as a function of out-of-plane magnetic field. Strong linewidth enhancement is observed in the resonant three-magnon regime at H_1 and H_2.

7.2 Results

7.2.1 Spin wave spectroscopy

We study nonlinear spin wave dynamics in nanoscale elliptical magnetic tunnel junctions (MTJs) that consist of a CoFeB free layer (FL), an MgO tunnel barrier, and a synthetic antiferromagnet (SAF) pinned layer [97]. Spectral properties of the FL spin wave modes are studied in a variety of MTJs with both in-plane and perpendicular-to-plane equilibrium orientations of the FL and SAF magnetization. We observe strong resonant nonlinear damping in both the in-plane and the perpendicular MTJs, which points to the universality of the effect.

We employ spin torque ferromagnetic resonance (ST-FMR) to measure magnetic damping of the FL spin wave modes. In this technique, a microwave drive current $I_{\mathrm{ac}} \sin(2\pi f t)$ applied

to the MTJ excites oscillations of magnetization at the drive frequency f. The resulting magnetoresistance oscillations $R_{\mathrm{ac}}\sin(2\pi ft+\phi)$ generate a direct voltage V_{mix}. Peaks in ST-FMR spectra $V_{\mathrm{mix}}(f)$ arise from resonant excitation of spin wave eigenmodes of the MTJ [98–104]. To improve signal-to-noise ratio, the magnitude of external magnetic field H applied parallel to the free layer magnetization is modulated, and a field-derivative signal $\tilde{V}_{\mathrm{mix}}(f)=\mathrm{d}V_{\mathrm{mix}}(f)/\mathrm{d}H$ is measured via lock-in detection technique [97]. $V_{\mathrm{mix}}(f)$ can then be obtained via numerical integration (Methods).

Figure 7.1a shows ST-FMR spectra $\tilde{V}_{\mathrm{mix}}(f)$ measured as a function of out-of-plane magnetic field H for an elliptical $52\,\mathrm{nm}\times 62\,\mathrm{nm}$ perpendicular MTJ device (Sample 1). Three spin wave eigenmodes with nearly linear frequency-field relation $f_n(H)$ are clearly visible in the spectra. Micromagnetic simulations (see Sec.7.4.3) reveal that these modes are three lowest frequency spin wave eigenmodes of the FL, Fig. 7.6. The lowest frequency (quasi-uniform) mode $|0\rangle$ is nodeless and has spatially uniform phase. Each of the two higher-order modes $|n\rangle$ $(n=1,2)$ has a single node at the FL center that is either perpendicular $(n=1)$ or parallel $(n=2)$ to the ellipse long axis.

The spectral linewidth of the resonances in Fig. 7.1a can be used for evaluation of the mode damping. The quasi-uniform mode $|0\rangle$ resonance visibly broadens at two magnetic field values: $H_1=0.74\,\mathrm{kOe}$ (4 GHz) and $H_2=1.34\,\mathrm{kOe}$ (6 GHz). Near H_1, the mode $|1\rangle$ resonance also broadens and exhibits splitting, same behavior is observed for the mode $|2\rangle$ at H_2. At these fields, the higher-order mode frequency is twice that of the quasi-uniform mode $f_n=2f_0$. This shows that three-magnon confluence [87, 105–108] is the mechanism of the quasi-uniform mode damping increase: two magnons of the quasi-uniform mode $|0\rangle$ merge into a single magnon of the higher-order mode $|n\rangle$.

The most striking feature of the quasi-uniform mode resonance near H_1 is its split-peak shape with a local minimum at the resonance frequency. Such a lineshape cannot be fit by the standard Lorentzian curve with symmetric and antisymmetric components [97]. We therefore

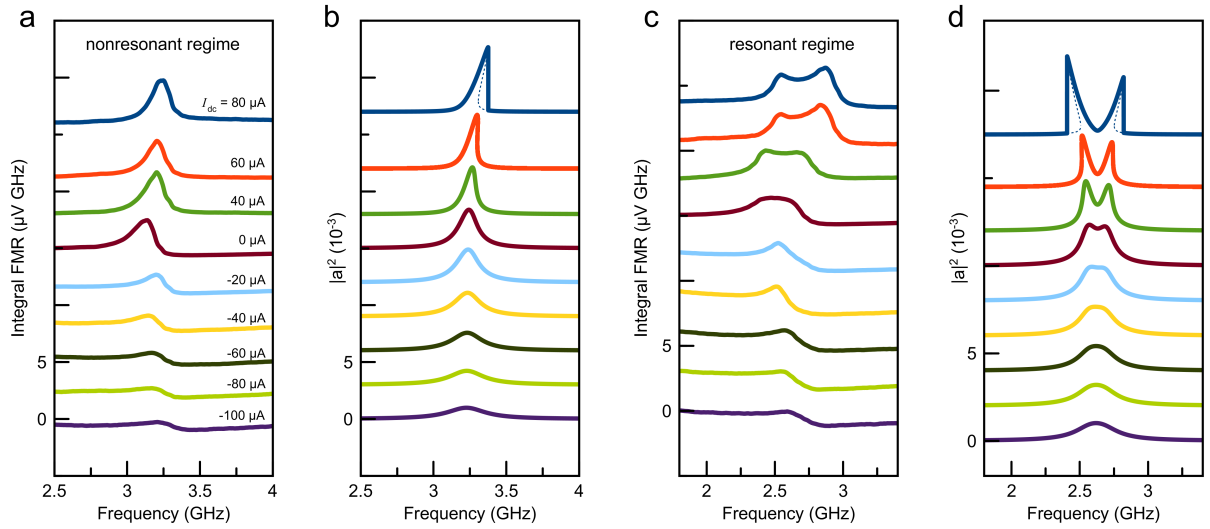

Figure 7.2: **Effect of spin torque on spin wave resonance lineshape. a, b** Spin wave resonance lineshapes in the nonresonant regime at $H > H_1$ for different values of direct bias current I_{dc}. **c, d** Spin wave resonance lineshapes in the resonant three-magnon regime at $H = H_1$. **a, c** Measured ST-FMR spectra (Sample 2). **b, d** Solutions of Eqs. (3) and (4). Identical bias current values I_{dc} (displayed in **a**) are used in **a-d**.

use a double-peak fitting function (described in Methods) to quantify the effective linewidth Δf_0 of the resonance profile. For applied fields sufficiently far from H_1, the ST-FMR curve recovers its single-peak shape and Δf_0 is determined as half width of the standard Lorentzian fitting function [97]. Figure 7.1b shows Δf_0 as a function of H and demonstrates a large increase of the linewidth near the fields of the resonant three-magnon regime H_1 and H_2. The stepwise increase of Δf_0 near H_1 is a result of the ST-FMR curve transition between the split-peak and single-peak shapes. For fields near H_2, the resonance profile broadens but does not develop a visible split-peak lineshape. As a result, $\Delta f_0(H)$ is a smooth function in the vicinity of H_2.

7.2.2 Effect of spin torque

In MTJs, direct bias current I_{dc} applied across the junction exerts spin torque on the FL magnetization, acting as antidamping for $I_{dc} > 0$ and as positive damping for $I_{dc} < 0$ [99,

109]. The antidamping spin torque increases the amplitude of the FL spin wave modes [99, 110] and decreases their spectral linewidth [111]. We can employ spin torque from I_{dc} to control the amplitude of spin wave eigenmodes excited in ST-FMR measurements, and thereby study the crossover between linear and nonlinear regimes of spin wave resonance.

Figure 7.2 shows the dependence of ST-FMR resonance curve of the $|0\rangle$ mode $V_{\mathrm{mix}}(f)$ on I_{dc} for a 50 nm $\times$ 110 nm elliptical in-plane MTJ (Sample 2). For in-plane magnetic field values far from the three-magnon resonance fields H_n, the amplitude of ST-FMR resonance curve $V_{\mathrm{mix}}(f)$ shown in Fig. 7.2a monotonically increases with increasing antidamping spin torque, as expected. At $H = H_1$, the antidamping spin torque has a radically different and rather surprising effect on the resonance curve. As illustrated in Fig. 7.2c, increasing antidamping spin torque first broadens the resonance at $H = H_1$ and then transforms a single-peak resonance lineshape into a split-peak lineshape with a local minimum at the resonance frequency f_0. The data in Fig. 7.2 demonstrate that the unusual split-peak lineshape of the resonance is only observed when (i) the three-magnon scattering of the quasi-uniform mode is allowed by the conservation of energy and (ii) the amplitude of the mode is sufficiently high, confirming that the observed effect is resonant and nonlinear in nature.

Fig. 7.2c reveals that antidamping spin torque can increase the spectral linewidth and the effective damping of the quasi-uniform spin mode if the mode undergoes resonant three-magnon scattering. Figure 7.3 further illustrates this counterintuitive effect. It shows the linewidth of the quasi-uniform mode of a 50 nm $\times$110 nm elliptical in-plane MTJ (Sample 3) measured as a function of bias current. In Fig. 7.3, blue symbols show the linewidth measured at an in-plane magnetic field sufficiently far from the three-magnon resonance fields H_n. At this field, the expected quasi-linear dependence of the linewidth on I_{dc} is observed for currents well below the critical current for the excitation of auto-oscillatory magnetic dynamics. Near the critical current, the linewidth increases due to a combination of the fold-over effect [112–114] and thermally activated switching between the large- and small-amplitude oscillatory

states of the fold-over regime [99]. The red symbols in Fig. 7.3 show the linewidth measured in the resonant three-magnon regime at $H = H_1$. In contrast to the nonresonant regime, the linewidth increases with increasing $|I_{\rm dc}|$ for both current polarities. Furthermore, the maximum linewidth is measured for the antidamping current polarity.

7.2.3 Theoretical model

Nonlinear interactions among spin waves in a bulk ferromagnet with a continuous spin wave spectrum can lead to broadening of the spin wave resonance [78, 115–117]. For example, three- and four-magnon scattering of the uniform mode into a continuum of degenerate spin wave eigenmodes gives rise to nonlinear enhancement of the uniform mode damping. However, these processes lead to a simple line broadening and cannot explain the observed split-peak lineshape of the resonance. The description of nonlinear spin wave resonance in the nanoscale ferromagnet geometry therefore requires a new theoretical framework. To derive the theory of resonant nonlinear damping in a nanomagnet, we start with a model Hamiltonian that explicitly takes into account resonant nonlinear scattering between the quasi-uniform mode and a higher-order spin wave mode (in reduced units with $\hbar \equiv 1$):

$$\begin{aligned}\mathcal{H} = \omega_0 a^\dagger a + \omega_n b^\dagger b + \frac{\Psi_0}{2} a^\dagger a^\dagger a a + \frac{\Psi_n}{2} b^\dagger b^\dagger b b \\ +(\psi_n a a b^\dagger + \psi_n^* a^\dagger a^\dagger b) \\ +\zeta \left\{ \exp(-i\,\omega t) a^\dagger + \exp(i\,\omega t) a \right\}\end{aligned} \tag{7.1}$$

where $a^\dagger$, a and $b^\dagger$, b are the magnon creation and annihilation operators for the quasi-uniform mode $|0\rangle$ with frequency ω_0 and for the higher-order spin wave mode $|n\rangle$ mode with frequency ω_n, respectively. The nonlinear mode coupling term proportional to the coupling strength parameter ψ_n describes the annihilation of two $|0\rangle$ magnons and creation of one

$|n\rangle$ magnon, as well as the inverse process. The Hamiltonian is written in the resonant approximation, where small nonresonant terms such as aab, $aaa^\dagger$ are neglected. The terms proportional to Ψ_0 and Ψ_n describe the intrinsic nonlinear frequency shifts [118] of the modes $|0\rangle$ and $|n\rangle$. The last term describes the excitation of the quasi-uniform mode by an external ac drive with the amplitude ζ and frequency ω.

We further define classically a dissipation function $\mathcal{Q}$, where α_0 and α_n are the intrinsic linear damping parameters of the modes $|0\rangle$ and $|n\rangle$ [119–121]:

$$\mathcal{Q} = \frac{\mathrm{d}a^\dagger}{\mathrm{d}t}\frac{\mathrm{d}a}{\mathrm{d}t}(\alpha_0 + \eta_0 a^\dagger a) + \frac{\mathrm{d}b^\dagger}{\mathrm{d}t}\frac{\mathrm{d}b}{\mathrm{d}t}(\alpha_n + \eta_n b^\dagger b) \tag{7.2}$$

For generality, Eq. (2) includes intrinsic nonlinear damping [122] of the modes $|0\rangle$ and $|n\rangle$ described by the nonlinearity parameters η_0 and η_n. However, our analysis below shows that the split-peak resonance lineshape is predicted by our theory even if η_0 and η_n are set equal to zero.

Equations describing the nonlinear dynamics of the two coupled spin wave modes of the system follow from Eq. (1) and Eq. (2):

$$i\frac{\mathrm{d}a}{\mathrm{d}t} = \frac{\partial\mathcal{H}}{\partial a^\dagger} + \frac{\partial\mathcal{Q}}{\partial(\mathrm{d}a^\dagger/\mathrm{d}t)} \tag{7.3}$$

$$i\frac{\mathrm{d}b}{\mathrm{d}t} = \frac{\partial\mathcal{H}}{\partial b^\dagger} + \frac{\partial\mathcal{Q}}{\partial(\mathrm{d}b^\dagger/\mathrm{d}t)} \tag{7.4}$$

In the Sec.7.4.1, we show that these equations have a periodic solution $a = \bar{a}\exp(-i\,\omega t)$ and $b = \bar{b}\exp(-i\,2\omega t)$, where $\bar{a}$, $\bar{b}$ are the complex spin wave mode amplitudes. For such periodic solution, Eqs. (3) and (4) are reduced to a set of two nonlinear algebraic equations for absolute

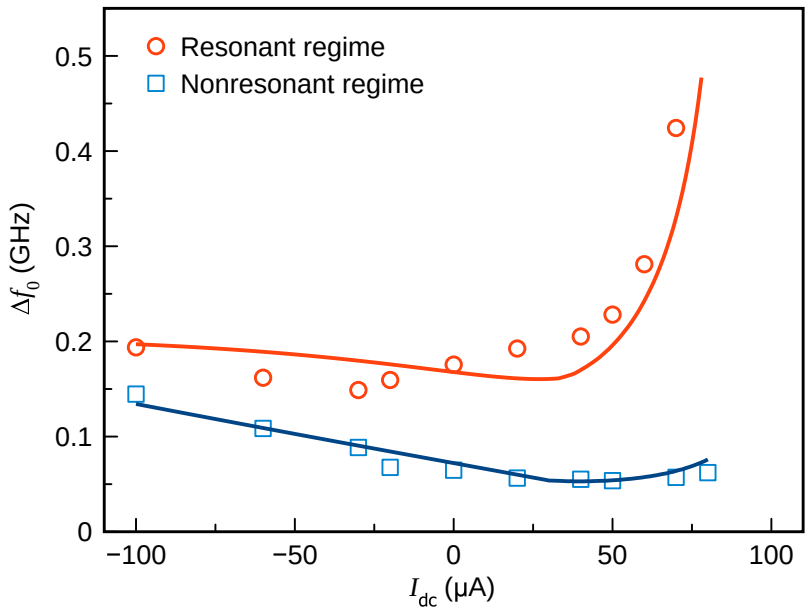

Figure 7.3: **Effect of spin torque on linewidth.** Linewidth of the quasi-uniform spin wave mode as a function of the applied direct bias current (Sample 3): blue symbols – in the nonresonant regime $H \neq H_1$ and red symbols – in the resonant three-magnon regime $H = H_1$. Lines are numerical fits using Eqs. (3) and (4).

values of the spin wave mode amplitudes $|\bar{a}|$ and $|\bar{b}|$, which can be solved numerically. Since the ST-FMR signal is proportional to $|\bar{a}|^2$ (Methods), the calculated $|\bar{a}|^2(\omega)$ function can be directly compared to the measured ST-FMR resonance lineshape.

We employ the solution of Eqs. (3) and (4) to fit the field dependence of the quasi-uniform mode linewidth in Fig. 7.1b. In this fitting procedure, the resonance lineshape $|\bar{a}|^2(\omega)$ is calculated, and its spectral linewidth $\Delta\omega_0$ is found numerically. The resonance frequencies ω_0 and ω_n are directly determined from the ST-FMR data in Fig. 7.1a. The intrinsic damping parameters α_0 and α_n near H_1 and H_2 are found from linear interpolations of the ST-FMR linewidths Δf_0 and Δf_n measured at fields far from H_1 and H_2. We find that $\Delta\omega_0$ weakly depends on the nonlinearity parameters Ψ and η, and thus these parameters are set to zero (see Sec.7.2.4 and Fig. 7.4). We also find that the calculated linewidth $\Delta\omega_0$ depends on the product of the drive amplitude ζ and mode coupling strength ψ_n, but is nearly insensitive to the individual values of ζ and ψ_n as long as $\zeta \cdot \psi_n = \text{const}$ (Fig.7.5 and Sec.7.2.4). Therefore,

we use $\zeta \cdot \psi_n$ as a single fitting parameter in this fitting procedure. Solid line in Fig. 7.1b shows the calculated field dependence of the quasi-uniform mode linewidth on magnetic field. The agreement of this single-parameter fit with the experiment is excellent.

Figures 7.2b and 7.2d illustrate that Eqs. (3) and (4) not only describe the field dependence of ST-FMR linewidth but also qualitatively reproduce the spectral lineshapes of the measured ST-FMR resonances as well as the effect of the antidamping spin torque on the lineshapes. Fig. 2b shows the dependence of the calculated lineshape $|\bar{a}|^2(\omega)$ on antidamping spin torque for a magnetic field H far from the three-magnon resonance fields H_n. At this nonresonant field, increasing antidamping spin torque induces the fold-over of the resonance curve [112] without resonance peak splitting. The dependence of $|\bar{a}|^2(\omega)$ on antidamping spin torque for $H = H_1$ is shown in Fig. 7.2d. At this field, the resonance peak in $|\bar{a}|^2(\omega)$ first broadens with increasing antidamping spin torque and then splits, in qualitative agreement with the experimental ST-FMR data in Fig. 2c. Our calculations (Fig.7.4 and Sec.7.2.4) reveal that while the nonlinearity parameters Ψ_0, η_0, Ψ_n and η_n have little effect on the linewidth $\Delta\omega_0$, they modify the lineshape of the resonance. Given that the nonlinearity parameter values are not well known for the systems studied here, we do not attempt to quantitatively fit the measured ST-FMR lineshapes.

Equations (3) and (4) also quantitatively explain the observed dependence of the quasi-uniform mode linewidth $\Delta\omega_0$ on direct bias current $I_{\rm dc}$. Assuming antidamping spin torque linear in bias current [111, 123, 124]: $\alpha_0 \to \alpha_0(1 - I_{\rm dc}/I_{\rm c}^{|0\rangle})$, $\alpha_n \to \alpha_n(1 - I_{\rm dc}/I_{\rm c}^{|n\rangle})$, where $I_{\rm c}^{|n\rangle} > I_{\rm c}^{|0\rangle}$ are the critical currents, we fit the measured bias dependence of ST-FMR linewidth in Fig. 7.3 by solving Eqs. (3) and (4). The solid lines in Fig. 7.3 are the best numerical fits, where $\zeta \cdot \psi_n$ and $I_{\rm c}$ are used as independent fitting parameters. The rest of the parameters in Eqs. (3) and (4) are directly determined from the experiment following the procedure used for fitting the data in Fig. 1b. Theoretical curves in Fig. 7.3 capture the main feature of

the data at the three-magnon resonance field H_1 – increase of the linewidth with increasing antidamping spin torque.

7.2.4 Effect of the drive amplitude and intrinsic nonlinearitites on the resonance lineshape

To understand the impact of the intrinsic nonlinearity parameters (Ψ_0, Ψ_n, η_0, η_n) on the quasi-uniform spin wave mode resonance, we plot the numerical solution of Eq. (7.30) in Fig.7.4. Each panel of this figure shows a reference lineshape of the resonance calculated with all intrinsic nonlinearity parameters set to zero (red curve) and a lineshape calculated with one of the intrinsic nonlinearity parameter different from zero (blue curve). This figure reveals that increasing η_0 decreases the mode amplitude and slightly increases the linewidth. Increasing η_n decreases the degree of the double-peak lineshape splitting. Increasing Ψ_n increases the lineshape asymmetry. Increasing Ψ_0 increases lineshape asymmetry and induces fold-over.

Figure 7.5 shows the linewidth as a function of the drive amplitude for three scenarios, where the intrinsic nonlinearities Ψ_0, Ψ_n, η_0, η_n are set to zero for simplicity. If the coupling parameter is zero, $\psi_n = 0$, the linewidth does not depend on the drive amplitude, as expected for a single-mode linear oscillator. The second case demonstrates that the linewidth remains constant when the product $\psi_n \cdot \zeta$ is constant. For a constant non-zero coupling parameter, the linewidth shows an increase with the drive amplitude. This observation allows us to employ a single fitting parameter ($\psi_n \cdot \zeta$) to fit the data in Fig. 7.1b. This conjecture can be confirmed analytically by introducing a normalized spin wave amplitude $\hat{a} = \psi_n \bar{a}$, which

allows us to rewrite Eq. (7.30) omitting all intrinsic nonlinearities into the following form:

$$\omega\left[1+i\alpha_0+i\frac{4\alpha_n|\hat{a}|^2}{(2\omega-\omega_n)^2+4\alpha_n^2\omega^2}\right]\hat{a}-\omega_0\hat{a}-\frac{2(2\omega-\omega_n)}{(2\omega-\omega_n)^2+4\alpha_n^2\omega^2}|\hat{a}|^2\hat{a}=\psi_n\zeta \qquad (7.5)$$

This equation describes an effective single-mode nonlinear oscillator with renormalized excitation amplitude $\psi_n\zeta$.

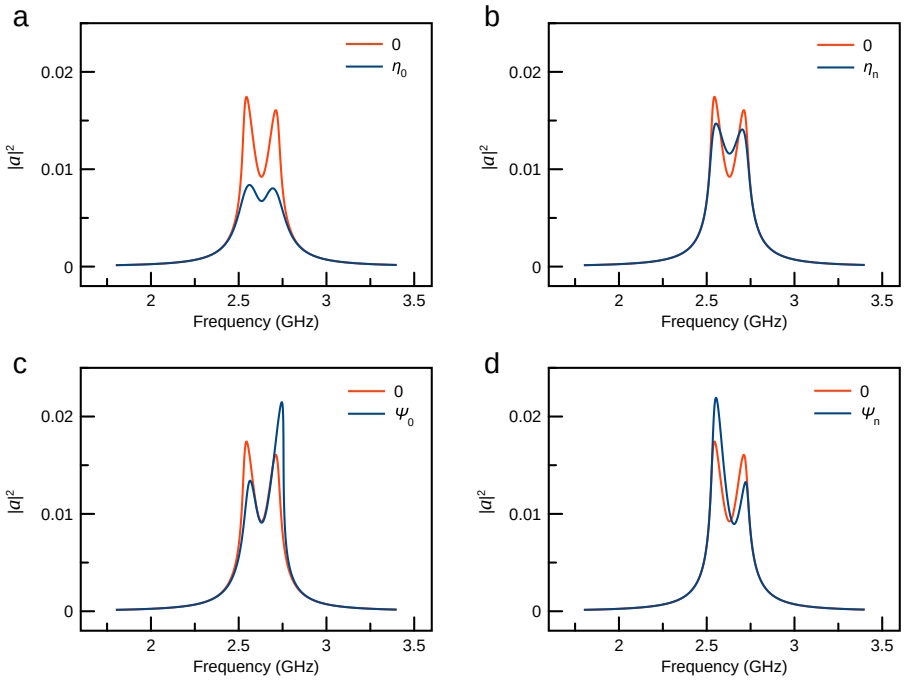

Figure 7.4: **Effect of intrinsic nonlinearities on the quasi-uniform spin wave resonance lineshape.** Spectral lineshape of the quasi-uniform spin wave mode resonance $|\bar{a}|^2(\omega)$ at the three-magnon resonance condition $2\omega_0=\omega_n$ calculated by numerically solving Eq. (7.30). The red curve is a reference lineshape calculated with all intrinsic nonlinearity parameters $(\eta_0,\eta_n,\Psi_0,\Psi_n)$ set to zero. The blue lineshape in each panel is calculated with one of the intrinsic nonlinearity parameters set to a non-zero value: **a** $\eta_0=1.325\cdot10^{-24}\,\mathrm{J}$, **b** $\eta_n=3.313\cdot10^{-24}\,\mathrm{J}$, **c** $\Psi_0=1.325\cdot10^{-24}\,\mathrm{J}$, **d** $\Psi_n=1.325\cdot10^{-23}\,\mathrm{J}$. Other parameters employed in the calculation are: $\omega_0=2\pi\cdot2.63\,\mathrm{GHz}$, $\omega_n=2\pi\cdot5.26\,\mathrm{GHz}$; $\alpha_0=0.02662$, $\alpha_n=0.03042$ at $I_{\mathrm{dc}}=0$; $\psi_n\cdot\zeta=h^2\cdot0.006\,\mathrm{GHz}^2$, where h is the Planck constant.

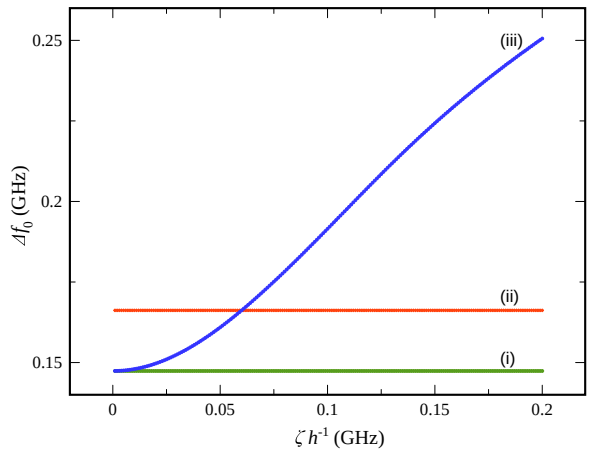

Figure 7.5: **Effect of the drive amplitude on linewidth in the resonant three-magnon regime.** Calculated linewidth of the quasi-uniform spin wave mode as a function of the drive amplitude ζ for different values of the mode coupling parameter ψ_n. (i) Green: $\psi_n = 0$, (ii) red: variable ψ_n with a constraint $\psi_n \cdot \zeta = h^2 \cdot 0.006\,\mathrm{GHz}^2$, and (iii) blue: $\psi_n = h \cdot 0.1\,\mathrm{GHz}$. All intrinsic nonlinearity parameters: Ψ_0, Ψ_n, η_0 and η_n are set to zero. h is the Planck constant. Other parameters employed in the calculation are: $\omega_0 = 2\pi \cdot 2.63\,\mathrm{GHz}$, $\omega_n = 2\pi \cdot 5.26\,\mathrm{GHz}$; $\alpha_0 = 0.02662$ and $\alpha_n = 0.03042$ at $I_{\mathrm{dc}} = 0$.

7.2.5 Effective single-mode nonlinear oscillator approximation

If we neglect intrinsic nonlinearities Ψ_n and η_n of the higher order spin wave mode, Eq. (7.30) can be reduced to a cubic equation for $\bar{a}$ and solved analytically. This approximation allows us to obtain several important qualitative insights into the properties of the resonant nonlinear damping of the quasi-uniform mode. By setting $\Psi_n = 0$ and $\eta_n = 0$ in Eq. (7.20), we obtain an exact solution for $\bar{b}$:

$$\bar{b} = \frac{\psi_n^* \bar{a}^2}{2\omega(1 + i\alpha_n) - \omega_n} \tag{7.6}$$

Using this result, we reduce Eq. (7.30) to a cubic algebraic equation for $\bar{a}$:

$$\omega\left[1+i(\alpha_0+\eta_0|\bar{a}|^2)+i\frac{4|\psi_n|^2\alpha_n|\bar{a}|^2}{(2\omega-\omega_n)^2+4\alpha_n^2\omega^2}\right]\bar{a} \\ -\omega_0\bar{a}-\left[\Psi_0+\frac{2|\psi_n|^2(2\omega-\omega_n)}{(2\omega-\omega_n)^2+4\alpha_n^2\omega^2}\right]|\bar{a}|^2\bar{a}=\zeta \tag{7.7}$$

This equation describes the amplitude $\bar{a}$ of an effective single-mode nonlinear oscillator.

It is evident from Eq. (7.8) that the frequency of the quasi-uniform mode experiences a nonlinear shift:

$$\omega_0^{\text{eff}}=\omega_0+\left[\Psi_0+\frac{2|\psi_n|^2(2\omega-\omega_n)}{(2\omega-\omega_n)^2+4\alpha_n^2\omega^2}\right]|\bar{a}|^2 \tag{7.8}$$

The nonlinear frequency shift has a well-pronounced antisymmetric resonant character near the resonance frequency $\omega_n/2$, that arises from the resonant three-magnon scattering.

Further, it is clear from Eq. (7.8) that the effective damping of the quasi-uniform mode also acquires a term arising from the three-magnon interaction:

$$\alpha_0^{\text{eff}}=\alpha_0+\left[\eta_0+\frac{4|\psi_n|^2\alpha_n}{(2\omega-\omega_n)^2+4\alpha_n^2\omega^2}\right]|\bar{a}|^2 \tag{7.9}$$

The last term describes a resonant enhancement of the nonlinear damping by three-magnon scattering near the resonance frequency $\omega_n/2$. Strikingly, the magnitude of the resonant damping enhancement at $\omega_n/2$ increases when the intrinsic damping of the higher order

mode α_n decreases. In the limit $\alpha_n \to 0$, the effective damping becomes

$$\alpha_0^{\text{eff}} \to \alpha_0 + \left[\eta_0 + \frac{2\pi|\psi_n|^2}{\omega}\delta(2\omega - \omega_n)\right]|\bar{a}|^2 \tag{7.10}$$

where δ is Dirac's delta function. Equation (7.9) suggests that the effective damping of the quasi-uniform mode α_0^{eff} can increase with increasing antidamping spin torque applied to the nanomagnet. Indeed, the antidamping spin torque tends to increase the amplitude [99] of the quasi-uniform mode $|\bar{a}|$ and decrease the intrinsic damping parameter of the higher order mode $\alpha_n \to \alpha_n(1 - I_{\text{dc}}/I_{\text{c}}^{|n\rangle})$, both enhancing the nonlinear damping term in Eq. (7.8). For a sufficiently large mode coupling parameter ψ_n, the enhancement of the nonlinear damping term by the antidamping spin torque can exceed the reduction of the linear damping parameter $\alpha_0 \to \alpha_0(1 - I_{\text{dc}}/I_{\text{c}}^{|0\rangle})$ by the torque, leading to an increase of α_0^{eff} by $I_{\text{dc}} > 0$ and broadening of the quasi-uniform mode resonance by the antidamping spin torque. This scenario is indeed realized in the MTJ devices studied here as demonstrated by the data and calculations in Fig. 7.3.

7.3 Discussion

Further insight into the mechanisms of the nonlinear spin wave resonance peak splitting and broadening by antidamping spin torque can be gained by neglecting the intrinsic nonlinearities Ψ_n and η_n of the higher-order mode $|n\rangle$. Setting $\Psi_n = 0$ and $\eta_n = 0$ in Eqs. (3) and (4) allows us to reduce the equation of motion for the quasi-uniform mode amplitude $|\bar{a}|$ to the standard equation for a single-mode damped driven oscillator (see Sec.7.2.5) where a constant damping parameter α_0 is replaced by an effective frequency-dependent nonlinear

damping parameter α_0^{eff}:

$$\alpha_0^{\text{eff}} = \alpha_0 + \left[\eta_0 + \frac{4\alpha_n\psi_n^2}{(2\omega-\omega_n)^2 + 4\alpha_n^2\omega^2}\right]|\bar{a}|^2 \tag{7.11}$$

and the resonance frequency is replaced by an effective resonance frequency:

$$\omega_0^{\text{eff}} = \omega_0 + \left[\Psi_0 + \frac{2|\psi_n|^2(2\omega-\omega_n)}{(2\omega-\omega_n)^2 + 4\alpha_n^2\omega^2}\right]|\bar{a}|^2 \tag{7.12}$$

Equation (5) clearly shows that the damping parameter of the quasi-uniform mode itself becomes a resonant function of the drive frequency with a maximum at half the frequency of the higher order mode ($\omega = \frac{1}{2}\omega_n$). The amplitude and the width of this resonance in $\alpha_0^{\text{eff}}(\omega)$ are determined by the intrinsic damping parameter α_n of the higher-order mode $|n\rangle$. If α_n is sufficiently small, the quasi-uniform mode damping is strongly enhanced at $\omega = \frac{1}{2}\omega_n$, which leads to a decrease of the quasi-uniform mode amplitude at this drive frequency. If the drive frequency is shifted away from $\frac{1}{2}\omega_n$ to either higher or lower values, the damping decreases, which can result in an increase of the quasi-uniform mode amplitude $|\bar{a}|$. Therefore, the amplitude of the quasi-uniform mode $|\bar{a}|(\omega)$ can exhibit a local minimum at $\omega = \frac{1}{2}\omega_n$. Due to its nonlinear origin, the tendency to form a local minimum in $|\bar{a}|(\omega)$ at $\frac{1}{2}\omega_n$ is enhanced with increasing $|\bar{a}|$. Since $|\bar{a}|$ is large near the resonance frequency ω_0, tuning ω_0 to be equal to $\frac{1}{2}\omega_n$ greatly amplifies the effect of local minimum formation in $|\bar{a}|(\omega)$. This qualitative argument based on Equation (5) explains the data in Fig. 7.2 – the split-peak nonlinear resonance of the quasi-uniform mode is only observed when external magnetic field tunes the spin wave eigenmode frequencies to the three-magnon resonance condition $\omega_0 = \frac{1}{2}\omega_n$.

Equation (6) reveals that the nonlinear frequency shift of the quasi-uniform mode is also a resonant function of the drive frequency. In contrast to the nonlinear damping resonance described by Equation (5), the frequency shift resonance is an antisymmetric function of $\omega - \frac{1}{2}\omega_n$. The nonlinear shift is negative for $\omega < \frac{1}{2}\omega_n$ and thus causes a fold-over towards

lower frequencies while it is positive for $\omega > \frac{1}{2}\omega_n$ causing fold-over towards higher frequencies. At the center of the resonance profile, the three-magnon process induces no frequency shift. This double-sided fold-over also contributes to the formation of the split-peak lineshape of the resonance shown in Figs. 2c and 2d and to the linewidth broadening. As with the nonlinear damping resonance, the antisymmetric nonlinear frequency shift and the double-sided fold-over become greatly amplified when the spin wave mode frequencies are tuned near the three-magnon resonance $\omega_0 = \frac{1}{2}\omega_n$.

Equations (5) and (6) also shed light on the origin of the quasi-uniform mode line broadening by the antidamping spin torque. The antidamping spin torque increases the quasi-uniform mode amplitude $|\bar{a}|$ via transfer of angular momentum from spin current to the mode [125]. Since the nonlinear damping and the nonlinear frequency shift are both proportional to $|\bar{a}|^2$ and both contribute to the line broadening, the antidamping spin torque can indeed give rise to the line broadening. Equation (5) reveals two competing effects of the antidamping spin torque on the quasi-uniform mode damping parameter α_0^{eff}: spin torque from I_{dc} decreases the linear component of the damping parameter $\alpha_0 \rightarrow \alpha_0(1 - I_{\text{dc}}/I_{\text{c}}^{|0\rangle})$ and increases the nonlinear component via increased $|\bar{a}|^2$. Whether the antidamping spin torque decreases or increases the spectral linewidth of the mode depends on the system parameters. Our numerical solution of Eqs. (3) and (4) shown in Fig. 3 clearly demonstrates that the antidamping spin torque can strongly increase the linewidth of the quasi-uniform mode when the three-magnon resonance condition $\omega_0 = \frac{1}{2}\omega_n$ is satisfied. Furthermore, we find that the three-magnon process exhibits no threshold behavior upon increasing amplitude (see Fig.7.5) or decreasing intrinsic damping.

The key requirement for observation of the resonant nonlinear damping is the discreteness of the magnon spectrum imposed by geometric confinement in the nanoscale ferromagnet. The split-peak nonlinear resonance discovered in this work cannot be realized in bulk ferromagnets because the three-magnon resonance condition in bulk is not only valid at the uniform mode

frequency $\omega_0 = \frac{1}{2}\omega_n$ but instead in a broad frequency range. Owing to the magnon spectrum continuity in bulk, shifting the excitation frequency away from ω_0 does not suppress the three-magnon scattering of the uniform mode – it simply shifts it from one group of magnons to another [78, 105]. Therefore, the amplitude of the uniform mode does not increase when the drive frequency is shifted away from ω_0 and the split-peak resonance is not realized.

We expect that the resonant nonlinear damping discovered in this work will have strong impact on the performance of spin torque devices such as spin torque magnetic memory, spin torque nanooscillators and spin torque microwave detectors. Since all these devices rely on large-amplitude oscillations of magnetization driven by spin torque, the amplitude limiting resulting from the resonant nonlinear damping is expected to have detrimental effect on the device performance.

In conclusion, our measurements demonstrate that magnetic damping of spin wave modes in a nanoscale ferromagnet has a strong nonlinear component of resonant character that appears at a discrete set of magnetic fields corresponding to resonant three-magnon scattering. This strong resonant nonlinearity can give rise to unusual spin wave resonance profile with a local minimum at the resonance frequency in sharp contrast to the properties of the linear and nonlinear spin wave resonances in bulk ferromagnets. The resonant nonlinearity has a profound effect on the response of the nanomagnet to spin torque. Antidamping spin torque that reduces the quasi-uniform spin wave mode damping at magnetic fields far from the resonant three-magnon regime, can strongly enhance the damping in the resonant regime. This inversion of the effect of spin torque on magnetization dynamics by the resonant nonlinearity is expected to have significant impact on the performance of nanoscale spin torque devices such as magnetic memory and spin torque oscillators.

7.4 Methods

7.4.1 Solution of the equations of motion

The Hamiltonian equations of motion describing the coupled dissipative dynamics of the quasi-uniform (a) and the higher-order (b) spin wave modes are:

$$i\frac{\mathrm{d}a}{\mathrm{d}t} = \frac{\partial \mathcal{H}}{\partial a^\dagger} + \frac{\partial \mathcal{Q}}{\partial(\mathrm{d}a^\dagger/\mathrm{d}t)} \tag{7.13}$$

$$i\frac{\mathrm{d}b}{\mathrm{d}t} = \frac{\partial \mathcal{H}}{\partial b^\dagger} + \frac{\partial \mathcal{Q}}{\partial(\mathrm{d}b^\dagger/\mathrm{d}t)} \tag{7.14}$$

where $\mathcal{H}$ is the Hamiltonian of the system and $\mathcal{Q}$ is the dissipation function, given by:

$$\begin{aligned}\mathcal{H} &= \omega_0 a^\dagger a + \omega_n b^\dagger b + \frac{1}{2}\Psi_0 a^\dagger a^\dagger a a + \frac{1}{2}\Psi_n b^\dagger b^\dagger b b \\ &\quad + (\psi_n^* a a b^\dagger + \psi_n a^\dagger a^\dagger b) + \zeta\{\exp(-i\omega t)a^\dagger + \exp(i\omega t)a\}\end{aligned} \tag{7.15}$$

$$\mathcal{Q} = \frac{\mathrm{d}a^\dagger}{\mathrm{d}t}\frac{\mathrm{d}a}{\mathrm{d}t}(\alpha_0 + \eta_0 a^\dagger a) + \frac{\mathrm{d}b^\dagger}{\mathrm{d}t}\frac{\mathrm{d}b}{\mathrm{d}t}(\alpha_n + \eta_n b^\dagger b) \tag{7.16}$$

By using Eq. (7.15) and Eq. (7.16) in Eq. (7.13) and Eq. (7.14), the Hamiltonian equations can be written as:

$$i\frac{\mathrm{d}a}{\mathrm{d}t} - (\alpha_0 + \eta_0 a^\dagger a)\frac{\mathrm{d}a}{\mathrm{d}t} = \omega_0 a + 2\psi_n a^\dagger b + \Psi_0 a^\dagger a a + \zeta\exp(-i\omega t) \tag{7.17}$$

$$i\frac{\mathrm{d}b}{\mathrm{d}t} - (\alpha_n + \eta_n b^\dagger b)\frac{\mathrm{d}b}{\mathrm{d}t} = \omega_n b + \psi_n^* a a + \Psi_n b^\dagger b b \tag{7.18}$$

Using a periodic ansatz $a = \bar{a}\exp(-i\omega t)$ and $b = \bar{b}\exp(-2i\omega t)$ in Eq. (7.17) and Eq. (7.18), where $\bar{a}$ and $\bar{b}$ are complex amplitudes, reduces the Hamiltonian equations to a set of two algebraic equation for the complex amplitudes:

$$\left(\omega - \omega_0 - \Psi_0|\bar{a}|^2 + i(\alpha_0 + \eta_0|\bar{a}|^2)\omega\right)\bar{a} - 2\psi_n\bar{a}^*\bar{b} = \zeta \tag{7.19}$$

$$\left(2\omega - \omega_n - \Psi_n|\bar{b}|^2 + 2i(\alpha_n + \eta_n|\bar{b}|^2)\omega\right)\bar{b} = \psi_n^*\bar{a}^2 \tag{7.20}$$

We solve Eq. (7.20) for $\bar{b}$ and multiply the numerator and denominator of this expression by the complex conjugate of the denominator:

$$\bar{b} = \psi_n^*\bar{a}^2\frac{\left(2\omega - \omega_n - \Psi_n|\bar{b}|^2\right) - i2(\alpha_n + \eta_n|\bar{b}|^2)\omega}{\left(2\omega - \omega_n - \Psi_n|\bar{b}|^2\right)^2 + 4(\alpha_n + \eta_n|\bar{b}|^2)^2\omega^2} \tag{7.21}$$

then we multiply Eq. (7.21) by $\frac{2\psi_n\bar{a}^*}{\bar{a}}$ and evaluate the real and imaginary parts.

$$\Re\left[\frac{2\psi_n\bar{a}^*\bar{b}}{\bar{a}}\right] = |\psi_n|^2|\bar{a}|^2\frac{2\left(2\omega - \omega_n - \Psi_n|\bar{b}|^2\right)}{\left(2\omega - \omega_n - \Psi_n|\bar{b}|^2\right)^2 + 4(\alpha_n + \eta_n|\bar{b}|^2)^2\omega^2} \tag{7.22}$$

$$\Im\left[\frac{2\psi_n\bar{a}^*\bar{b}}{\bar{a}}\right] = |\psi_n|^2|\bar{a}|^2\frac{-4(\alpha_n + \eta_n|\bar{b}|^2)\omega}{\left(2\omega - \omega_n - \Psi_n|\bar{b}|^2\right)^2 + 4(\alpha_n + \eta_n|\bar{b}|^2)^2\omega^2} \tag{7.23}$$

By taking the modulus of Eq. (7.20), we obtain:

$$|\bar{a}|^2 = \frac{|\bar{b}|}{|\psi_n|}\sqrt{\left(2\omega - \omega_n - \Psi_n|\bar{b}|^2\right)^2 + 4(\alpha_n + \eta_n|\bar{b}|^2)^2\omega^2} \tag{7.24}$$

Using Eq. (7.24) in Eqs. (7.22-7.23), we derive:

$$\Re\left[\frac{2\psi_n\bar{a}^*\bar{b}}{\bar{a}}\right] = \frac{2\left(2\omega-\omega_n-\Psi_n|\bar{b}|^2\right)|\psi_n||\bar{b}|}{\sqrt{\left(2\omega-\omega_n-\Psi_n|\bar{b}|^2\right)^2+4(\alpha_n+\eta_n|\bar{b}|^2)^2\omega^2}} \tag{7.25}$$

$$\Im\left[\frac{2\psi_n\bar{a}^*\bar{b}}{\bar{a}}\right] = \frac{-4(\alpha_n+\eta_n|\bar{b}|^2)\omega|\psi_n||\bar{b}|}{\sqrt{\left(2\omega-\omega_n-\Psi_n|\bar{b}|^2\right)^2+4(\alpha_n+\eta_n|\bar{b}|^2)^2\omega^2}} \tag{7.26}$$

Taking the modulus squared of Eq. (7.19):

$$\left\{\left(\omega-\omega_0-\Psi_0|\bar{a}|^2-\Re\left[\frac{2\psi_n\bar{a}^*\bar{b}}{\bar{a}}\right]\right)^2 + \left((\alpha_0+\eta_0|\bar{a}|^2)\omega-\Im\left[\frac{2\psi_n\bar{a}^*\bar{b}}{\bar{a}}\right]\right)^2\right\}|\bar{a}|^2=\zeta^2 \tag{7.27}$$

and using Equations (7.24)–(7.26) in Eq. (7.27) gives us an algebraic equation for the absolute value of the higher order mode amplitude $|\bar{b}|$:

$$\left\{\left(\omega-\omega_0-\Psi_0\frac{|\bar{b}|}{|\psi_n|}\sqrt{\left(2\omega-\omega_n-\Psi_n|\bar{b}|^2\right)^2+4(\alpha_n+\eta_n|\bar{b}|^2)^2\omega^2}- \frac{2\left(2\omega-\omega_n-\Psi_n|\bar{b}|^2\right)|\psi_n||\bar{b}|}{\sqrt{\left(2\omega-\omega_n-\Psi_n|\bar{b}|^2\right)^2+4(\alpha_n+\eta_n|\bar{b}|^2)^2\omega^2}}\right)^2 + \tag{7.28}$$

$$\left(\left(\alpha_0+\eta_0\frac{|\bar{b}|}{|\psi_n|}\sqrt{\left(2\omega-\omega_n-\Psi_n|\bar{b}|^2\right)^2+4(\alpha_n+\eta_n|\bar{b}|^2)^2\omega^2}\right)\omega - \frac{-4(\alpha_n+\eta_n|\bar{b}|^2)\omega|\psi_n||\bar{b}|}{\sqrt{\left(2\omega-\omega_n-\Psi_n|\bar{b}|^2\right)^2+4(\alpha_n+\eta_n|\bar{b}|^2)^2\omega^2}}\right)^2\right\}\times \tag{7.29}$$

$$\frac{|\bar{b}|}{|\psi_n|}\sqrt{\left(2\omega-\omega_n-\Psi_n|\bar{b}|^2\right)^2+4(\alpha_n+\eta_n|\bar{b}|^2)^2\omega^2}=\zeta^2$$

(7.30)

After numerically solving Eq. (7.30) for $|\bar{b}|$, and using it in Eq. (7.24), we can calculate the amplitude of the quasi-uniform mode $|\bar{a}|$.

For the calculation shown in Fig. 7.1, we used the following parameters: $\omega_0(H) = 2\pi \cdot (3.02 \cdot \frac{H}{1\,\mathrm{kOe}} + 2.05)\,\mathrm{GHz}$, $\omega_1(H) = 2\pi \cdot (2.75 \cdot \frac{H}{1\,\mathrm{kOe}} + 6.6)\,\mathrm{GHz}$, $\omega_2(H) = 2\pi \cdot (2.8 \cdot \frac{H}{1\,\mathrm{kOe}} + 8.44)\,\mathrm{GHz}$, $\Delta\omega_0^{\mathrm{intrinsic}}(H) = 2\pi \cdot (0.035 \cdot \frac{H}{1\,\mathrm{kOe}} + 0.037)\,\mathrm{GHz}$ if $H > 0.83815\,\mathrm{kG}$ and $2\pi \cdot (-0.17 \cdot \frac{H}{1\,\mathrm{kOe}} + 0.21)\,\mathrm{GHz}$ if $H < 0.83815\,\mathrm{kG}$, $\Delta\omega_1^{\mathrm{intrinsic}}(H) = 2\pi \cdot (0.045 \cdot \frac{H}{1\,\mathrm{kOe}} + 0.09)\,\mathrm{GHz}$, $\Delta\omega_2^{\mathrm{intrinsic}}(H) = 2\pi \cdot (0.035 \cdot \frac{H}{1\,\mathrm{kOe}} + 0.2441)\,\mathrm{GHz}$, $\psi_n \cdot \zeta = h^2 \cdot 0.026\,\mathrm{GHz}^2$ and all intrinsic nonlinear parameters (Ψ_0, Ψ_n, η_0, η_n) are zero.

For the calculation in Fig. 7.2, the parameters are: $\omega_0^{\mathrm{ON}} = 2\pi \cdot 2.63$ GHz, $\omega_n^{\mathrm{ON}} = 2\pi \cdot 5.26$ GHz, $\omega_0^{\mathrm{OFF}} = 2\pi \cdot 3.23$ GHz, $\omega_n^{\mathrm{OFF}} = 2\pi \cdot 5.63$ GHz, $\alpha_0^{\mathrm{ON}}(0) = 0.02662$, $\alpha_n^{\mathrm{ON}}(0) = 0.03042$, $\alpha_0^{\mathrm{OFF}}(0) = 0.02282$, $\alpha_n^{\mathrm{OFF}}(0) = 0.02746$, $I_{\mathrm{c0}}^{\mathrm{ON}} = 90\ \mu$A, $I_{\mathrm{cn}}^{\mathrm{ON}} = 110\ \mu$A, $I_{\mathrm{c0}}^{\mathrm{OFF}} = 87\ \mu$A, $I_{\mathrm{cn}}^{\mathrm{OFF}} = 210\ \mu$A, $\psi_n \cdot \zeta = h^2 \cdot 0.006\,\mathrm{GHz}^2$ and all intrinsic nonlinear parameters (Ψ_0, Ψ_n, η_0, η_n) are zero.

For the Fig. 7.3, the calculation parameters are: $\omega_0^{\mathrm{ON}} = 2\pi \cdot 2.9571$ GHz, $\omega_n^{\mathrm{ON}} = 2\pi \cdot 5.9142$ GHz, $\omega_0^{\mathrm{OFF}} = 2\pi \cdot 3.7029$ GHz, $\omega_n^{\mathrm{OFF}} = 2\pi \cdot 6.5958$ GHz, $\alpha_0^{\mathrm{ON}}(0) = 0.01961$, $\alpha_n^{\mathrm{ON}}(0) = 0.02536$, $\alpha_0^{\mathrm{OFF}}(0) = 0.01566$, $\alpha_n^{\mathrm{OFF}}(0) = 0.02731$, $I_{\mathrm{c0}}^{\mathrm{ON}} = 85\ \mu$A, $I_{\mathrm{cn}}^{\mathrm{ON}} = 110\ \mu$A, $I_{\mathrm{c0}}^{\mathrm{OFF}} = 85\ \mu$A, $I_{\mathrm{cn}}^{\mathrm{OFF}} = 138\ \mu$A, $\psi_n \cdot \zeta = h^2 \cdot 0.012\,\mathrm{GHz}^2$ and all intrinsic nonlinear parameters (Ψ_0, Ψ_n, η_0, η_n) are zero.

7.4.2 Linewidth evaluation

All measurements presented in this Article were carried out with magnetic field applied along the easy axis of the MTJ devices so that the magnetic moments of the free and pinned layers are collinear to each other. In this geometry, the ST-FMR signals are dominated by photo-resistance contribution and are proportional to the square of the transverse component of the dynamic magnetization magnetization [102], which allows us to directly compare calculated $|a|^2(\omega)$ resonance curves to measured ST-FMR resonance curves $\tilde{V}_{\mathrm{mix}}(f)$ and to $V_{\mathrm{mix}}(f)$ approximated by numerical integration $\int \tilde{V}_{\mathrm{mix}}(f)\mathrm{d}f$.

When $V_{\mathrm{mix}}(f)$ and $|a|^2(\omega)$ are single-peak curves, they are fit to a sum of symmetric and antisymmetric Lorentzian curves with identical central frequencies and linewidth parameters as described in Ref. [97], and the spectral linewidth is determined as half-width at the half-maximum of the symmetric Lorentzian curve.

In order to quantify the linewidth of the split-peak resonance profile, we introduce a fitting function that is a sum of two Lorentzian curves with different central frequencies separated by δf. The half width of the resonance profile Δf_0 is then defined as the average of the half widths of the two Lorentzians plus $\delta f/2$.

7.4.3 Micromagnetic simulations

Micromagnetic simulations were performed using OOMMF software [126, 127]. To account for all magnetic interactions in the MTJ, a three dimensional model was employed with three ferromagnetic layers: free, SAF top and SAF bottom. We use material parameters obtained from the measurements and/or their accepted literature values (see Ref. [97] for the MTJ structure and fabrication details). Magnetization dynamics is excited by a combined pulse of spin torque and Oersted field, resulting from a sinc-shaped spatially uniform current pulse.

The spatial profile of the Oersted field corresponds to that of a long wire with elliptical cross section. The direction of the spin torque vector acting on the free layer is determined by the magnetization orientation of the SAF top layer. The spectrum of spin wave eigenmodes is obtained via fast Fourier transform (FFT) of the time dependent components of the layers' magnetic moment. Spatial mapping of the resulting Fourier amplitude and phase at a given frequency provides the mode profiles. The observed excitations are confirmed to be spin wave modes localized to the free layer. SAF modes are found at much higher frequencies than the free layer modes, and their frequencies are found to be incommensurable to the free layer quasi-uniform mode frequency [128].

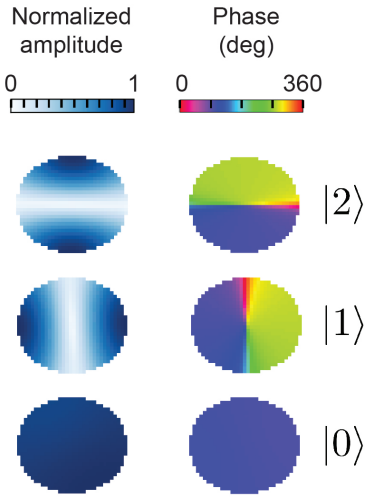

Figure 7.6: **Spatial profiles of spin wave eigenmodes.** Normalized amplitude and phase of the three lowest frequency spin wave eigenmodes of the MTJ free layer, given by micromagnetic simulations.

Bibliography

[78] H. Suhl. "The theory of ferromagnetic resonance at high signal powers". In: *J. Phys. Chem. Solids* 1.4 (1957), pp. 209–227. ISSN: 0022-3697. URL: http://www.sciencedirect.com/science/article/pii/0022369757900100.

[79] Hans G Bauer et al. "Nonlinear spin-wave excitations at low magnetic bias fields". In: *Nat. Commun.* 6 (2015), p. 8274. URL: http://rdcu.be/upc8.

[80] M. Bauer et al. "Observation of Spatiotemporal Self-Focusing of Spin Waves in Magnetic Films". In: *Phys. Rev. Lett.* 81 (17 1998), pp. 3769–3772. URL: https://link.aps.org/doi/10.1103/PhysRevLett.81.3769.

[81] Arnold Markovich Kosevich, BA Ivanov, and AS Kovalev. "Magnetic solitons". In: *Phys. Rep.* 194.3-4 (1990), pp. 117–238.

[82] A. N. Slavin and I. V. Rojdestvenski. "Bright and dark spin wave envelope solitons in magnetic films". In: *IEEE Trans. Magn.* 30.1 (1994), pp. 37–45. ISSN: 0018-9464.

[83] Mingzhong Wu, Boris A. Kalinikos, and Carl E. Patton. "Self-Generation of Chaotic Solitary Spin Wave Pulses in Magnetic Film Active Feedback Rings". In: *Phys. Rev. Lett.* 95.23 (Nov. 2005), p. 237202. URL: https://link.aps.org/doi/10.1103/PhysRevLett.95.237202.

[84] M. d'Aquino et al. "Analytical Treatment of Nonlinear Ferromagnetic Resonance in Nanomagnets". In: *IEEE Trans. Magn.* 53 (2017), p. 4301005. URL: doi.org/10.1109/TMAG.2017.2702641.

[85] S Il Kiselev et al. "Microwave oscillations of a nanomagnet driven by a spin-polarized current". In: *Nature* 425.6956 (2003), pp. 380–383. URL: http://dx.doi.org/10.1038/nature01967M3.

[86] I. N. Krivorotov et al. "Time-domain studies of very-large-angle magnetization dynamics excited by spin transfer torques". In: *Phys. Rev. B* 77.5 (Feb. 28, 2008), p. 054440. URL: https://link.aps.org/doi/10.1103/PhysRevB.77.054440.

[87] C. T. Boone et al. "Resonant Nonlinear Damping of Quantized Spin Waves in Ferromagnetic Nanowires: A Spin Torque Ferromagnetic Resonance Study". In: *Phys. Rev. Lett.* 103 (16 2009), p. 167601. URL: https://link.aps.org/doi/10.1103/PhysRevLett.103.167601.

[88] Luqiao Liu et al. "Spin-Torque Switching with the Giant Spin Hall Effect of Tantalum". In: *Science* 336.6081 (May 4, 2012), pp. 555–558. ISSN: 0036-8075, 1095-9203. URL: http://science.sciencemag.org/content/336/6081/555 (visited on 05/21/2016).

[89] William H. Rippard et al. "Spin-transfer dynamics in spin valves with out-of-plane magnetized CoNi free layers". In: *Phys. Rev. B* 81.1 (Jan. 29, 2010), p. 014426. URL: https://link.aps.org/doi/10.1103/PhysRevB.81.014426.

[90] D. Houssameddine et al. "Spin-torque oscillator using a perpendicular polarizer and a planar free layer". In: *Nat. Mater.* 6.6 (June 2007), pp. 447–453. ISSN: 1476-1122. URL: http://www.nature.com/nmat/journal/v6/n6/abs/nmat1905.html?foxtrotcallback=true (visited on 07/20/2017).

[91] A. Houshang et al. "Spin-wave-beam driven synchronization of nanocontact spin-torque oscillators". In: *Nat. Nanotech.* 11.3 (Mar. 2016), pp. 280–286. ISSN: 1748-3387. URL: https://www.nature.com/nnano/journal/v11/n3/full/nnano.2015.280.html (visited on 07/14/2017).

[92] Vladislav E. Demidov et al. "Magnetic nano-oscillator driven by pure spin current". In: *Nat. Mater.* 11.12 (Dec. 2012), pp. 1028–1031. ISSN: 1476-1122. URL: https://www.nature.com/nmat/journal/v11/n12/full/nmat3459.html (visited on 07/15/2017).

[93] Ferran Macià, Dirk Backes, and Andrew D. Kent. "Stable magnetic droplet solitons in spin-transfer nanocontacts". In: *Nature Nanotechnology* 9.12 (Dec. 2014), pp. 992–996. ISSN: 1748-3387. URL: https://www.nature.com/nnano/journal/v9/n12/full/nnano.2014.255.html (visited on 07/20/2017).

[94] Jian Zhu et al. "Voltage-Induced Ferromagnetic Resonance in Magnetic Tunnel Junctions". In: *Phys. Rev. Lett.* 108.19 (May 9, 2012), p. 197203. URL: http://link.aps.org/doi/10.1103/PhysRevLett.108.197203 (visited on 05/02/2015).

[95] S. Miwa et al. "Highly sensitive nanoscale spin-torque diode". In: *Nat. Mater.* 13.1 (Jan. 2014), pp. 50–56. ISSN: 1476-1122. URL: https://www.nature.com/nmat/journal/v13/n1/full/nmat3778.html (visited on 07/14/2017).

[96] Bin Fang et al. "Giant spin-torque diode sensitivity in the absence of bias magnetic field". In: *Nat. Commun.* 7 (Apr. 7, 2016), p. 11259. ISSN: 2041-1723. URL: https://www.nature.com/articles/ncomms11259 (visited on 07/15/2017).

[97] A. M. Gonçalves et al. "Spin torque ferromagnetic resonance with magnetic field modulation". In: *Appl. Phys. Lett.* 103.17 (2013), p. 172406. URL: http://dx.doi.org/10.1063/1.4826927.

[98] AA Tulapurkar et al. "Spin-torque diode effect in magnetic tunnel junctions". In: *Nature* 438.7066 (2005), pp. 339–342. URL: http://dx.doi.org/10.1038/nature04207M3.

[99] J. C. Sankey et al. "Spin-Transfer-Driven Ferromagnetic Resonance of Individual Nanomagnets". In: *Phys. Rev. Lett.* 96 (22 2006), p. 227601. URL: https://link.aps.org/doi/10.1103/PhysRevLett.96.227601.

[100] Motoya Shinozaki et al. "Damping constant in a free layer in nanoscale CoFeB/MgO magnetic tunnel junctions investigated by homodyne-detected ferromagnetic resonance". In: *Appl. Phys. Exp.* 10.1 (2017), p. 013001. URL: http://stacks.iop.org/1882-0786/10/i=1/a=013001.

[101] Christopher J. Safranski et al. "Material parameters of perpendicularly magnetized tunnel junctions from spin torque ferromagnetic resonance techniques". In: *Appl. Phys. Lett.* 109.13 (Sept. 26, 2016), p. 132408. ISSN: 0003-6951. URL: http://aip.scitation.org/doi/10.1063/1.4963354.

[102] Michael Harder, Yongsheng Gui, and Can-Ming Hu. "Electrical detection of magnetization dynamics via spin rectification effects". In: *Phys. Rep.* Electrical detection of magnetization dynamics via spin rectification effects 661 (Nov. 23, 2016), pp. 1–59. ISSN: 0370-1573. URL: http://www.sciencedirect.com/science/article/pii/S0370157316303167.

[103] O. Mosendz et al. "Quantifying Spin Hall Angles from Spin Pumping: Experiments and Theory". In: *Phys. Rev. Lett.* 104.4 (Jan. 28, 2010), p. 046601. URL: https://link.aps.org/doi/10.1103/PhysRevLett.104.046601.

[104] C. Liu et al. "Electrical detection of ferromagnetic resonance in ferromagnet/n-GaAs heterostructures by tunneling anisotropic magnetoresistance". In: *Appl. Phys. Lett.* 105.21 (Nov. 24, 2014), p. 212401. ISSN: 0003-6951. URL: http://aip.scitation.org/doi/abs/10.1063/1.4902088.

[105] César L. Ordóñez Romero et al. "Three-magnon splitting and confluence processes for spin-wave excitations in yttrium iron garnet films: Wave vector selective Brillouin light scattering measurements and analysis". In: *Phys. Rev. B* 79 (14 2009), p. 144428. URL: https://link.aps.org/doi/10.1103/PhysRevB.79.144428.

[106] H. Schultheiss et al. "Direct Current Control of Three Magnon Scattering Processes in Spin-Valve Nanocontacts". In: *Phys. Rev. Lett.* 103.15 (Oct. 8, 2009), p. 157202. URL: https://link.aps.org/doi/10.1103/PhysRevLett.103.157202.

[107] Hidekazu Kurebayashi et al. "Controlled enhancement of spin-current emission by three-magnon splitting". In: *Nat. Mater.* 10.9 (2011), pp. 660–664. URL: http://www.nature.com/nmat/journal/v10/n9/full/nmat3053.html.

[108] R. N. Costa Filho, M. G. Cottam, and G. A. Farias. "Microscopic theory of dipole-exchange spin waves in ferromagnetic films: Linear and nonlinear processes". In: *Phys. Rev. B* 62 (10 2000), pp. 6545–6560. URL: https://link.aps.org/doi/10.1103/PhysRevB.62.6545.

[109] Alina M Deac et al. "Bias-driven high-power microwave emission from MgO-based tunnel magnetoresistance devices". In: *Nat. Phys.* 4.10 (2008), pp. 803–809. URL: http://www.nature.com/nphys/journal/v4/n10/full/nphys1036.html.

[110] V. E. Demidov et al. "Control of Magnetic Fluctuations by Spin Current". In: *Phys. Rev. Lett.* 107.10 (Sept. 2, 2011), p. 107204. URL: https://link.aps.org/doi/10.1103/PhysRevLett.107.107204.

[111] G. D. Fuchs et al. “Spin-torque ferromagnetic resonance measurements of damping in nanomagnets”. In: *Appl. Phys. Lett.* 91.6 (Aug. 6, 2007), p. 062507. ISSN: 0003-6951. URL: http://aip.scitation.org/doi/10.1063/1.2768000.

[112] GA Melkov et al. “Nonlinear Ferromagnetic Resonance in Nanostructures Having Discrete Spectrum of Spin-Wave Modes”. In: *IEEE Magn. Lett.* 4 (2013), p. 4000504. URL: http://ieeexplore.ieee.org/stamp/stamp.jsp?arnumber=6595654.

[113] M. Helsen et al. “Non-linear radial spinwave modes in thin magnetic disks”. In: *Appl. Phys. Lett.* 106.3 (Jan. 19, 2015), p. 032405. ISSN: 0003-6951. URL: http://aip.scitation.org/doi/full/10.1063/1.4906196.

[114] Jan Podbielski, Detlef Heitmann, and Dirk Grundler. “Microwave-Assisted Switching of Microscopic Rings: Correlation Between Nonlinear Spin Dynamics and Critical Microwave Fields”. In: *Phys. Rev. Lett.* 99.20 (Nov. 14, 2007), p. 207202. URL: https://link.aps.org/doi/10.1103/PhysRevLett.99.207202.

[115] V. V. Naletov et al. “Ferromagnetic resonance spectroscopy of parametric magnons excited by a four-wave process”. In: *Phys. Rev. B* 75 (14 2007), p. 140405. URL: https://link.aps.org/doi/10.1103/PhysRevB.75.140405.

[116] Y. Khivintsev et al. “Nonlinear ferromagnetic resonance in permalloy films: A non-monotonic power-dependent frequency shift”. In: *Phys. Rev. B* 81.5 (Feb. 23, 2010), p. 054436. URL: https://link.aps.org/doi/10.1103/PhysRevB.81.054436.

[117] Bivas Rana et al. “Effect of excitation power on voltage induced local magnetization dynamics in an ultrathin CoFeB film”. In: *Sci. Rep.* 7 (May 24, 2017), p. 2318. ISSN: 2045-2322. URL: http://www.ncbi.nlm.nih.gov/pmc/articles/PMC5443791/.

[118] Feng Guo, Lyubov M. Belova, and Robert D. McMichael. “Nonlinear ferromagnetic resonance shift in submicron Permalloy ellipses”. In: *Phys. Rev. B* 91 (6 2015), p. 064426. URL: https://link.aps.org/doi/10.1103/PhysRevB.91.064426.

[119] Hans T. Nembach et al. “Mode- and Size-Dependent Landau-Lifshitz Damping in Magnetic Nanostructures: Evidence for Nonlocal Damping”. In: *Phys. Rev. Lett.* 110.11 (Mar. 12, 2013), p. 117201. URL: https://link.aps.org/doi/10.1103/PhysRevLett.110.117201.

[120] Y. Li and W.E. Bailey. “Wave-Number-Dependent Gilbert Damping in Metallic Ferromagnets”. In: *Phys. Rev. Lett.* 116.11 (Mar. 18, 2016), p. 117602. URL: https://link.aps.org/doi/10.1103/PhysRevLett.116.117602.

[121] Koji Sekiguchi et al. “Time-Domain Measurement of Current-Induced Spin Wave Dynamics”. In: *Phys. Rev. Lett.* 108.1 (Jan. 5, 2012), p. 017203. URL: https://link.aps.org/doi/10.1103/PhysRevLett.108.017203.

[122] Andrei Slavin and Vasil Tiberkevich. “Nonlinear auto-oscillator theory of microwave generation by spin-polarized current”. In: *IEEE Trans. Magn.* 45.4 (2009), pp. 1875–1918. URL: http://ieeexplore.ieee.org/stamp/stamp.jsp?arnumber=4802339.

[123] V. Lauer et al. "Spin-transfer torque based damping control of parametrically excited spin waves in a magnetic insulator". In: *Appl. Phys. Lett.* 108.1 (Jan. 4, 2016), p. 012402. ISSN: 0003-6951. URL: http://aip.scitation.org/doi/abs/10.1063/1.4939268.

[124] Chi Zhang et al. "Engineering the Spectrum of Dipole Field-Localized Spin-Wave Modes to Enable Spin-Torque Antidamping". In: *Phys. Rev. Appl.* 7.5 (May 25, 2017), p. 054019. URL: https://link.aps.org/doi/10.1103/PhysRevApplied.7.054019.

[125] S. M. Rezende, F. M. de Aguiar, and A. Azevedo. "Magnon excitation by spin-polarized direct currents in magnetic nanostructures". In: *Phys. Rev. B* 73.9 (Mar. 6, 2006), p. 094402. URL: https://link.aps.org/doi/10.1103/PhysRevB.73.094402.

[126] M. J. Donahue and D. G. Porter. *OOMMF User's Guide*. National Institute of Standards and Technology, Gaithersburg, MD, 1999.

[127] Robert D McMichael and Mark D Stiles. "Magnetic normal modes of nanoelements". In: *J. Appl. Phys.* 97.10 (2005), 10J901.

[128] P. S. Keatley et al. "Resonant enhancement of damping within the free layer of a microscale magnetic tunnel valve". In: *J. Appl. Phys.* 117.17 (May 7, 2015), 17B301. ISSN: 0021-8979, 1089-7550. URL: http://aip.scitation.org/doi/10.1063/1.4907701.

Chapter 8

Conclusion

Competition between superconducting and ferromagnetic ordering in S/F heterostructures can lead to unusual types of magneto-transport effects emerging from the proximity effect at the S/F interfaces. This thesis provided evidence of this unusual magneto-transport effect by reporting measurements of the superconducting transition temperature T_c in CoO/Co/Cu/Co/Nb multilayers in a spin valve structure. T_c was measured both as a function of the in-plane angle between the Co magnetic moments and of the thicknesses of the Co/Cu/Co spin valve layers. It was found that T_c is a nonmonotonic function of the angle, with a minimum near orthogonal orientations of the magnetic moments of the two Co layers. The behavior of T_c as a function of these variables was quantitatively described by an efficient microscopic method that is based on a linearization of the self-consistent Bogoliubov–de Gennes equations. We have shown that the nonmonotonic behavior of $T_c(\alpha)$ is correlated with the formation of long-range triplet pairs.

In the crystallographic study of $IrMn_3$ thin films, it was found that the films grown on MgO/Ir buffer layers exhibit a high degree of $L1_2$ chemical ordering but lack any crystallographic texture; conceivably, MgO deposition at higher temperatures may improve the film growth.

The films grown on Ir buffer layer are highly textured with strong out-of-plane and in-plane crystallographic order. For these highly textured films, the vertical grain size is 15 nm and the out-of-plane mosaic spread is 2.8°, which is comparable to $IrMn_3$ films grown by MBE. The films exhibit crystallographic twinning with two sets of grains, which are in-plane rotated by 60° to each other. The $L1_2$ chemical order parameter for these highly textured $IrMn_3$ films is determined to be 0.45. These highly textured films of $IrMn_3$ exhibit the crystallographic and chemical ordering required for observation of anomalous Hall effect in this non-collinear antiferromagnet. In addition to this X-ray diffractometry characterization, some devices were fabricated to measure their anomalous Hall resistance. For some samples, it was possible to see some signal of this effect, but the samples did not survive more than a few hours. The main reason was that the multilayer peeled off very easily. Further progress in the project would be to find a better adhesion layer. It would be also interesting to find a substrate with lower lattice mismatch with the $IrMn_3$ film.

Finally, the nonlinear resonant three-magnon scattering measurements demonstrate that magnetic damping of spin wave modes in a nanoscale ferromagnet has a strong nonlinear component of resonant character that appears at a discrete set of magnetic fields corresponding to resonant three-magnon scattering. This strong resonant nonlinearity can give rise to unusual spin wave resonance profile with a local minimum at the resonance frequency in sharp contrast to the properties of the linear and nonlinear spin wave resonances in bulk ferromagnets. The resonant nonlinearity has a profound effect on the response of the nanomagnet to spin torque. Antidamping spin torque that reduces the quasi-uniform spin wave mode damping at magnetic fields far from the resonant three-magnon regime can strongly enhance the damping in the resonant regime. This inversion of the effect of spin torque on magnetization dynamics by the resonant nonlinearity is expected to have significant impact on the performance of nanoscale spin torque devices such as magnetic memory and spin torque oscillators.